POLITECNICO DI TORINO

Master's Degree in Aerospace Engineering

Master's Degree Thesis

Experimental Study on Silicon Carbide Passivation in High-Enthalpy Oxygen Flows

Supervisors

Prof. Dario Pastrone

Prof. Georg Herdrich

Candidate

Jacopo TARANTINO

DECEMBER 2024

Experimental Study on Silicon Carbide Passivation in High-Enthalpy Oxygen Flows

Experimentelle Studie über die Passivierung von Siliziumkarbid in hochenergetischen Sauerstoffströmen

Master Thesis

Jacopo Tarantino

IRS-24-S-087

Examiners:
Apl. Prof. Dr.-Ing. Georg Herdrich
Prof. Dr. Dario Giuseppe Pastrone

Supervisors:
Jonathan Skalden, M. Sc.
Konstantinos Papavramidis, M. Sc.
Hendrik Burghaus, M. Sc.

External Supervisors:
Denise Keil, M. Sc.
Nicolas Steenbergen, M. Sc.

Institute of Space Systems
University of Stuttgart

December 2024

University of Stuttgart
Institute of Space Systems

Pfaffenwaldring 29 · 70569 Stuttgart · www.irs.uni-stuttgart.de

Task Description Master's Thesis

for Jacopo Tarantino

Investigation of SiO2 Surface Generation Methods for a VLEO Intake

Untersuchung von Methoden zur Herstellung einer SiO2 Oberfläche für einen VLEO-Einlass

Motivation:

Atmosphere-breathing electric propulsion (ABEP) offers a promising approach for long-duration missions in very low earth orbits (VLEO) by utilizing the residual atmosphere as a propellant for electric thrusters. This innovative technology not only enables drag compensation but also has the potential to enhance the efficiency and sustainability of space missions. An ABEP system consists of two core elements: thruster and intake. The thruster has already been successfully tested, and now an intake is under construction process at IRS, which enables a complete system test. The intake concept has already been identified as a specular coated paraboloid, with the principle proven via numerical simulations. The intake's material plays a pivotal role in the overall efficiency of the system as gas-surface interactions affect capturing and delivering the atmospheric particles to the electric thruster. The design and optimisation of the intake device is in line with the material reflection properties to ensure an adequate performance of the ABEP system. Here, silica (SiO_2) is a promising candidate material due to high chemical and thermal stability, as well as specular reflection properties.
In this study, two methods to generate a SiO_2 surface shall be investigated, passivation of SiC in an oxygen plasma and plasma-enhanced chemical vapor deposition (PECVD). In collaboration with the German Aerospace Centre's (DLR) Institute for Technical Physics, samples of both processes shall be optically investigated prior and after treatment. Further tasks include the procurement of the substrates for both SiO_2 surface processes and a test campaign in the plasma wind tunnels of IRS. Documentation in a report concludes the thesis.

Task Description:

- Literature study of SiO_2 surface processes and optical instruments
- Procurement of substrates
- Optical analysis of substrates and generated SiO_2 surfaces
- Organisation and conduction of SiC passivation in plasma wind tunnels at IRS and PECVD
- Documentation

Research is performed at:	IRS / DLR Institute for Technical Physics
Internal advisor:	Jonathan Skalden, Konstantinos Papavramidis, Hendrik Burghaus
External advisor:	Denise Keil, Thomas Klumpp, Prof. Dr. Dario Pastore
Start date:	02.04.2024
Submission deadline:	07.10.2024

Acknowledgement of receipt:
I hereby confirm that I read and understood the task of the master's thesis, the legal framework as well as the study and exam regulations.

gez. G. Herdrich	gez. D. Pastrone	gez. Jacopo Tarantino
apl. Prof. Dr.-Ing. Georg Herdrich (Responsible Professor)	External advisor	Student

Declaration

I, **Jacopo Tarantino** hereby certify that I have written this **Master's Thesis** independently with the support of the supervisor, and I did not use any resources apart from those specified. The thesis, or substantial components of it, has not been submitted as part of graded course work at this or any other educational institution.

I also declare that during the preparation of this thesis I have followed the appropriate regulations regarding copyright for the use of external content, according to the rules of good scientific and academic practice[1]. I have included unambiguous references for any external content (such as images, drawings, text passages etc.), and in cases for which approval is required for the use of this material, I have obtained the approval of the owner for the use of this content in my thesis. I am aware that I am responsible in the case of conscious negligence of these responsibilities.

STUTTGART, 15/11/2025, gez. Jacopo Tarantino

.....

Location, Date, Signature

I hereby agree that my **Master's Thesis** titled

Investigation of SiO2 Surface Generation Methods for a VLEO Intake

is archived and publicly available in the library of the Institute of Space Systems of the University of Stuttgart and that the thesis is available on the website of the institute as well as in the online catalogue of the library of the University of Stuttgart. The latter means that bibliographic data of the thesis (title, author, year of publication, etc.) is permanently and worldwide available.

After finishing the work, I will, for this purpose, deliver a further copy of the thesis along with the examination copy, as well as a digital version.

I transfer the proprietary of these additional copies to the University of Stuttgart. I concede that the thesis and the results generated within the scope of this work can be used free of cost and of temporal and geographical restrictions for the purpose of research and teaching to the institute of Space Systems. If there exist utilization right agreements related to the thesis from the institute or third parties, then these agreements also apply for the results developed in the scope of this thesis.

STUTTGART, 15/11/2025, gez. Jacopo Tarantino

.....

Location, Date, Signature

[1] Stated in the DFG recommendations for “Assurance of Good Scientific Practice” or in the statute of the University of Stuttgart for “Ensuring the Integrity of Scientific Practice and the Handling of Misconduct in Science“

Abstract

Satellite missions in Very Low Earth Orbit (VLEO), at altitudes below 450 km, face challenges such as rapid orbital decay due to atmospheric drag and material degradation caused by erosion from Atomic Oxygen (AO). To address these challenges, Atmosphere-Breathing Electric Propulsion (ABEP) technology offers a promising solution by utilizing atmospheric particles as propellant to significantly extend mission durations without the need for onboard fuel. This thesis explores the behavior of possible advanced coatings for the intake of ABEP systems, with particular attention to the passivation of sintered Silicon Carbide (SiC) in high-enthalpy oxygen flows.

SiC is selected for its high chemical and thermal stability, the material's potential to form a protective layer of silicon dioxide (SiO_2) enhances its properties, mitigating erosion caused by AO. This study analyzes the behavior of SiC in oxygen plasma by exposing it to the inductively driven Plasma Wind Tunnel (PWK3) at the Institute of Space Systems (IRS) of the University of Stuttgart. By varying the exposure time as a parameter, the passivation of SiC is evaluated by measuring its performance under high-enthalpy oxygen exposure.

Furthermore, SiO_2 coatings were developed on potential intake samples using the Plasma-Enhanced Chemical Vapor Deposition (PECVD) technique, in order to verify the preservation of specular reflection properties necessary for efficient particle collection. SiO_2 demonstrated specular properties at surface roughness levels in the Angström range, an essential characteristic for optimizing particle intake efficiency in ABEP systems.

Surface analysis, conducted at the German Aerospace Center (DLR) in Stuttgart, employed advanced techniques such as Nomarski Microscopy, White Light Interferometry (WLIM), Atomic Force Microscopy (AFM), Scanning Electron Microscopy (SEM), and Energy-Dispersive X-ray Spectroscopy (EDX).

The findings contribute to the advancement of sustainable propulsion technologies for satellites by informing the selection and optimization of materials for ABEP intake systems, thereby enhancing both performance and longevity in the challenging VLEO environment.

Contents

List of Figures

List of Tables

Nomenclature

Symbols

A	[m^2]	Area
α	[1/K]	Coefficient of Thermal Expansion
E	[GPa]	Young's Modulus
E_0	[eV]	Electron Beam Energy
$I(z)$	[W/m^2]	Intensity at a Point
k	[N/m]	Spring Constant
L	[m]	Length
m	[kg]	Mass
$\dot{m}$	[kg/s]	Mass Flow Rate
n	[-]	Refractive Index
R_a	[μm]	Arithmetic Mean Roughness
R_q	[μm]	Root Mean Square Roughness
R_z	[μm]	Ten-Point Mean Roughness
R_1	[K]	Thermal Shock Resistance Parameter Based on Critical Temperature Difference
$\gamma(z)$	[-]	Fringe Visibility
λ	[nm]	Wavelength
$\delta\phi$	[rad]	Phase Difference
$\sigma_{b4,m}$	[MPa]	Mean Flexural Strength Measured Using 4-Point Bending
T	[K]	Temperature
$Z(x)$	[m]	Height Deviation at Position x Along a Line
$Z(x,y)$	[m]	Height Deviation at Position x, y Over an Area

Abbreviations

ABEP	Atmosphere-Breathing Electric Propulsion
AFM	Atomic Force Microscopy
AO	Atomic Oxygen
BSE	Backscattered Electron Detector
CTE	Coefficient of Thermal Expansion
DIC	Differential Interference Contrast
EDX	Energy-Dispersive X-ray Spectroscopy
EHT	Electron High Tension
FEA	Finite Element Analysis
GSI	Gas Surface Interactions
HOPG	Highly Oriented Pyrolytic Graphite
IKV	Institute for Plastics Processing
IMTCCC	Institute for Manufacturing Technologies of Ceramic Components and Composites
IPT	RF Helicon-Based Plasma Thruster
MISSE	Materials International Space Station Experiment
NIR	Near-Infrared
NRLMSISE	Naval Research Laboratory Mass Spectrometer and Incoherent Scatter Extension
PECVD	Plasma-Enhanced Chemical Vapor Deposition
PID	Proportional-Integral-Derivative
PID	Proportional-Integral-Derivative Controller
PWT3	Plasma Wind Tunnel 3
PSI	Phase Shifting Interferometry
RMS	Root Mean Square
RWTH	Rheinisch-Westfälische Technische Hochschule Aachen
SE	Secondary Electrons
SEI	Secondary Electron Imaging
SDDs	Silicon Drift Detectors
SEM	Scanning Electron Microscopy
SOAR	Satellite for Orbital Aerodynamics Research
VSI	Variable Step Interferometry
WLIM	White Light Interferometry Microscopy
WD	Working Distance

Chemical Substances

Al	Aluminum
Au	Gold
B	Boron
BN	Boron Nitride
C	Carbon
Cu	Copper
$C_6H_{12}O_6$	Hexamethyldisiloxane (HMDSO)
Fe	Iron
HCl	Hydrochloric Acid
HMDSO	Hexamethyldisiloxane
HOPG	Highly Oriented Pyrolytic Graphite
Ni	Nickel
O	Atomic Oxygen
O_2	Molecular Oxygen
SSiC	Sintered Silicon Carbide
SiC	Silicon Carbide
SiO_2	Silicon Dioxide
Ti	Titanium

1. Introduction

The rapid expansion of satellite deployments in Low Earth Orbit (LEO) has increased the concerns on orbital congestion, collision risks, and the proliferation of space debris [1]. To mitigate these issues and enhance the performance of satellite missions, attention is shifting toward Very Low Earth Orbit (VLEO) missions, which operate at altitudes below 450 km [2]. VLEO offers significant advantages, including enhanced payload performance for Earth observation and communication systems due to the reduced distance to Earth's surface, enabling higher-resolution imaging and more efficient telecommunications with lower latency and reduced power requirements [1].

However, operating satellites in VLEO presents substantial challenges. The denser atmospheric environment at these altitudes results in increased aerodynamic drag, which can lead to rapid orbital decay if not actively compensated [3]. Additionally, the presence of atomic oxygen (AO), a highly reactive species, poses a threat to spacecraft materials through erosion, compromising structural integrity and reducing mission lifespans [4]. These challenges necessitate innovative solutions to enable sustained operations in VLEO while maintaining spacecraft durability [5].

Atmosphere-Breathing Electric Propulsion (ABEP) systems offer a promising solution by utilizing residual atmospheric particles as propellants for electric thrusters. This approach compensates for aerodynamic drag without the need of onboard propellant storage, effectively extending mission durations and enhancing sustainability by reducing mass and system complexity [6]. An ABEP system comprises two critical components: the intake, which collects atmospheric particles, and the thruster, which ionizes and accelerates these particles to generate thrust [7].

Material selection for the intake is crucial due to the harsh VLEO environment characterized by high-enthalpy oxygen flows and exposure to AO [8]. The intake materials must exhibit high thermal and chemical stability, resist erosion, and maintain surface properties that optimize particle capture and delivery. Silicon Carbide (SiC) has emerged as a promising intake coating material owing to its remarkable chemical and thermal stability, high hardness, and resistance to oxidation and erosion at elevated temperatures. When oxidized, Silicon Dioxide (SiO_2) forms a protective layer that can enhance its reflective properties, potentially improving particle capture efficiency for a specific type of intake, i.e. based on specular reflection.[9].

The formation of a high-quality SiO_2 surface layer on SiC samples serves multiple critical functions for VLEO applications. Primarily, the SiO_2 layer acts as a protective barrier against the highly reactive atomic oxygen prevalent in VLEO, which is known to cause significant erosion and degradation of spacecraft materials [10]. The formation of this layer on SiC provides a self-protection mechanism by hindering oxygen flux to the underlying material surface [11].

Moreover, the SiO_2 surface layer exhibits medium to low catalytic activity with respect to oxygen and nitrogen at typical transition temperatures [10]. This characteristic is beneficial in reducing undesirable chemical reactions on the spacecraft surface. Additionally, when properly oxidized, the SiO_2 layer can maintain the initial surface roughness of the original silicon surface, preserving the material's smoothness and integrity [10]. The formation of a thin layer of alpha-quartz orientation retains the surface smoothness, which is advantageous for maintaining the desired aerodynamic properties [10].

However, for VLEO applications, SiO_2 surfaces present some limitations. They produce broader angular distributions of scattered particles compared to other materials such as Highly Oriented Pyrolytic Graphite (HOPG), despite having lower surface roughness [10]. The interaction potential for SiO_2 surfaces is highly corrugated because electrons are tightly bound in covalent bonds, making the scattering dynamics less favorable for gas concentration applications [10]. Consequently, the concentration factor achievable with SiO_2 surfaces is an order of magnitude lower than what can be achieved using materials like HOPG [10]. These characteristics make SiO_2 surfaces on SiC a compromise solution—providing good protection against atomic oxygen erosion but not necessarily optimal for aerodynamic quality in VLEO applications where specular reflection properties are desired [1].

Previous studies [12, 13] have tested SiC samples under high-enthalpy plasma environments to evaluate their oxidation behavior and erosion resistance. These samples provide valuable baseline data for understanding

the material's quality over time and under different environmental exposures. Analyzing these samples alongside new SiC samples with reduced roughness allows for a comprehensive assessment of the protective SiO_2 layer formation.

In addition to SiC samples, Gold-Nickel samples realized with the Repli-formed Optics™ technology [14] are potential candidates for intake surfaces. Coating these materials with the SiO_2 layer could enhance their quality under VLEO conditions by improving erosion resistance and maintaining the specular reflection necessary for efficient particle collection.

Furthermore, developing coatings on Gold-Nickel intake samples using advanced techniques like Plasma-Enhanced Chemical Vapor Deposition (PECVD) [15] opens new ways for material optimization. Applying a SiO_2 coating onto Gold-Nickel substrates aims to combine the advantageous properties of both materials, potentially leading to superior quality in the harsh VLEO environment.

1.1. Previous Studies and Related Projects

Significant research efforts have been undertaken to overcome the challenges associated with sustained operations in VLEO. The DISCOVERER project [1], funded under the European Union's Horizon 2020 program [16], aimed to revolutionize satellite operations in VLEO by developing technologies that enable long-term missions at these lower altitudes. The project focused on advancing ABEP systems, aerodynamic materials and coatings, and aerodynamic characterization to mitigate increased drag and material erosion in VLEO. Building upon these foundations, the Technology Enhancement of Cathode-Less Electric Propulsion (RAM-CLEP) project [17], funded by the European Space Agency (ESA), seeks to further develop and demonstrate ABEP technologies for practical application in VLEO missions. These projects emphasize the importance of material selection for the intake component, highlighting the need for materials capable of withstanding high-enthalpy oxygen flows and resisting AO erosion.

The University of Manchester has conducted experiments such as the Satellite for Orbital Aerodynamics Research (SOAR) [18] and participated in the Materials International Space Station Experiment-12 (MISSE-12) mission [5]. The MISSE-12 mission, part of NASA's Materials International Space Station Experiment (MISSE) program [19], focuses on testing materials and technologies that can withstand VLEO conditions, including exposure to AO.

Research at the IRS has also contributed to the development of ABEP technologies. Recent studies on intake designs for satellite propulsion in VLEO highlight the superior quality of specular intakes over diffuse ones. Simulations showed that specular intakes achieved up to 94% collection efficiency between 150 km and 250 km, compared to 46% for diffuse intakes. Specular intakes also performed better in misaligned flows [20]. Further studies revealed that shorter intakes and larger discharge channel diameters improve efficiency, especially when combined with specular surfaces [21]. Building on this, a parabolic intake prototype was designed, optimizing geometry in combination with different specularity levels to maximize collection efficiency for ABEP systems. The intake's aluminum build and specular coating were designed to enhance particle reflection and efficient collection in VLEO [22].

In prior research, SiC samples were exposed to high-enthalpy oxygen plasmas in the the Plasma Wind Tunnel 3 (PWK3) at the Institute of Space Systems Stuttgart (IRS Stuttgart) to simulate VLEO conditions. In the course of this work new polished SiC samples underwent surface analysis to evaluate oxidation behavior, erosion rates, and the formation of protective SiO_2 layers. The findings provided insights into the material's quality [13].

Additionally, the exploration of coating techniques such as PECVD [15] for depositing SiO_2 layers on potential Gold-Nickel intake materials with very low level of roughness has been investigated. Coating these samples aims to enhance their durability and maintain the necessary specular reflection properties for efficient ABEP intake operation under VLEO conditions.

These studies have laid the groundwork for further exploration into material selection, coating processes, and system optimization for ABEP technology.

1.2. Objectives of the Thesis

The primary objective of this thesis is to evaluate the suitability of an intake coating material for ABEP systems operating in VLEO. This work specifically aims to investigate the behavior of SiC under high-enthalpy oxygen plasma conditions, focusing on its ability to form a protective SiO_2 layer and its potential for improving gas-surface interactions critical to ABEP intake efficiency.

To achieve this goal, the research is structured around the following specific objectives:

- **Literature study**: Conduct a comprehensive review of existing research on ABEP systems, emphasizing the optimization of specular intake geometries. Investigate the properties of SiC, particularly its potential to form a passivating SiO_2 layer in high-enthalpy O_2 flows, critical for VLEO applications. Explore the PWK3 facility at IRS, assessing its relevance for simulating VLEO conditions, and evaluate the PECVD technique for advanced intake coatings. Finally, analyze state-of-the-art surface characterization methods, focusing on their application to material performance in aerospace contexts.
- **Procurement of materials**: Establish communication with industry partners and suppliers to procure high-quality SiC and intake samples. Ensure the availability of all necessary materials required for experimental analysis.
- **Experimental parameter study**: Investigate the passivation of SiC in a pure O_2 plasma environment using the PWK3 at the IRS. Simulate high-enthalpy conditions by varying exposure time as a key parameter. Evaluate the formation of the SiO_2 layer and analyze SiC samples from previous studies to compare oxidation behavior under different exposure durations and conditions.
- **Surface analysis**: Perform surface analysis of SiC samples before and after plasma exposure. Analyze SiO_2-coated Gold-Nickel intake samples before and after PECVD coating processes. Employ advanced microscopy techniques, including Nomarski microscopy, WLIM, AFM, and SEM coupled with EDX.
- **Passivation mechanism investigation**: Analyze the formation and stability of the protective SiO_2 layer. Study its impact on the erosion-resistant properties of SiC. Evaluate the significance of these properties for the quality and performance of ABEP intakes.
- **Assessment of suitability**: Integrate findings from the literature review, experimental results, and surface analyses. Assess the overall suitability of SiC as an intake material for ABEP systems. Provide recommendations for material selection and enhancements to improve the efficiency, durability, and sustainability of ABEP systems in VLEO.

This thesis is structured to provide a detailed investigation of materials suitable for ABEP systems, with a particular focus on SiC and Gold-Nickel intake samples. Chapter 2 establishes the theoretical background necessary to understand the context and objectives of the study. Chapter 3 details the experimental methodology, including the preparation and polishing of SiC samples, the coating process applied to Gold-Nickel samples using the PECVD technique, the plasma exposure process and the surface analysis techniques. Chapter 4 presents the experimental results of polished SiC samples tested in the PWK3 facility and the results obtained from Gold-Nickel intake samples coated using the PECVD technique. Chapter 5 concludes the thesis by summarizing key insights, discussing their implications for ABEP intake design, and proposing directions for future research.

By addressing these objectives, this thesis aims to contribute to the development of advanced ABEP systems, specifically through the evaluation and optimization of SiO_2 as an intake coating material, supporting the goal of sustainable and efficient satellite operations in VLEO.

2. Theoretical Background

This chapter provides the foundational knowledge necessary to understand the challenges and solutions associated with satellite operations in VLEO and the application of ABEP systems. The composition and dynamics of the VLEO environment are discussed, highlighting their impact on material degradation and orbital decay. The principles of ABEP systems, focusing on the specular intake design, are explored in detail. Additionally, the properties of SiC and SiO_2 coatings are analyzed, emphasizing their thermal stability, oxidation behavior, and erosion resistance in high-enthalpy oxygen flows. The process of coating using PECVD and the passivation behavior of materials exposed to high-enthalpy oxygen plasma in PWK3 are also reviewed, providing critical insights into the formation and effectiveness of a SiO_2 protective layer. Surface analysis methodologies employed in this thesis are examined, establishing the scientific basis for subsequent experimental investigations.

2.1. Very Low Earth Orbit

VLEO refers to orbital altitudes below 450 kilometers [2]. The atmospheric environment in VLEO is characterized by higher atmospheric density compared to higher orbits, which significantly influences satellite design and operational strategies.

2.1.1. Atmospheric Composition Models

Among the various atmospheric models available, the NRLMSISE-00 model [23] is employed in this study due to its accurate representation of lower thermosphere conditions and its proven application in ABEP system research. Figure 2.1 illustrates the averaged particle number densities and neutral temperature T_{in} in VLEO for an equatorial orbit. In this scenario, the latitude is fixed at 0°, while longitudes are averaged between 0° and 360° in 45° increments.

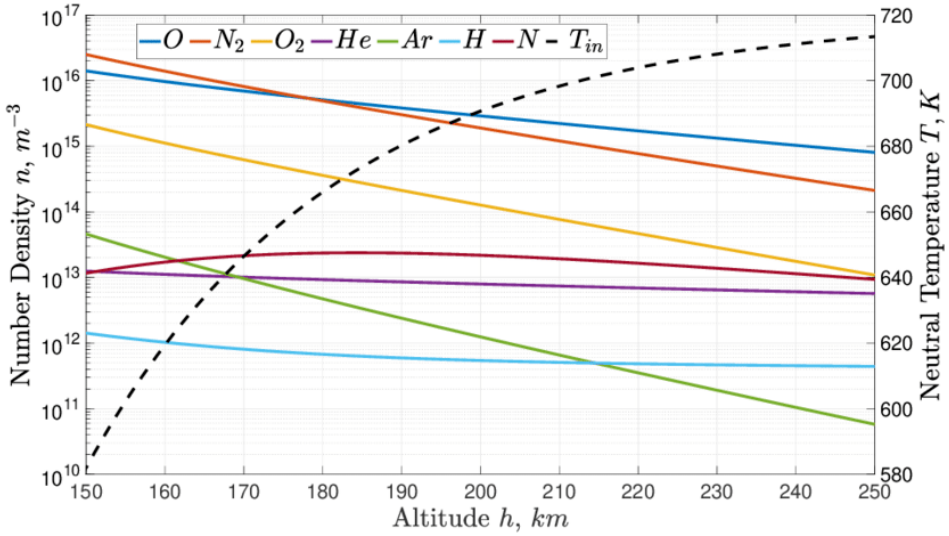

Figure 2.1.: Atmospheric composition in VLEO based on the NRLMSISE-00 atmospheric model [8].

The data presented in Figure 2.1 was extracted from the NASA Community Coordinated Modeling Center [24] for the date 15/02/2020 at 00:00:00. This corresponds to a solar radio flux of $F_{10.7} = 69.5$ and a geomagnetic index of $A_p = 4.1$, indicative of low solar activity. The altitude range selected for this study spans from $h = 150$ km to $h = 250$ km. Within this altitude range, the dominant atmospheric species are nitrogen (N_2) and AO. These species are sufficiently abundant to be harvested for propulsion purposes in ABEP systems [25].

2.1.2. Advantages and Challenges in VLEO

Operating satellites in VLEO offers several compelling advantages that can significantly enhance the performance and sustainability of space missions. However, these benefits are accompanied by substantial challenges that necessitate advanced technological solutions [1].

2.1.2.1. Advantages of VLEO Operations

- **Extended mission duration:** ABEP systems facilitate prolonged satellite operations in VLEO by continuously compensating for atmospheric drag. This negates the need for extensive onboard propellant reserves, thereby enabling sustained missions without frequent propulsion system refueling [8].
- **Reduced launch mass and cost:** Eliminating the requirement for large propellant tanks significantly reduces the overall mass of the spacecraft. This mass reduction allows for either the inclusion of larger payloads, enhancing mission capabilities, or the utilization of smaller, more cost-effective launch vehicles, thereby lowering overall mission costs [7].
- **Improved sensor sensitivity and data quality:** Proximity to Earth enhances the sensitivity of onboard sensors and instruments, enabling more precise measurements and higher-quality data collection. This is particularly advantageous for scientific research and Earth monitoring applications [4].
- **Potential for novel mission profiles:** VLEO opens ways for innovative mission designs, including high-frequency Earth imaging, rapid revisit times for reconnaissance, and enhanced capabilities for atmospheric and space weather studies [4].

2.1.2.2. Challenges of VLEO Operations

Despite the numerous advantages, operating in VLEO introduces several significant challenges that must be addressed to ensure mission success and longevity.

- **Increased atmospheric drag:** The denser atmospheric environment at VLEO results in markedly higher aerodynamic drag compared to higher orbits. Without effective drag compensation, satellites experience rapid orbital decay, which can drastically shorten mission lifespans and necessitate frequent reboost maneuvers [4].
- **AO erosion:** VLEO is characterized by high concentrations of AO, a highly reactive species that can aggressively erode spacecraft materials. AO-induced erosion compromises structural integrity, degrades surface coatings, and diminishes the quality of critical components, thereby threatening the operational functionality and durability of satellites [8].

Maximizing the benefits of VLEO operations while mitigating its inherent challenges requires a multifaceted approach that integrates advanced propulsion technologies, durable materials, and sophisticated spacecraft design.

2.2. ABEP Systems

The ABEP system comprises two main components: an intake to collect atmospheric particles and an electric thruster to convert the collected particles into propulsion.

2.2.1. Concept and Principles

ABEP systems use atmospheric particles as propellant, collected by an intake system and utilized in an electric thruster [8].

As shown in Figure 2.2, the system features a front-mounted intake to capture atmospheric particles, which are then compressed or sent directly to the thruster. The electric thruster, equipped with a birdcage antenna and solenoids or magnets, ionizes and accelerates these particles to produce thrust, counteracting drag. Powered by solar arrays and an RF power supply, the ABEP system operates without the need for onboard propellant [8].

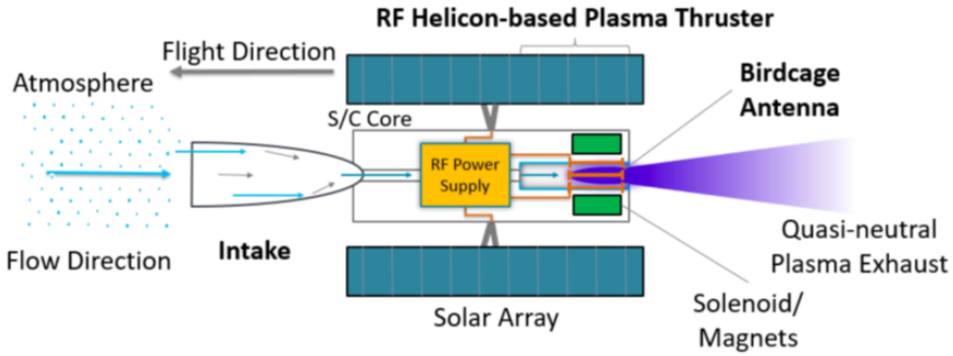

Figure 2.2.: ABEP concept using the IPT [22, 8]

2.2.2. Thruster Design

Traditional electric propulsion (EP) systems, such as Hall-effect thrusters (HETs) and ion engines [26], face significant challenges when operating with atmospheric propellants in VLEO environments. These challenges include electrode erosion due to exposure to reactive species like AO and lower performance when using atmospheric gases. To overcome these limitations, the Radio Frequency (RF) helicon-based plasma thruster (IPT) has been developed as a key component of ABEP systems [27].

2.2.2.1. The RF Helicon-based Plasma Thruster (IPT)

The IPT operates on the principle of electrodeless plasma generation and acceleration using RF power and helicon waves. The thruster design avoids the use of electrodes, thereby significantly reducing erosion and extending operational life when using atmospheric propellants [6]. A schematic diagram of the IPT setup concept is shown in Figure 2.3.

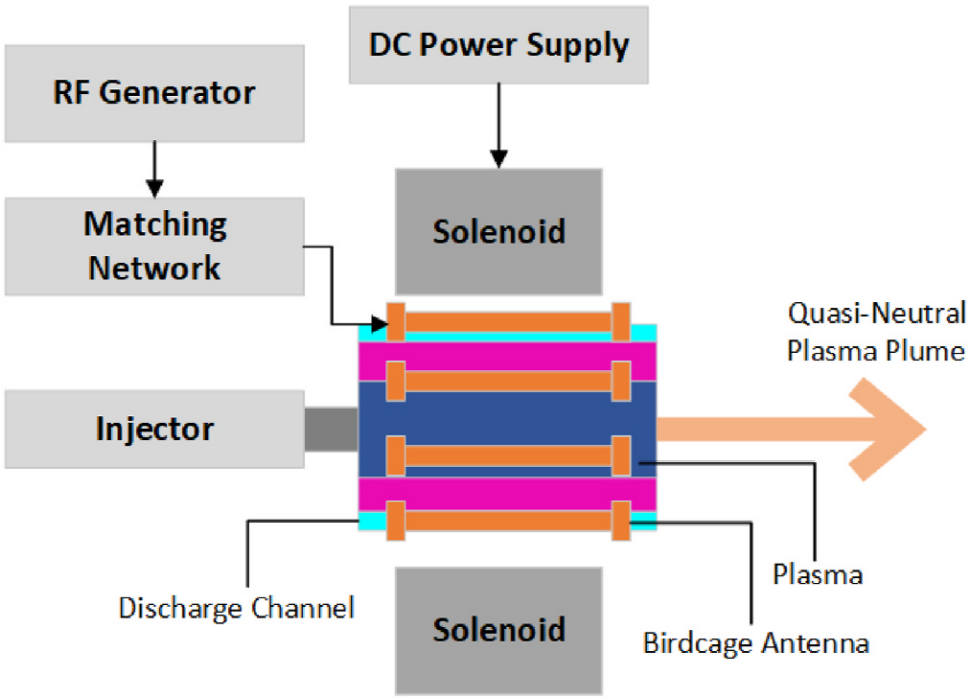

Figure 2.3.: Setup concept of the IPT lab-prototype [17].

The key components of the IPT include [28]:

- **Discharge channel**: A cylindrical dielectric tube where plasma generation occurs.
- **RF antenna (Birdcage antenna)**: Surrounds the discharge channel and generates oscillating electromagnetic fields to ionize the propellant gas.

- **External magnetic field system**: Provides a static magnetic field "via a solenoid or permanent magnets" necessary for helicon wave formation.
- **Propellant injection system**: Introduces atmospheric gases collected by the intake or injector into the discharge channel.
- **RF generator and matching network**: Supplies RF power to the antenna and optimizes power transfer.
- **Thruster support structure**: Mechanical structure supporting the thruster components.

The working principle of the IPT involves several key processes. Atmospheric gases are collected by an intake system and injected into the discharge channel, where an RF antenna powered by an RF generator, operating at $40.68\,\mathrm{MHz}$ [28], creates oscillating electromagnetic fields. An external static magnetic field is applied to establish the necessary conditions for helicon wave propagation. The interplay between the RF fields and the static magnetic field ionizes the propellant gas, generating a high-density plasma. Helicon waves, which are low-frequency waves excited within the plasma, further enhance ionization efficiency. The resulting plasma is then accelerated and ejected from the thruster, producing thrust. This process eliminates the need for electrodes or a neutralizer, as the exhaust remains quasi-neutral.

The IPT offers numerous advantages, making it a choice for advanced propulsion systems. Its electrodeless design eliminates any erosion issues by AO, significantly enhancing the thruster's operational lifespan [28]. The system is able to utilize efficient ionization of atmospheric gases, particularly nitrogen and oxygen, taking advantage of the available resources in VLEO environments [6].

2.2.3. Intake Design

The intake design is a critical component of ABEP systems, significantly influencing overall performance and efficiency. The primary function of an ABEP intake is to collect and compress atmospheric particles from the rarefied VLEO environment, delivering them to the thruster at suitable pressures and mass flow rates. Effective intake design must address several key parameters, including collection efficiency, compression ratio, backflow prevention, structural integrity, and compliance with mass and volume constraints [8].

In the rarefied gas conditions of VLEO, the atmospheric density is extremely low, and the mean free path of particles is comparable to or larger than the characteristic dimensions of the intake system. Key parameters influencing intake design include:

- **Collection efficiency:** The collection efficiency (η_c) is defined as the ratio of the collected particle flux ($\dot{N}_{\mathrm{out}}$) to the incoming particle flux ($\dot{N}_{\mathrm{in}}$) [8]:

$$\eta_c = \frac{\dot{N}_{\mathrm{out}}}{\dot{N}_{\mathrm{in}}}. \tag{2.1}$$

  This metric evaluates the intake's ability to capture and direct atmospheric particles to the thruster effectively. High collection efficiency is essential for maximizing the propellant mass flow rate supplied to the thruster, thereby enhancing the overall performance and sustainability of the propulsion system.
- **Compression ratio:** The compression ratio (CR) quantifies the increase in particle density from the free stream (n_{free}) to the thruster inlet (n_{inlet}) and is expressed as:

$$CR = \frac{n_{\mathrm{inlet}}}{n_{\mathrm{free}}}. \tag{2.2}$$

  A higher compression ratio ensures a denser propellant supply at the thruster inlet, which can lead to improved thrust generation.
- **Backflow prevention:** Backflow prevention minimizes the escape of collected particles back into space, ensuring that the maximum number of collected particles are utilized for propulsion. This is critical for maintaining high system efficiency and preventing loss of performance.
- **Structural integrity:** The intake must maintain structural integrity in the harsh VLEO environment, which includes exposure to atomic oxygen (AO), micrometeoroid impacts, and thermal stresses from high-enthalpy oxygen flows. Materials and designs must resist erosion, corrosion, and mechanical stresses to ensure long-term reliability and operability.

2.2.3.1. Design Approaches

Two primary approaches are employed in the design of ABEP intakes: diffuse reflection intakes and specular reflection intakes. Each approach leverages different physical mechanisms to enhance particle collection and compression.

An illustrative comparison between diffuse and specular reflection mechanisms is shown in Figure 2.4, highlighting the fundamental differences in particle trajectories upon interaction with the intake surfaces.

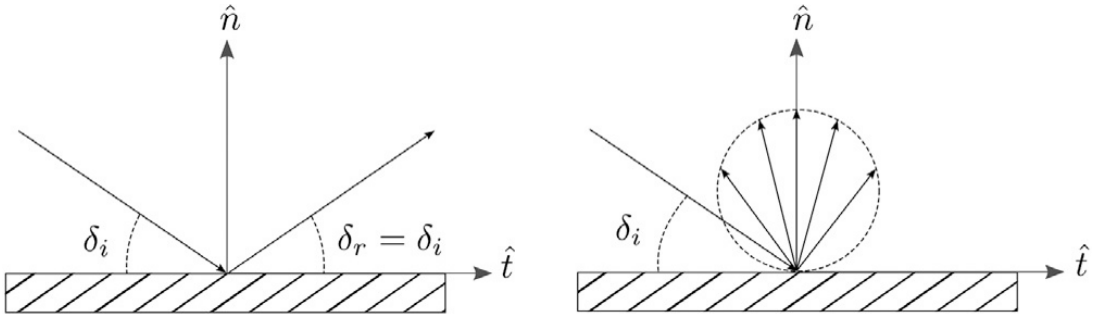

Figure 2.4.: Comparison of specular (left) and diffuse (right) reflection mechanisms in ABEP intake designs.

Diffuse Reflection Intakes

Diffuse reflection intakes utilize surfaces that cause incoming atmospheric particles to scatter upon impact in random directions. These designs often employ structures with multiple stages or channels, such as honeycomb configurations, to increase the probability that scattered particles are directed towards the thruster inlet [8].

Key features of diffuse reflection intakes include:

- **Simplicity**: Relatively straightforward geometries and manufacturing processes.
- **Moderate collection efficiency**: Typically achieving collection efficiencies in the range of 30% to 50% [8], depending on the specific design and operating conditions.
- **Backflow reduction**: Multi-stage designs can help minimize particle backflow by increasing the likelihood that particles are redirected towards the thruster.

An example schematic of a diffuse reflection intake is shown in Figure 2.5.

Specular Reflection Intakes

Specular reflection intakes employ surfaces with mirror-like properties to reflect incoming particles in a controlled, predictable manner. These designs often utilize parabolic or conical geometries to focus or channel particles towards the thruster inlet [6]. The smooth, reflective surfaces aim to preserve the kinetic energy of the particles and enhance compression.

In contrast to diffuse reflection, specular reflection maintains the angle of incidence equal to the angle of reflection, as depicted in Figure 2.4. This predictable behavior allows for precise directing of particles towards the thruster, improving collection efficiency and compression ratios.

In this master thesis, the focus is placed on specular intake designs due to their superior performance compared to diffuse designs. Specular intakes not only achieve higher collection efficiencies and compression ratios but also alleviate some of the stringent requirements on the propulsion system by delivering a more concentrated and directed particle flow. This emphasis aligns closely with the ongoing research at IRS, which has demonstrated the advantages of specular reflection for ABEP systems in VLEO.

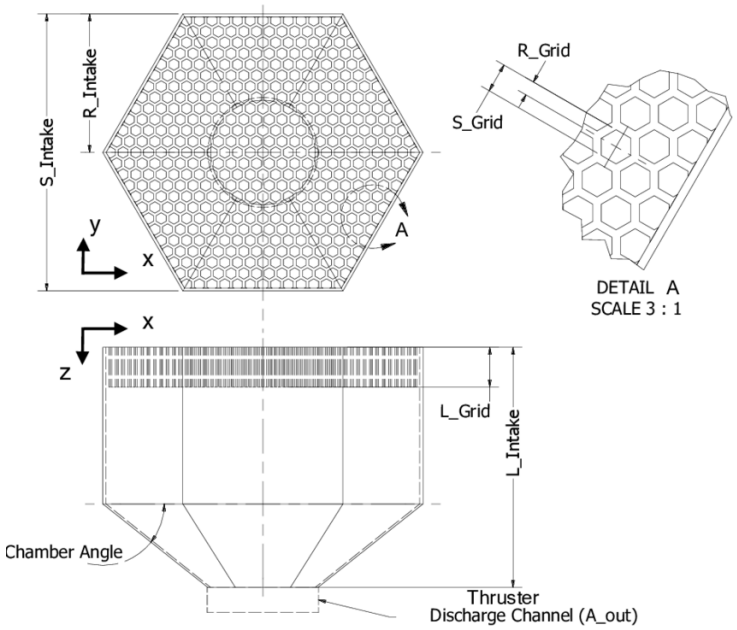

Figure 2.5.: Schematic of a diffuse reflection intake design [8].

2.3. Specular Intake Design

The specular intake design is a critical component of ABEP systems, aimed at maximizing the collection efficiency of atmospheric particles in VLEO. By utilizing specular reflection principles, the intake directs incoming atmospheric particles towards the thruster with minimal energy loss, enhancing the overall performance of the ABEP system [8].

2.3.1. Principle of Operation

Specular intake designs rely on mirror-like surfaces that reflect incoming atmospheric particles in a deterministic manner, preserving their kinetic energy and directing them towards the thruster inlet. This represents a significant departure from traditional diffuse-based designs. The fundamental concept is based on specular reflection properties to guide incoming particles through controlled reflections toward a focal point [8].

2.3.1.1. Parabolic Geometry and Focal Point

The intake geometry is based on a paraboloid shape, which has the property of reflecting parallel incoming particles towards a common focal point. The general equation of a parabola in Cartesian coordinates is:

$$y = \frac{x^2}{4f} \tag{2.3}$$

where f is the focal length, defined as the distance between the vertex of the parabola and its focal point. In the context of the intake design, the focal point location can be adjusted to optimize particle collection and compression ratios. Three main configurations, as shown in Figure 2.6, are considered based on the focal point location relative to the thruster:

- **Focal point inside the discharge channel (S-FT)**: The focal point is located within the thruster's discharge channel.
- **Focal point at the intake-thruster interface (S-FE)**: The focal point lies at the plane separating the intake and the thruster.
- **Focal point ahead of the discharge channel (S-FI)**: The focal point is positioned upstream of the intake outlet.

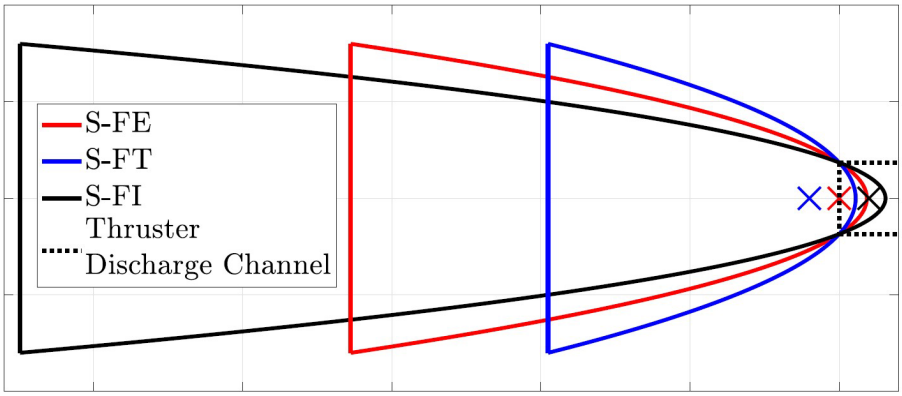

Figure 2.6.: Focal point variations in specular intake design [8].

Studies have indicated that placing the focal point inside the discharge channel (S-FT configuration) generally yields the highest collection efficiency, as it allows for better focusing of particles into the thruster [8].

2.3.1.2. Intake Geometry Equations

The key equations governing the specular intake design relate the geometric parameters of the intake to the desired focal point location and the dimensions of the thruster's discharge channel [22]. The relationship between the focal length f, the intake diameter d_{in}, the intake length l_{in}, and the thruster discharge channel diameter d_{IPT} can be expressed as follows:

$$\frac{1}{4f}\left(\frac{d_{\text{IPT}}}{2}\right)^2 = s_f + f \tag{2.4}$$

Equation for the Thruster Interface
Equation (2.4) defines the relationship at the thruster interface, where the discharge channel diameter d_{IPT} is the smallest diameter of the intake.

Equation for the Intake inlet
Equation (2.5) defines the relationship at the inlet of the intake, where the intake diameter d_{in} is the largest diameter of the intake.

$$\frac{1}{4f}\left(\frac{d_{\text{in}}}{2}\right)^2 = l_{\text{in}} + s_f + f \tag{2.5}$$

where s_f is the distance between the end plane of the intake paraboloid and the focal point. These equations allow the calculation of the intake geometry based on the desired focal point location and the physical dimensions of the intake and thruster.

Derivation of Intake Length
Subtracting Equation (2.4) from Equation (2.5) eliminates $s_f + f$ and allows for the determination of the intake length l_{in}:

$$l_{\text{in}} = \frac{\left(\frac{d_{\text{in}}}{2}\right)^2 - \left(\frac{d_{\text{IPT}}}{2}\right)^2}{4f} \tag{2.6}$$

These equations facilitate the precise design of the intake geometry by linking the intake dimensions and focal point location to the thruster's discharge channel characteristics. A schematic illustration of the specular intake geometry is shown in Figure 2.7.

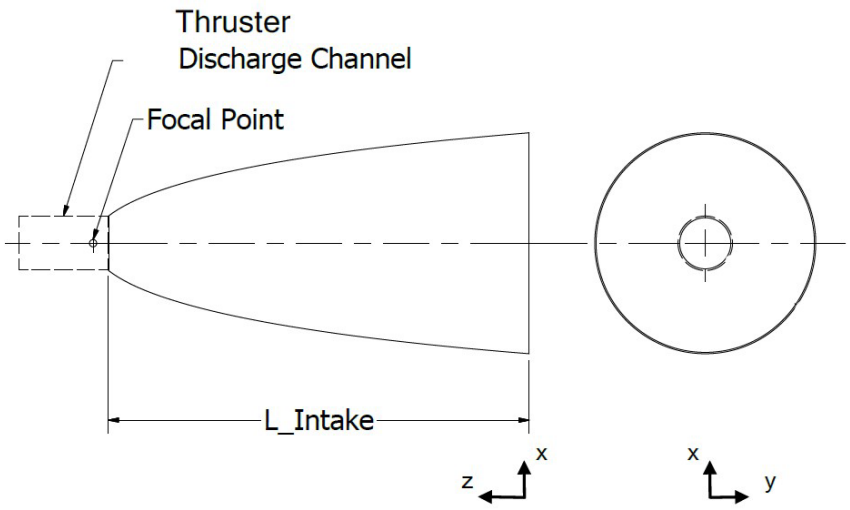

Figure 2.7.: Specular intake geometry [8].

2.3.2. Technical Considerations

The performance and efficiency of specular intake systems in ABEP platforms are governed by several critical technical parameters that must be carefully considered during the design phase.

2.3.2.1. Geometric Optimization

The optimization of intake geometry is a critical factor in achieving the desired performance of ABEP systems. Several geometric parameters must be carefully balanced to ensure efficient particle collection, minimize energy losses, and align with mission-specific requirements.

Focal Point Positioning

The precise placement of the parabola's focal point within the thruster discharge channel is crucial. This configuration ensures that reflected atmospheric particles are directed efficiently into the thruster, maximizing the propellant mass flow rate. Additionally, proper focal point positioning enhances the system's robustness against flow misalignment, providing a significant advantage over diffuse intake designs by reducing performance degradation in off-axis flows [8, 6].

Intake Length

The length of the intake plays a vital role in determining the compression ratio and overall collection efficiency. While longer intakes may theoretically improve compression by providing additional time and surface area for particle concentration, they also increase the probability of particle-wall interactions and backscattering. These interactions can significantly reduce collection efficiency, particularly for specular intakes operating in VLEO, where the high thermal velocities of atmospheric particles further exacerbate performance losses with increasing intake length [21]. As a result, the intake length must be carefully optimized to balance these trade-offs, ensuring sufficient compression without sacrificing efficiency or compromising compatibility with the thruster design [6].

Intake Diameter

The intake's frontal diameter directly affects the cross-sectional area available for atmospheric particle collection. Larger diameters enhance particle capture rates, particularly in lower altitudes where atmospheric density is higher. However, increasing the diameter also imposes constraints on the overall geometry, including aerodynamic drag and compatibility with the spacecraft's structural and design limitations. Consequently, the intake diameter must be optimized to maximize particle collection while maintaining compatibility with the thruster requirements and ensuring seamless integration within the spacecraft architecture [8].

By carefully tailoring these geometric parameters, the intake design can achieve a high level of performance, ensuring efficient particle capture, enhanced compression ratios, and reliable operation under VLEO conditions.

2.3.2.2. Performance Limitations

The performance analysis of specular intakes highlights several critical limitations and operational constraints that must be addressed for their effective implementation in ABEP systems:

- **Flow alignment sensitivity:** Specular intakes exhibit reduced performance with misaligned flow, although they remain more robust than diffuse designs [8].
- **Pressure distribution limitations:** At altitudes of 150 km, specular intakes achieve a pressure of approximately 0.3 Pa at the back of the intake [8]. While this falls below the typical operating pressure range of 1 to 7 Pa required by most laboratory model thrusters, experimental evidence suggests that helicon plasma thrusters can operate at pressures as low as 0.266 Pa. This indicates that the pressure limitation may be manageable for specific thruster designs [8].
- **Material degradation effects:** The intake's performance strongly depends on the material's ability to maintain specular reflection properties. AO exposure in the VLEO environment poses a significant risk of degradation over the mission lifetime, which could reduce the overall intake efficiency [8].
- **Environmental variability:** Operational variations in atmospheric density and composition, driven by temporal, seasonal, and solar activity fluctuations, significantly impact intake performance. These fluctuations alter the mass flow rate and collection efficiency, necessitating design margins to ensure effective operation under varying conditions [6].
- **Scaling limitations:** As spacecraft frontal area (A_f) increases, the required exhaust velocity (c_e) for drag compensation rises significantly. For example, a frontal area of 0.1 m^2 necessitates an exhaust velocity of approximately 48 km/s. While this is more feasible than the 190 to 210 km/s required by diffuse intakes, it still presents challenges for current electric propulsion technologies [8].

This theoretical foundation of specular intake design naturally leads to the critical consideration of gas-surface interactions, which fundamentally determine the actual performance of these geometrically optimized surfaces. The relationship between ideal geometric design and real material properties becomes particularly important when considering AO exposure and surface degradation in the VLEO environment.

2.3.3. Gas-Surface Interaction Mechanisms

Gas-surface interactions (GSI) are pivotal in determining the efficiency and longevity of specular intake designs in ABEP systems. In the VLEO environment, AO and other reactive species interact with the intake surface, leading to potential erosion, oxidation, and changes in surface reflectivity. Understanding these interactions is essential for optimizing intake performance and selecting appropriate materials and coatings.

2.3.3.1. Maxwell's Gas-Surface Interaction Model

James Clerk Maxwell proposed a model to describe the interaction between gas molecules and surfaces, introducing the concept of specular and diffuse reflections [29]. According to Maxwell's model, a fraction f of the incident particles is diffusely reflected, while the remaining fraction $(1 - f)$ is reflected specularly.

The scattering kernel, representing the probability distribution of reflected particle velocities, is given by:

$$\Phi(\vec{c}_r, \vec{c}_i) = (1 - f)\delta(\vec{c}_r - \vec{c}_{\text{spec}}) + f\Phi_{\text{diffuse}}(\vec{c}_r) \tag{2.7}$$

where $\vec{c}_i$ is the incident particle velocity, $\vec{c}_r$ is the reflected particle velocity, $\vec{c}_{\text{spec}}$ is the specularly reflected velocity, δ is the Dirac delta function, and Φ_{diffuse} represents the diffuse reflection distribution.

2.3.3.2. Accommodation Coefficient

The energy accommodation coefficient, denoted as β, is a key parameter that quantifies the degree of energy exchange between incident particles and a surface. It is defined mathematically by the equation:

$$\beta = \frac{E_i - E_r}{E_i - E_w}, \tag{2.8}$$

where E_i represents the incident energy flux of the particles, E_r is the energy flux of the reflected particles, and E_w corresponds to the energy flux of particles re-emitted in thermal equilibrium with the surface, commonly referred to as diffuse reflection at the wall temperature. The value of β ranges from 0, which indicates no energy exchange and perfectly elastic specular reflection, to 1, signifying complete energy accommodation and fully diffuse reflection. This coefficient is critical in characterizing surface interaction dynamics, particularly in environments like VLEO, where the interplay of energy transfer mechanisms influences material performance and system efficiency.

2.3.3.3. Types of Scattering

Gas-surface interactions produce a range of scattering behaviors, primarily influenced by the accommodation coefficient β and the physical characteristics of the surface. These behaviors, depicted in Figure 2.8, are critical for understanding the dynamics of particle reflection in atmospheric-breathing electric propulsion systems.

Diffuse scattering ($\beta \approx 1$) occurs when particles fully equilibrate with the surface temperature before re-emission. The result is a Maxwellian velocity distribution that is isotropic relative to the surface normal. This type of scattering, characterized by a cosine distribution of reflected particles, typically arises on rough or highly adsorptive surfaces.

Subspecular scattering describes a situation where particles reflect at angles closer to the surface normal than the specular angle. This behavior is caused by interactions that reduce the tangential momentum of the particle, leading to reflection angles smaller than the angle of incidence.

In contrast, superspecular scattering involves particles reflecting at angles greater than the specular angle, moving further from the surface normal. This phenomenon is often attributed to repulsive surface forces that amplify the tangential component of the particle's velocity upon reflection.

Blended diffuse and quasi-specular scattering represents a hybrid behavior where particles exhibit both diffuse and quasi-specular reflection characteristics. In this scenario, some particles reflect diffusely, while others maintain partial energy accommodation and reflect quasi-specularly ($0 < \beta < 1$).

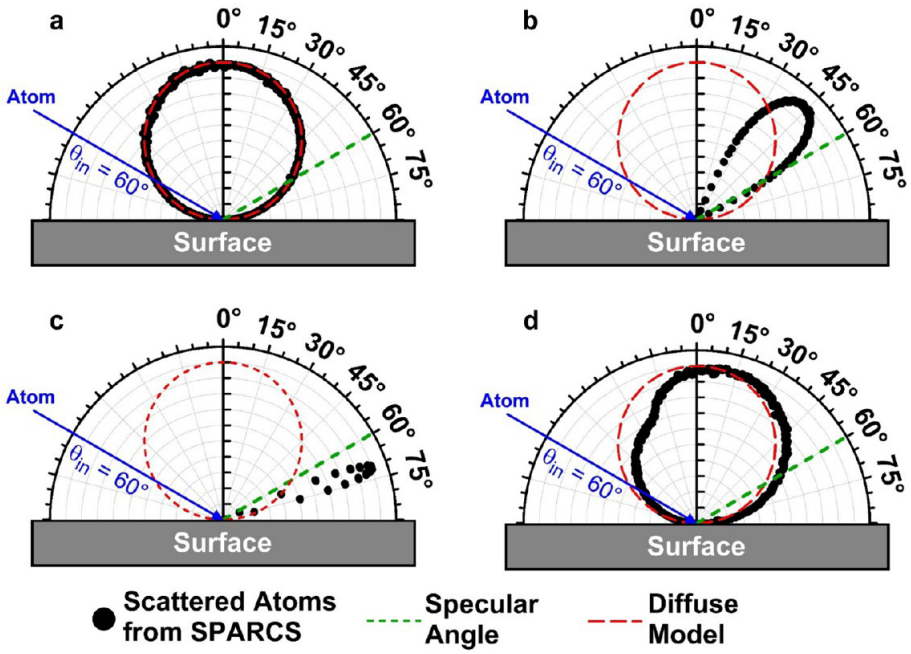

Figure 2.8.: Scattering models represented in SPARCS: (a) diffuse scattering, (b) subspecular scattering, (c) superspecular scattering, and (d) blended diffuse and quasi-specular scattering [10].

Understanding these scattering mechanisms is fundamental for accurately predicting the behavior of specular intakes. Reflection efficiency and particle trajectories, both of which significantly impact intake performance, depend directly on these interaction models [30, 10].

In the harsh environment of Very Low Earth Orbit (VLEO), maintaining specular reflection properties poses a considerable challenge due to factors such as atomic oxygen (AO) erosion and contamination. Material selection is crucial to address these issues. Silicon Carbide (SiC) emerges as a promising candidate for intake coatings, offering high hardness, superior thermal stability, and strong resistance to AO erosion, making it well-suited for ensuring long-term durability and performance.

2.4. Silicon Carbide

SiC could emerge as a promising material for intake coating applications in VLEO conditions due to its exceptional chemical, thermal, and mechanical properties. This section explores the characteristics of SiC that could make it suitable for such applications and examines its behavior under the extreme conditions encountered in VLEO environments.

2.4.1. Chemical, Thermal, and Mechanical Properties of SiC

Silicon carbide (SiC) is a compound formed by silicon and carbon atoms, characterized by its chemical formula SiC. SiC exists in multiple polytypes, with the most prevalent being α-SiC, which has a hexagonal crystal structure, and β-SiC, which exhibits a cubic crystal structure. The strong covalent bonding between silicon and carbon atoms imparts exceptional properties to SiC, making it a preferred material for demanding aerospace applications [11, 9].

Chemical Properties

SiC exhibits remarkable chemical stability, maintaining inertness to most acids and alkalis, which renders it highly resistant to chemical corrosion. One of its notable attributes is its oxidation behavior under specific conditions. When exposed to elevated temperatures in an oxygen-rich environment, SiC reacts to form a protective silicon dioxide (SiO_2) layer on its surface. This SiO_2 layer serves as a barrier, inhibiting further oxidation and enhancing the material's durability in thermally harsh environments [9].

It is crucial, however, to distinguish between this protective oxidation process and the behavior of SiC when exposed to high-enthalpy oxygen plasma, such as in the Plasma Wind Tunnel 3 (PWK3). In the

latter scenario, the extreme conditions lead to a rapid oxidation process that forms a SiO_2 layer. This plasma-induced oxidation is distinct from the conventional high-temperature oxidation in ambient oxygen atmospheres. While SiC shows high resistance to chemical degradation in ambient conditions, plasma environments challenge the material's surface stability, emphasizing the need for understanding these differing contexts [9].

Thermal Properties

SiC is renowned for its superior thermal properties, which are particularly beneficial for aerospace applications. Its high thermal conductivity, ranging from 120 to 270 W/(m·K), facilitates efficient heat dissipation, making it well-suited for environments with high thermal loads [31]. Additionally, SiC has a low thermal expansion coefficient of approximately 4.0×10^{-6} K^{-1} at typical operating temperatures (e.g., 1500–2000 K), minimizing thermal stresses caused by rapid temperature fluctuations [32]. This stability under thermal cycling enhances its structural integrity in high-temperature systems. Furthermore, the sublimation temperature of SiC, approximately 2700 °C, ensures its functionality in extreme thermal environments where other materials might fail [33].

Mechanical Properties

SiC's exceptional mechanical properties make it a standout material for structural applications. Its hardness, ranging from 24 to 28 GPa, approaches that of diamond, enabling high wear resistance, which is crucial in abrasive environments. Additionally, SiC's elastic modulus, between 450 and 470 GPa, indicates substantial stiffness, allowing it to maintain its shape and resist deformation under mechanical loads. Its notable fracture toughness further enhances its durability, providing resistance to crack propagation under stress [34].

When compared to other materials such as hexagonal boron nitride (h-BN) and diamond-like carbon (DLC), SiC demonstrates a superior combination of properties. For example, while h-BN offers high thermal stability, its mechanical strength and oxidation resistance are inferior to those of SiC. Similarly, DLC excels in hardness and low friction but lacks the thermal stability and oxidation resistance of SiC at elevated temperatures. Table 2.1 provides a comparative summary of SiC's key properties relative to these alternative aerospace materials [34, 35, 36].

Table 2.1.: Key properties of SiC compared to other aerospace materials

Property	**SiC**	**h-BN**	**Diamond-Like Carbon**
Density (kg/m^3)	3210	2100	2300
Melting Point (°C)	Sublimes at ∼2700	Decomposes at ∼2973	∼3700 (sublimes)
Thermal Conductivity (W/(m·K))	120–270	25–200	0.1–10
Thermal Expansion Coefficient (10^{-6} K^{-1})	4.0	1.0	0.5
Elastic Modulus (GPa)	450–470	14–34	100–150
Hardness (GPa)	24–28	1–2	10–50

2.4.2. Oxidation Behavior of SiC

The oxidation of SiC can be categorized into two regimes: passive oxidation and active oxidation [37, 11].

Passive Oxidation

Passive oxidation occurs at temperatures between approximately 800°C and 1200°C in oxygen-rich environments (oxygen partial pressures greater than 10^{-4} atm). In this regime, SiC reacts with oxygen to form a continuous and protective SiO_2 layer [38]:

$$\mathrm{SiC_{(s)}} + \frac{3}{2}\,\mathrm{O_2(g)} \rightleftharpoons SiO_2(\mathrm{s}) + \mathrm{CO(g)} \quad \Delta_r H^\circ = -944.47\,\mathrm{kJ/mol} \tag{2.9}$$

In the VLEO environment, temperatures are significantly low, typically ranging from −100°C to +100°C due to solar heating and Earth's albedo. For ABEP systems, understanding passive oxidation is essential to ensure the integrity of the protective SiO_2 layer under operational conditions.

Active Oxidation

Active oxidation occurs at higher temperatures above approximately 1200°C and at lower oxygen partial pressures (less than 10^{-4} atm). In this regime, the protective SiO_2 layer becomes volatile, and material loss occurs due to the formation of gaseous silicon monoxide (SiO):

$$SiC(s) + O_2(g) \rightarrow SiO(g) + CO(g) \tag{2.10}$$

Understanding these oxidation regimes is crucial for ABEP systems, as the protective SiO_2 layer formed during passive oxidation is essential for maintaining material integrity and preserving the specular reflection properties critical for intake performance (see Section 2.3.3).

2.4.2.1. Wagner and Turkdogan Oxidation Models

The Wagner and Turkdogan models provide foundational theoretical frameworks to describe the oxidation kinetics and mechanisms of SiC under oxidizing conditions [38].

Wagner's Model

Wagner's model [39] focuses on the diffusion-controlled oxidation of SiC and considers two distinct initial surface conditions. The first is a pure SiC surface, which refers to an unaltered SiC surface exposed directly to an oxidizing environment. The second is a passivated SiC surface, where the SiC has already formed a protective silicon dioxide (SiO_2) layer. For passive oxidation, Wagner proposed that the oxidation process is primarily governed by the diffusion of oxygen through the boundary layer surrounding the SiC material to reach the surface. Once oxygen reaches the SiC surface, it reacts to form a SiO_2 layer, as described by reaction 2.9.

Turkdogan's Extension

Turkdogan [40] expanded upon Wagner's model by incorporating additional factors that influence the oxidation process. He introduced the effects of gas flow on mass transport, recognizing the impact of convective flow on the delivery of oxygen to the SiC surface. Furthermore, his model accounts for vapor phase transport mechanisms, including the movement of volatile species such as silicon monoxide (SiO) in the gas phase. Turkdogan also incorporated surface reaction kinetics, which describe the rates of chemical reactions occurring at the SiC/SiO_2 interface [38]. These enhancements provide a more accurate description of oxidation under realistic environmental conditions where both diffusion and convection significantly contribute to the process.

The primary distinctions between Wagner's and Turkdogan's approaches are summarized in Table 2.2:

Table 2.2.: Comparison of Wagner and Turkdogan oxidation models for passive oxidation of SiC

Aspect	Wagner Model	Turkdogan Model
Oxidation Location	At the SiC surface	Within the boundary layer
Mass Transport	Diffusion only	Diffusion + Convection
Flow Effects	Not considered	Explicitly included
Reaction Kinetics	Simplified surface reactions	Detailed surface reaction kinetics

Both Wagner's and Turkdogan's models describe the formation of a passive SiO_2 layer as a sequential process. Initially, oxygen molecules adsorb onto the SiC surface, initiating localized reactions that form SiO_2 nuclei. These nuclei eventually nucleate and grow into a continuous, adherent protective layer. Over time, the SiO_2 layer thickens as oxygen continues to diffuse through the boundary layer and reacts with the underlying SiC, following a diffusion-controlled mechanism [38].

The effectiveness of the passive SiO_2 layer in protecting SiC from further oxidation depends on several factors:

- **Layer thickness**: Thicker layers provide better protection but may introduce thermal stresses.

- **Temperature**: Higher temperatures can enhance diffusion rates but may also accelerate oxidation.
- **Oxygen partial pressure**: Higher oxygen concentrations increase the oxidation rate.
- **Surface conditions**: Surface roughness and the presence of defects can influence oxidation kinetics and layer integrity [9].

SiO_2 exhibits several properties that make it a promising candidate for ABEP intake coatings in VLEO applications. When properly prepared, SiO_2 surfaces can achieve remarkably low surface roughness values of approximately 0.94 ± 0.06 Å, enabling highly specular gas-surface interactions. The material forms as a thin layer of polycrystalline alpha-quartz when exposed to hyperthermal atomic oxygen, maintaining surface roughness characteristics very close to the initial substrate roughness [10]. This oxide layer demonstrates significant chemical stability, as unsaturated hydrocarbons, water, and ammonia, which typically decompose on bare silicon surfaces, show reduced reactivity with the oxidized surface. Furthermore, experimental studies using hyperthermal beams containing atomic and molecular oxygen at speeds of approximately 5500 m/s have demonstrated that SiO_2 surfaces promote inelastic scattering with relatively focused angular distributions. The surface maintains its properties even under bombardment by reactive species at high relative velocities of several kilometers per second, making it particularly suitable for the harsh VLEO environment [10].

2.4.2.2. Formation of SiO_2 Layer and Passivation Mechanisms

The protective SiO_2 layer formed during passive oxidation acts as a barrier to further oxidation by limiting the diffusion of oxygen to the SiC surface [37]. The passivation mechanism begins with the rapid formation of a thin SiO_2 layer on the SiC surface, typically only a few nanometers thick. This initial layer grows thicker over time through diffusion-controlled processes, potentially reaching micrometer scales over extended periods. As the oxidation process continues, the amorphous SiO_2 undergoes crystallization and densification, transforming into a more stable crystalline form that enhances its protective qualities.

The SiO_2 layer is instrumental in maintaining the specular reflection properties of intake surfaces. Its uniformity and smoothness help preserve the surface characteristics necessary for efficient specular reflection, as discussed in Section 2.3.3. However, factors such as thermal cycling and exposure to atomic oxygen in VLEO can influence the effectiveness of the SiO_2 layer over time. Evaluating and improving the properties of this layer, particularly through advanced coating techniques like PECVD, is critical, as discussed in the following section.

2.5. Plasma-Enhanced Chemical Vapor Deposition Process

PECVD is a widely used technique for depositing thin films from a gas phase to a solid phase on a substrate under the influence of plasma. PECVD allows for the deposition of various materials, including SiO_2, at relatively low substrate temperatures compared to conventional Chemical Vapor Deposition (CVD), making it suitable for coating temperature-sensitive substrates [41].

2.5.1. Basic Principles

PECVD leverages plasma to enhance chemical reactions necessary for film deposition. The process enables the formation of thin films at lower temperatures, which is particularly beneficial for substrates sensitive to high thermal loads.

As illustrated in Figure 2.9, the PECVD process involves several key components and steps:

2.5.1.1. Plasma Generation and Maintenance

Plasma is generated by applying radio-frequency (RF) or microwave power to electrodes or antennas within the reaction chamber. The energy input ionizes the precursor gases, creating a plasma consisting of electrons, ions, radicals, and neutral species. The choice of frequency and power affects the plasma density and energy, influencing the deposition rate and film properties [15].

2.5.1.2. Chemical Reactions and Film Growth

The film growth in PECVD begins with the generation of reactive species. Precursor gases, such as silane and methane for SiO_2 deposition, are introduced into the chamber and dissociated in the plasma to form

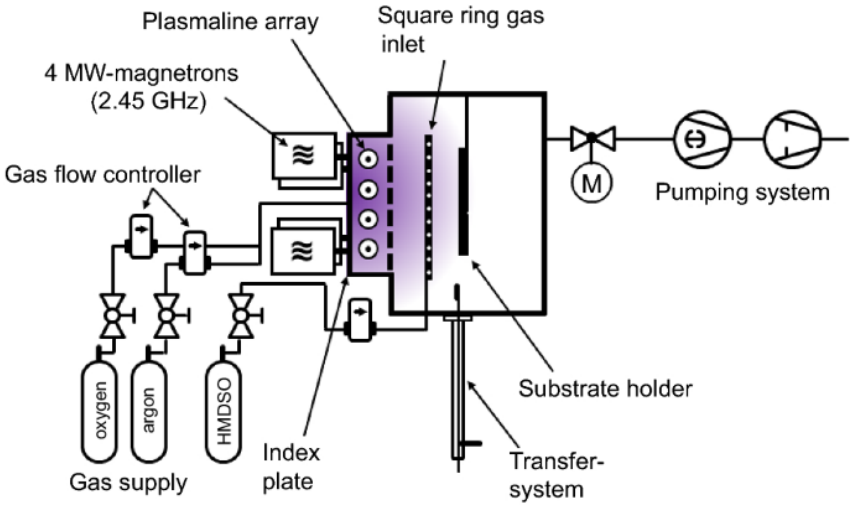

Figure 2.9.: Schematic view of the PECVD process [15].

highly reactive species. These species are then transported to the substrate surface by diffusing through the plasma. Upon reaching the substrate, the reactive species adsorb onto the surface and undergo chemical reactions, leading to the formation of a thin film. Simultaneously, volatile byproducts from these surface reactions desorb and are removed from the chamber through the vacuum system. These sequential processes enable the controlled deposition of thin films with precise properties tailored to specific applications.

2.5.1.3. Process Parameters

Key parameters influencing the PECVD process include:

- **Gas flow rates**: Control the concentration of precursor gases and reactive species, affecting film composition and deposition rate.
- **Chamber pressure**: Influences the mean free path of particles and plasma characteristics, impacting film uniformity and quality.
- **Plasma power and frequency**: Determine the energy and density of the plasma, affecting the dissociation of precursor gases and the energy of ions impinging on the substrate.
- **Substrate temperature**: Influences surface reactions, film adhesion, and microstructure.

By adjusting these parameters, the properties of the deposited films such as composition, density, microstructure, and stress can be tailored to meet specific requirements [41].

2.5.2. PECVD of SiO_2 Coatings

PECVD is particularly suitable for depositing SiO_2 coatings due to its ability to produce high-quality films at lower temperatures. Precursors such as silane (SiH_4) and methane (CH_4), or organosilicon compounds like hexamethyldisiloxane (HMDSO), are commonly used for SiO_2 deposition [15].

2.5.2.1. Advantages of PECVD SiO_2 Coatings

The PECVD process offers several advantages for depositing SiO_2 coatings:

- **Low deposition temperature**: Enables coating of substrates sensitive to high temperatures, preserving the integrity of temperature-sensitive materials.
- **Uniform film thickness**: Achieved through controlled plasma conditions and gas flow, ensuring consistent coating properties over large areas and complex geometries.
- **Good adhesion and conformality**: Plasma processes enhance film adherence to the substrate and allow for conformal coatings over intricate surfaces, which is essential for components like ABEP intake surfaces.

2.5.2.2. Applications in VLEO Environments

SiO_2 coatings deposited by PECVD can protect spacecraft surfaces from the harsh conditions in VLEO, such as AO erosion and thermal cycling. The PECVD process allows for the deposition of dense, amorphous SiO_2 films that could offer enhanced barrier properties and maintain the specular reflectivity required for ABEP intake surfaces. Maintaining specular reflectivity is crucial, as discussed in Section 2.3.3, to ensure efficient particle reflection within the intake system.

2.5.3. Relevance to ABEP Systems

The implementation of PECVD-deposited SiO_2 coatings on ABEP intake surfaces directly impacts the system's performance. As detailed in Section 2.3.3, maintaining specular reflection properties is essential for efficient particle collection and reflection within the intake. The protective SiO_2 coating not only preserves these optical properties by resisting AO-induced erosion but also enhances the intake's durability under thermal and mechanical stresses encountered in VLEO environments.

Moreover, the ability to deposit high-quality SiO_2 coatings via PECVD at relatively low temperatures allows for compatibility with a variety of substrate materials, providing flexibility in intake design and manufacturing.

2.6. High-Enthalpy Oxygen Flows and Plasma Wind Tunnel Testing

Understanding the behavior of materials like SiC under the extreme conditions of VLEO is crucial for developing durable intake coatings in ABEP systems. High-enthalpy oxygen flows and PWK3 testing provide valuable insights into material performance, oxidation mechanisms, and degradation processes. This section discusses the capabilities of the PWK3 facility at the IRS[42] of the University of Stuttgart its characteristics on providing relevant parameters that could be linked to conditions of rich AO environments that are also encountered in VLEO.

2.6.1. Overview of the PWK3 Facility at IRS Stuttgart

The PWK3 is a facility designed for atmospheric entry simulation, thermal protection system (TPS) testing, and fundamental plasma research [43, 42]. By enabling controlled experimentation under high-enthalpy plasma flows, PWK3 replicates the extreme environments encountered during atmospheric entry or can provide related conditions present in VLEO regimes, making it uniquely suited for testing materials like SiC for ABEP applications.

The facility consists of three main components:

- **Vacuum chamber**: A cylindrical vacuum chamber measuring 2 m in length and 1.6 m in diameter, equipped with optical access ports for plasma observation and diagnostics [43].
- **Inductively heated plasma generator (IPG)**: The facility can be equipped with different plasma generators—IPG3, IPG4, or IPG5—depending on experimental requirements [44, 43]. The power is coupled inductively into the gas utilizing a copper coil and a Meissner-type resonant network.
- **Support infrastructure**: Includes a high-power supply system capable of delivering up to 375 kW, a comprehensive multi-stage vacuum pump system, water cooling for critical components, and safety systems [43].

Key specifications of the PWK3 facility are summarized in Table 2.3.

2.6.2. Plasma Generation Techniques and Diagnostic Methods in PWK3

An inductively coupled plasma generator (IPG) produces the plasma in PWK3. The IPG consists of a water-cooled induction coil surrounding a quartz tube through which the working gas flows. A radio-frequency (RF) power supply feeds the induction coil, generating an alternating magnetic field that ionizes the gas within the quartz tube, creating plasma [43]. The operational frequency of the RF power supply can be adjusted between 0.5 and 1.4 MHz by changing the capacitor configuration and coil geometry [43, 44].

Different plasma generators offer varying capabilities:

Table 2.3.: Key specifications of the PWK3 facility [43, 44, 42].

Parameter	Specification
Vacuum chamber dimensions	2 m (length) × 1.6 m (diameter)
Vacuum system	Four-stage vacuum pump system
Base pressure	5 Pa
Maximum suction capacity	250,000 m^3/h at 10 Pa
Power supply	Up to 375 kW
Operational frequency range	0.5–1.4 MHz
Plasma generators	IPG3, IPG4, or IPG5
Working gases	O_2, N_2, CO_2, Air, Ar

- **IPG3**: Basic version with a compact design, featuring a transparent tube cooling system, axial optical access, and qualification for operation with pure gases like Ar and CO_2. Designed for thermal protection system (TPS) material investigations.
- **IPG4**: Distinguished from IPG3 by including an additional nozzle, enabling operation under different flow conditions.
- **IPG5**: Specifically designed to enable the use of very thin tubes and ceramic tubes. It features a split-flange design that allows for the installation of tubes with wall thicknesses under 2 mm. This version can achieve closer coil-to-plasma distances (less than 2 mm) compared to earlier versions, improving electromagnetic coupling efficiency.

Plasma parameters can be finely controlled by adjusting the RF power, gas mass flow rate, and operational frequency, enabling precise simulation of desired plasma conditions [43, 42]. Key performance specifications of the IPG3 plasma generator are provided in Table 2.4.

Table 2.4.: Performance specifications of the IPG3 plasma generator [43, 42].

Parameter	Specification
Stagnation Point Enthalpy	Up to 60 MJ/kg
Flow velocity	390 m/s (subsonic) to 6000 m/s (supersonic)
Operational pressure range	0.3–20 hPa
Oxygen partial pressure	800–3000 Pa
Surface temperature	Exceeding 2000°C
Gas mass flow rates	1.5–8 g/s
Oxygen dissociation	Near-complete dissociation possible

Temperature measurements in PWK3 employ sophisticated pyrometry systems. The Linear Pyrometer 3 (LP3) operates at a wavelength of 958.1 nm, enabling accurate surface temperature measurements within the range of 750 K to 2500 K. Complementing this, the Multiwavelength Pyrometer 3 (MP3) system utilizes both Near-Infrared (NIR) and Mid-Infrared (MIR) spectroscopes for comprehensive temperature and emissivity determination. The NIR spectroscope, implemented through an Ocean Optics NIRQuest 2.5 spectrometer, operates in the wavelength range of 0.9 µm to 2.5 µm, facilitating high-temperature measurements from 1050 K to 1930 K. The MIR spectroscope, covering wavelengths from 2.5 µm to 10 µm, extends the measurement capabilities to lower temperatures below 900 K. This integrated approach enables comprehensive characterization of both plasma properties and material behavior during high-enthalpy plasma interactions [38, 13].

2.6.3. Impact of Exposure Time on Material Degradation

Exposure time is a critical parameter in material testing within PWK3, especially for studying oxidation and erosion behaviors of materials like SiC. The duration of exposure influences several key phenomena [9, 45]:

- **Passive-active transition (PAT)**: The transition from passive to active oxidation is time-dependent and influenced by temperature, oxygen partial pressure, and flow velocity [38].
- **Surface morphology evolution**: Extended exposure can lead to changes in surface morphology, such as bubble formation at the SiC-SiO_2 interface, surface roughening, and layer spallation.

- **Thermal equilibration**: The sample temperature evolves over time, reaching a steady state, affecting oxidation kinetics and regimes [38].

Understanding the impact of exposure time is essential for predicting material behavior and lifetime in high-enthalpy environments similar to those encountered in VLEO or atmospheric entry.

2.6.4. Experimental Control of Exposure Parameters

Precise control of experimental parameters in PWK3 ensures reproducible results [43, 42]. Key parameters that are regulated include:

- **Plasma power**: Controlled via the anode voltage and RF power supply settings, directly influencing plasma temperature, ionization, and enthalpy.
- **Gas mass flow rate and composition**: Adjusted using mass flow controllers to achieve the desired gas mixture and flow rate, affecting plasma density, pressure, and composition.
- **Chamber pressure**: Regulated by the vacuum pump system and gas flow rate, affecting the mean free path of particles and flow regime. The chamber pressure also indirectly influences the stagnation pressure experienced by the sample.
- **Stagnation pressure on the sample**: The interaction between the plasma stream and the sample surface determines the stagnation pressure, which significantly affects local aerodynamic forces and heat flux on the sample.
- **Sample position**: Adjusted to control the local plasma conditions experienced by the sample, ensuring consistent exposure to the plasma flow.

2.6.5. Implications for ABEP System Design

By understanding the oxidation kinetics of SiC under high-enthalpy oxygen flows, engineers can optimize coating thickness and composition to maximize durability and maintain specular reflection properties over the intended mission lifespan. This directly impacts the performance of ABEP intake systems, as maintaining specular reflectivity is crucial for efficient particle collection and reflection within the intake, as discussed in Section 2.3.3.

The PWK3 facility at IRS Stuttgart offers a unique platform for investigating material behavior in high-enthalpy, reactive gas flows. While acknowledging the limitations in directly replicating VLEO conditions, the controlled environment and diagnostic capabilities of PWK3 make it an invaluable tool for advancing ABEP technology and ensuring the robustness of materials used in these systems.

2.7. Surface Analysis Techniques

To evaluate the effects of high-enthalpy oxygen plasma exposure on SiC surfaces, advanced surface analysis techniques are employed. These techniques provide detailed insights into surface morphology, roughness, composition, and structural changes from the micro to nanoscale levels. The primary methods used in this work include Nomarski Microscopy, AFM, and Atomic Force Microscopy (AFM).

2.7.1. Surface Roughness Theory

Surface roughness is a critical parameter influencing material performance, particularly in environments like VLEO where surface interactions significantly affect material behavior. Surface roughness impacts reflection properties, oxidation rates, thermal resistance, and overall durability[10].

2.7.1.1. Surface Roughness Parameters

Surface roughness is quantified using standardized parameters that describe the deviations of a surface from its ideal form. The most commonly used parameters are:

Arithmetic Mean Roughness (R_a)
The arithmetic mean roughness, R_a, is a fundamental metric for quantifying surface texture, representing the average of the absolute deviations of the surface height from the mean plane over a specified sampling length or area [46]. When applied to a profile, or line measurement, R_a is mathematically defined as:

$$R_a = \frac{1}{L} \int_0^L |Z(x)| \, dx \tag{2.11}$$

In this expression, L denotes the evaluation length along the x-axis, measured in meters, while $Z(x)$ represents the surface height deviations from the mean plane at a given position x, expressed in micrometers (μm). The integral averages the absolute deviations along the profile length.

For a surface area measurement, the arithmetic mean roughness is extended to S_a, which evaluates the mean absolute deviations over a specified area. This is expressed as:

$$S_a = \frac{1}{A} \iint_A |Z(x, y)| \, dx \, dy \tag{2.12}$$

Here, A is the total evaluation area measured in square meters, and $Z(x, y)$ denotes the surface height deviations from the mean plane at a given point (x, y), again measured in micrometers (μm). The double integral captures the average deviation across the entire surface area, providing a two-dimensional extension of the R_a concept.

These definitions ensure that both profile-based and area-based measurements provide a standardized approach to evaluating surface texture, facilitating comparability across different applications and materials.

Root Mean Square Roughness (R_q)

Also known as RMS (Root Mean Square) roughness, R_q is the square root of the mean of the squares of the surface deviations [46].

For a profile:

$$R_q = \sqrt{\frac{1}{L} \int_0^L [Z(x)]^2 \, dx} \tag{2.13}$$

For a surface:

$$S_q = \sqrt{\frac{1}{A} \iint_A [Z(x, y)]^2 \, dx \, dy} \tag{2.14}$$

Ten-Point Mean Roughness (R_z)

The ten-point mean roughness, R_z, is calculated by averaging the sum of the five highest peaks and the five deepest valleys over the sampling length [46].

$$R_z = \frac{1}{5} \left(\sum_{i=1}^{5} Z_{p_i} + \sum_{j=1}^{5} |Z_{v_j}| \right) \tag{2.15}$$

where Z_{p_i} are the heights of the five highest peaks and Z_{v_j} are the depths of the five deepest valleys.

2.7.1.2. Units of Measurement

Surface roughness parameters are commonly expressed in micrometers (µm), which are well-suited for most industrial applications. For surfaces requiring higher precision, particularly at the nanometer scale, roughness is measured in nanometers (nm), providing detailed characterization of surface features at a finer resolution.

2.7.1.3. Measurement and Quality Control

The precise measurement of surface roughness is fundamental for effective quality control. Advanced profilometry techniques, such as WLIM and AFM, provide highly accurate assessments of roughness parameters. Ensuring consistency and reliability in measurements is further supported by adherence to established standards, such as ISO 21920, which provide a robust framework for uniform evaluation [46].

2.7.1.4. Manufacturing Considerations

The preparation of high-quality surfaces for metallurgical and microscopic analysis demands meticulous attention to detail and the use of advanced techniques. Among these, metallographic diamond suspension polishing stands out for its ability to produce defect-free surfaces essential for precise characterization.

Metallographic Diamond Suspension Polishing

Metallographic suspension polishing with diamond suspension is an advanced technique for preparing metallurgical samples with high-quality, defect-free surfaces suitable for microscopic analysis. This method involves mounting multiple samples simultaneously in a holder using a thermosetting adhesive, enabling uniform and efficient polishing. The polishing process employs diamond particles suspended in a carrier medium, which remove material through micro-cutting and plowing actions [47].
Polycrystalline diamonds, composed of numerous sub-micron crystallites, offer uniform abrasion and enhanced performance due to their resistance to microfracturing. Key process parameters include the concentration and uniform distribution of diamond particles, as well as the selection of appropriate lubricants to ensure optimal contact between the diamonds and the sample surface [47]. The polishing sequence typically progresses through the following stages:

- **Initial polishing**: Utilizes coarser diamond particles (15–9 μm) for primary material removal.
- **Intermediate polishing**: Employs medium-sized particles (9–3 μm) to eliminate deformation.
- **Final polishing**: Uses fine particles (3–0.5 μm) to achieve the desired surface finish.

Surface quality is further enhanced by polycrystalline diamonds, which minimize scratches and microcracking while ensuring superior flatness and uniformity. This method is highly valued for its efficiency, exceptional surface quality, and applicability to a wide range of metallic materials. However, considerations regarding the cost of diamond abrasives and the necessity for specialized equipment must be addressed to optimize its implementation [47, 48].

2.7.2. Nomarski Microscopy

Nomarski microscopy, also known as Differential Interference Contrast (DIC) microscopy, is an advanced optical technique introduced by Georges Nomarski in 1955 [49]. It enhances contrast in unstained, transparent samples by converting phase shifts in light passing through the sample into amplitude differences, which can be visualized as variations in image intensity. This method is particularly advantageous in materials science and engineering for analyzing minute variations in surface topography [50].

2.7.2.1. Principle of Operation

The fundamental principle of Nomarski microscopy is based on interference contrast. The technique employs polarized light and specialized optical components, including polarizers, analyzers, and a modified Wollaston prism known as a Nomarski prism, to split and recombine light beams [51].

The operation consists, as illustrated in Figure 2.10, of the several essential steps:

- **Polarization of light**: Unpolarized light from the illumination source is passed through a polarizer to produce plane-polarized light.
- **Beam splitting**: The polarized light enters the Nomarski (Wollaston) prism, which splits it into two orthogonally polarized beams that are laterally sheared by a small distance, typically less than the resolving power of the objective lens.
- **sample interaction**: These two beams traverse the sample along closely adjacent paths. Variations in the sample's optical path length—due to differences in refractive index or thickness—introduce phase shifts between the beams.
- **Recombination and interference**: After passing through the sample, the beams are recombined by a second Nomarski (Wollaston) prism. An analyzer, oriented perpendicular to the initial polarizer, forces the orthogonally polarized beams to interfere.
- **Image formation**: The interference of the beams converts the phase differences into amplitude variations, resulting in an image with enhanced contrast that accentuates gradients in optical path length [50].

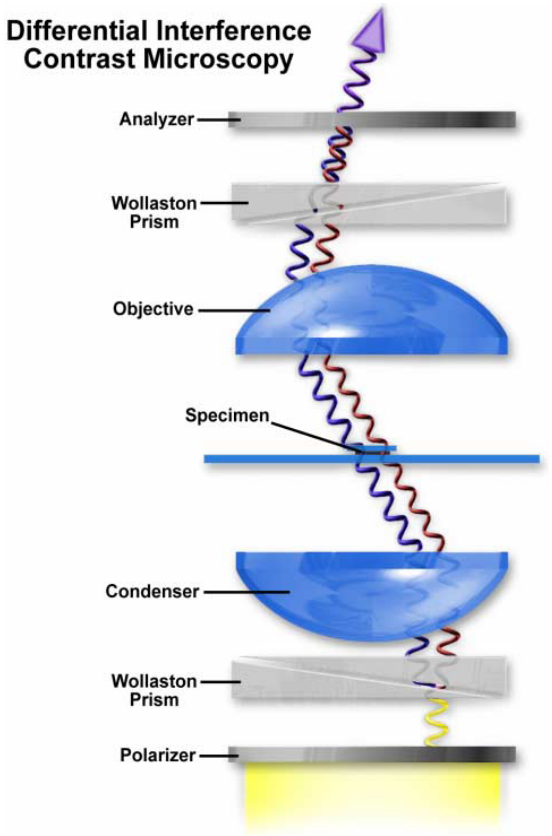

Figure 2.10.: Schematic diagram of a Nomarski microscope setup, illustrating the light path and the role of the Nomarski prism [51].

2.7.2.2. Image Formation and Contrast Mechanism

Nomarski microscopy is sensitive to the gradients of optical path length rather than absolute values, making it particularly effective for detecting edges and fine surface details. The lateral shear between the beams causes the interference contrast to be proportional to the rate of change of optical path difference across the sample [50]. This results in images with a characteristic pseudo-relief appearance, where height differences are translated into intensity variations, providing a three-dimensional visual effect. The technique enhances contrast without introducing halos or shading artifacts common in other phase contrast methods.

2.7.2.3. Advantages of Nomarski Microscopy

Nomarski microscopy offers several significant advantages, making it a powerful tool in imaging and analysis. By utilizing the full numerical aperture of the objective lens, it provides high spatial resolution for detailed imaging. The technique is non-destructive and non-contact, ensuring the preservation of delicate samples. It enhances contrast effectively, enabling the visualization of transparent or unstained samples with subtle optical variations. Furthermore, Nomarski microscopy has optical sectioning capability, allowing for improved depth discrimination in thick samples. With proper calibration, it also supports quantitative analysis, facilitating measurements of optical path differences and surface slopes [50].

2.7.3. White Light Interferometry Microscopy

WLIM is a non-contact optical profiling technique used to measure surface topography with nanometer-scale vertical resolution [52]. By utilizing broadband (white light) illumination, WLIM generates interference patterns that are highly sensitive to surface height variations, making it an invaluable tool for precise surface characterization in materials science and engineering.

2.7.3.1. Principle of Operation

The fundamental principle of WLIM is based on low-coherence interferometry. The technique employs a Michelson or Mirau interferometer configuration to split the incoming white light into two beams: a reference beam and a sample beam [53, 54].

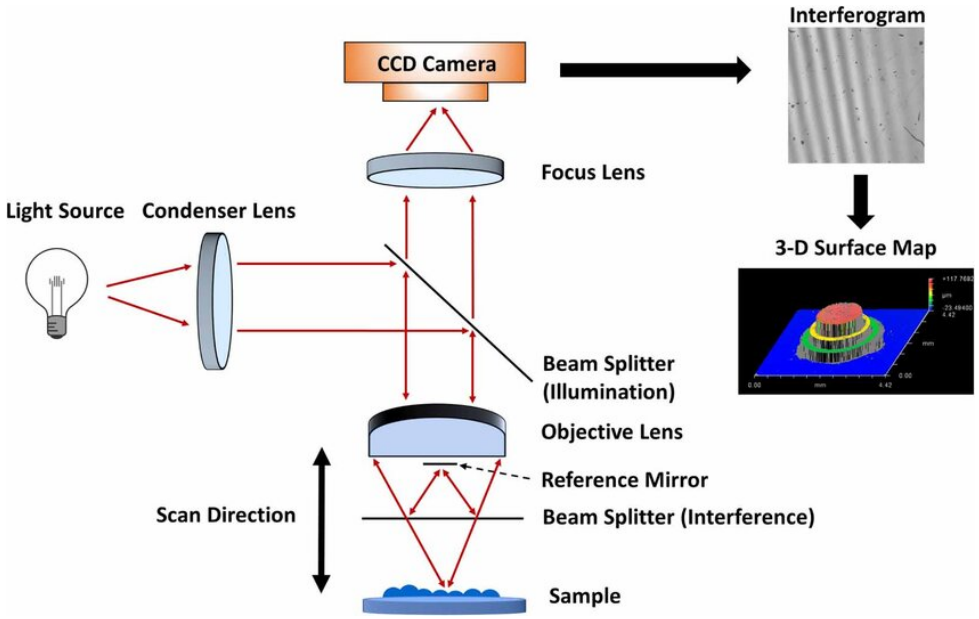

Figure 2.11.: Schematic diagram of a White Light Interferometry setup illustrating the key components and light paths [55].

The operation involves the following steps:

- **Beam splitting**: A broadband light source is directed into the interferometer, where a beam splitter divides it into the reference and sample beams.
- **Reflection**: The sample beam reflects off the test surface, while the reference beam reflects off a reference mirror with a known position.
- **Recombination and interference**: The reflected beams are recombined at the beam splitter, producing an interference pattern due to the optical path difference between the two beams.
- **Vertical scanning**: The optical path difference is varied by moving either the sample or the reference mirror vertically using a precision piezoelectric scanner.
- **Fringe localization**: Due to the low coherence length of white light, interference fringes are observed only when the optical path lengths of the two beams match within the coherence length, effectively localizing the fringes to specific surface heights.
- **Data acquisition**: A charge-coupled device (CCD) or complementary metal-oxide-semiconductor (CMOS) camera captures the interference pattern at each scan position.
- **Surface reconstruction**: Advanced signal processing algorithms analyze the interferograms to determine the exact height of each point on the surface, constructing a three-dimensional surface map [52].

2.7.3.2. Advantages of WLIM

WLIM, as a surface metrology technique, offers the non-contact and non-destructive capability to analyze delicate or easily deformed surfaces. It achieves vertical resolutions better than 1 nm and operates over a large measurement range, accommodating surfaces with height variations from nanometers to millimeters. The technique is characterized by fast data acquisition, typically completing measurements within seconds to minutes. Its versatility makes it suitable for a wide variety of materials and surface types. Furthermore, WLIM eliminates the 2π phase ambiguity inherent in monochromatic interferometry due to the use of white light [52].

This non-contact, high-resolution technique is essential for analyzing SiC surface topography during oxidation, accurately capturing subtle surface changes in high-temperature oxidizing environments and providing critical insights to enhance SiC-based aerospace components.

2.7.4. Atomic Force Microscopy

AFM has emerged as a pivotal technique for nanoscale surface analysis since its invention by Binnig, Quate, and Gerber in 1986 [56]. AFM provides high-resolution imaging and quantitative measurements of surface properties, enabling the investigation and manipulation of materials at the atomic and molecular levels. Its versatility allows operation in various environments, including air, vacuum, and liquids, making it indispensable in fields ranging from materials science to biology [57].

2.7.4.1. Principle of Operation

AFM operates by detecting the forces between a sharp probe tip and a sample surface. The core component is the cantilever-tip assembly, also known as the *probe*, which interacts with the sample through a raster scanning motion. The deflection of the cantilever due to tip-sample interactions is monitored using a laser beam reflected off the back of the cantilever onto a position-sensitive photodetector (PSPD). By tracking the vertical and lateral motions of the probe, a high-resolution three-dimensional topographic map of the surface is constructed [58].

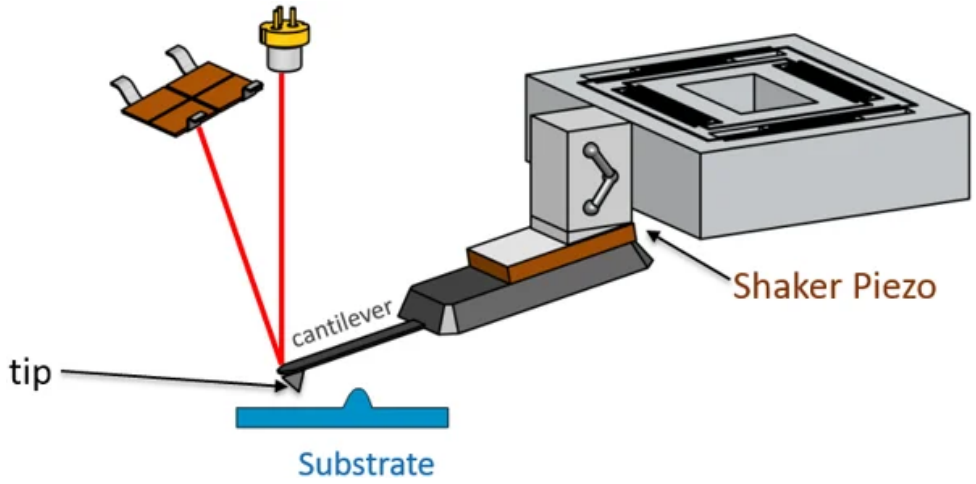

Figure 2.12.: Schematic diagram of AFM operation principle [58].

The cantilever-tip assembly consists of a very sharp tip, typically with a radius of curvature between 5 and 10 nm, mounted at the end of a flexible cantilever. The cantilever is usually fabricated from silicon or silicon nitride, with geometries commonly being rectangular (diving-board) or triangular. The dimensions of the cantilever—width (w), thickness (t), and length (L)—are critical as they determine the spring constant (k) of the cantilever, which governs the interaction between the tip and the sample surface. The spring constant for a rectangular cantilever is given by:

$$k = \frac{Ewt^3}{4L^3}, \tag{2.16}$$

where E is the Young's modulus of the cantilever material. Accurate knowledge of the spring constant is essential for quantitative force measurements and is typically provided by the vendor, though actual values may vary and require calibration [58].

The deflection of the cantilever is detected via the optical lever method. A laser beam is reflected off the back of the cantilever onto a PSPD. Small deflections cause changes in the position of the reflected laser spot on the detector, which are converted into electrical signals proportional to the deflection. Calibration of the deflection sensitivity is essential for converting these signals into units of nanometers [57].

Figure 2.13.: View of the cantilever after fine approach (side view on the left and top view on the right) [57].

2.7.4.2. Modes of Operation

AFM can be operated in several modes, each utilizing different tip-sample interaction regimes:

- **Contact mode**: In contact mode, the tip remains in continuous contact with the sample surface, and the cantilever deflection serves as the feedback parameter. This mode is suitable for imaging hard surfaces but can exert significant lateral forces, potentially damaging soft or delicate samples [58, 59].
- **Tapping mode**: Tapping mode, or intermittent contact mode, is a dynamic mode that involves oscillating the cantilever near its resonance frequency so that the tip intermittently contacts the sample surface. This reduces lateral forces and minimizes sample damage. The oscillation amplitude of the cantilever is used as the feedback parameter [58]. Tapping modes can be categorized into resonant modes and off-resonant modes.
- **Non-contact mode**: In non-contact mode, the cantilever oscillates near its resonance frequency without making physical contact with the sample. The tip senses long-range attractive forces, such as van der Waals interactions, providing high-resolution imaging while minimizing sample perturbation [59].

2.7.4.3. Calibration Techniques

Accurate AFM measurements require meticulous calibration of system parameters.

Deflection Sensitivity Calibration

Deflection sensitivity calibration (Figure 2.14) converts the voltage measured by the photodetector into nanometers of cantilever deflection. This is performed by acquiring a force-distance curve on a hard, non-deformable surface (e.g., sapphire). The slope of the linear (repulsive) region of the contact portion of the curve represents the deflection sensitivity [58].

Spring Constant Calibration

Calibration of the spring constant of rectangular cantilevers is performed via the Sader method, which is implemented across various AFM product lines [60]. This method relies on inputting the length and width of the cantilever, typically provided by the vendor. A thermal noise spectrum of the cantilever is recorded, where the room temperature thermal motion drives the cantilever. A single harmonic oscillator model is used to fit the peak in the thermal spectrum, extracting the resonance frequency and quality factor. These parameters are then input into the Sader model for hydrodynamic damping to calculate the spring constant. Alternatively, a frequency sweep using a shaker piezo can be used, provided the cantilever is retracted at least 100 μm from the surface to avoid interaction during the measurement [60].

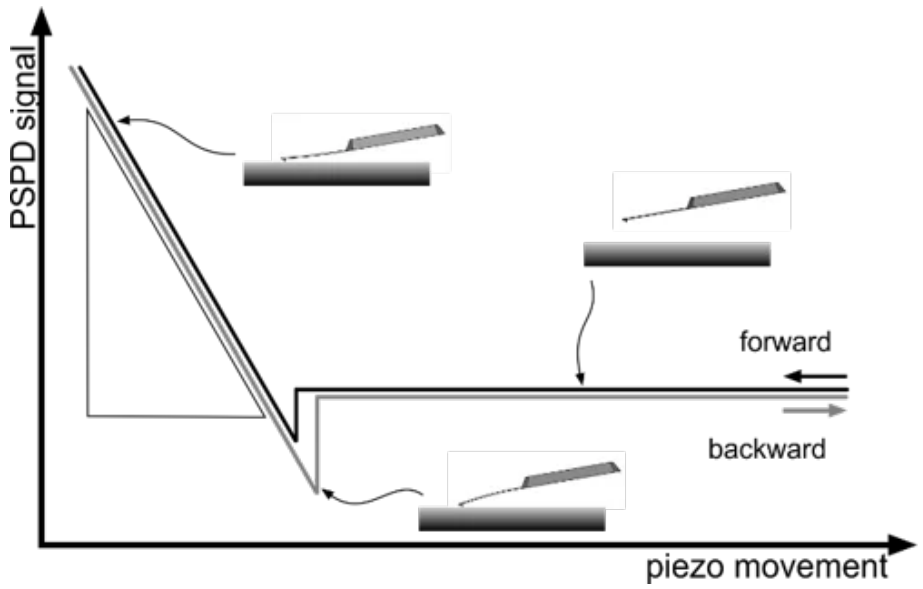

Figure 2.14.: Force-distance curve used for deflection sensitivity calibration [58].

2.7.4.4. Feedback Control in AFM

AFM utilizes a feedback loop to maintain a stable interaction between the probe tip and the sample surface. This feedback system dynamically adjusts the vertical position of the scanner (z-piezo) to keep a specific feedback parameter, such as cantilever deflection or oscillation amplitude, constant at a predefined setpoint.

PID Control

The feedback loop is primarily governed by a Proportional-Integral-Derivative (PID) controller. The PID controller modulates the scanner position based on the error signal, which is the difference between the measured feedback parameter and its setpoint. The performance and stability of the feedback system depend critically on the tuning of the PID gains:

- **Proportional gain (P)**: Responds proportionally to the current error, providing an immediate corrective action.
- **Integral gain (I)**: Accumulates past errors to eliminate steady-state discrepancies, ensuring accurate long-term tracking.
- **Derivative gain (D)**: Predicts future errors by analyzing the rate of change of the error, enhancing the system's responsiveness.

Proper calibration of the PID gains is essential for optimal performance. If the gains are set too low, the system may exhibit slow response and inadequate tracking of surface features. Conversely, excessively high gains can induce oscillations and introduce noise into the imaging process. Among the PID components, the integral gain plays a pivotal role in image quality, while the proportional and derivative gains contribute to the refinement and stability of the feedback loop [58].

2.7.5. Scanning Electron Microscopy and Energy-Dispersive X-ray Spectroscopy

SEM coupled with EDX represents a powerful analytical methodology for both morphological and elemental characterization of materials at the microscale. This integrated system enables researchers to obtain high-resolution imaging while simultaneously performing quantitative elemental analysis [61]. SEM-EDX is widely utilized across various scientific and engineering disciplines due to its ability to provide detailed information about the surface topography, composition, and properties of materials. This section delves into the fundamental principles, quantitative analysis capabilities, technical considerations, advantages, and diverse applications of SEM-EDX in engineering studies.

2.7.5.1. Fundamental Principles

Electron-Matter Interactions

The interaction of the high-energy primary electron beam with the sample generates several types of signals, including secondary electrons (SE), backscattered electrons (BSE), and characteristic X-rays. These signals are critical for SEM and EDX analysis, providing complementary information about the sample's surface topography, composition, and atomic structure [61].

X-ray Generation and Detection

As the high-energy electron beam interacts with atoms in the sample, it can eject inner-shell electrons, creating vacancies. When electrons from higher energy levels fill these vacancies, characteristic X-rays are emitted. These X-rays are detected by energy-dispersive detectors, such as silicon drift detectors (SDDs), which convert them into electrical pulses proportional to their energies [61]. This process enables both qualitative and quantitative elemental analysis.

2.7.5.2. Principle of Operation

Scanning Electron Microscopy

SEM functions by directing a focused beam of electrons generated by the electron gun onto the sample surface. The beam is finely focused using condenser and objective lenses and is scanned across the sample in a raster pattern using electromagnetic scan coils. This interaction generates a range of signals, which are captured by specialized detectors (e.g., SE and BSE detectors) to produce high-resolution images. These images provide valuable insights into the sample's surface morphology, composition, and microstructural details [62].

Components and Signal Detection

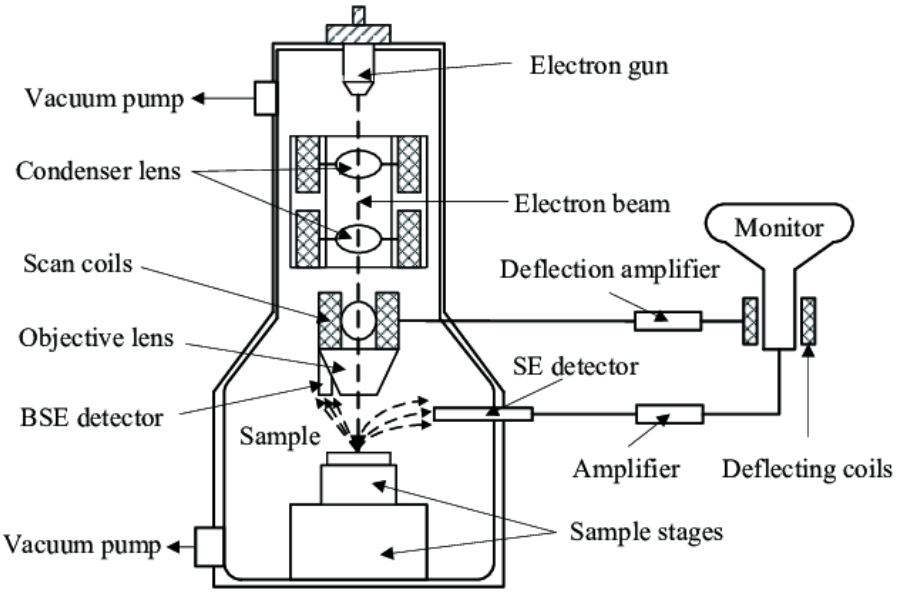

Figure 2.15.: Schematic diagram of a SEM illustrating the key components, electron beam path, and signal detection systems [63].

As illustrated in Figure 2.15, the SEM consists of several critical components:

- **Electron source (electron gun):** Generates a beam of high-energy electrons, serving as the primary probe in SEM imaging.
- **Electromagnetic lenses (condenser and objective lenses):** Focus and refine the electron beam to produce a narrow, precise spot on the sample, ensuring high spatial resolution.

- **Scanning coils:** Control the deflection of the focused electron beam, enabling raster scanning across the sample surface for image acquisition.
- **Sample stage:** Supports and positions the sample within the vacuum chamber, allowing for precise adjustments in multiple axes (e.g., X, Y, Z, tilt, and rotation).
- **Detectors:**
  - **Secondary lectron (SE) detector:** Captures low-energy secondary electrons emitted from the sample surface, producing detailed surface topography images.
  - **Backscattered electron detector (BSE):** Detects elastically scattered electrons with higher energies, providing compositional contrast based on the atomic number of elements in the sample.
- **Display and signal amplification systems:** Amplify, process, and visualize detected signals on a monitor, generating high-resolution images for analysis and interpretation.

Vacuum System

A vacuum environment, maintained by vacuum pumps, is critical for SEM operation to minimize electron scattering and ensure a stable electron beam. This vacuum enables efficient interaction between the electron beam and the sample, free from interference by air molecules. Importantly, to preserve the integrity of the sample, it is necessary that the SEM/EDX system used does not require gold coating. This preserves the sample's integrity and prevents surface destruction, which is crucial for subsequent analyses or applications.

Energy-Dispersive X-ray Spectroscopy

EDX is an analytical technique used in conjunction with SEM for elemental analysis and chemical characterization of a sample. When the high-energy electron beam interacts with the sample, it can excite electrons in inner atomic shells, ejecting them and creating electron holes. Electrons from higher-energy shells then fill these holes, releasing energy in the form of X-rays. The energy of these X-rays is characteristic of the atomic structure of the emitting element, allowing for identification and quantification of the elements present in the sample.

The intensity of the detected X-rays is measured in counts per second per electron volt (cps/eV), which quantifies the number of X-ray photons detected within a specific energy range during a defined time interval. The unit "cps/eV" reflects the detector's efficiency and is crucial for generating an X-ray spectrum. The spectrum plots the number of counts (cps) as a function of photon energy (eV), where characteristic peaks correspond to the energy levels of elements in the sample. This metric facilitates accurate quantitative and qualitative analysis, as it allows researchers to discern element-specific signals from background noise.

The key components of an EDX system include an X-ray detector, typically a silicon drift detector, which captures the emitted X-rays; a pulse processor that converts the X-ray signals into measurable electronic pulses; and an analyzer, which is responsible for data collection and analysis to identify and quantify the elements present in the sample.

2.7.5.3. Advantages of SEM-EDX

The combination of SEM and EDX offers several advantages for materials characterization:

- **High spatial resolution**: SEM can achieve nanometer-scale resolution, allowing for detailed examination of surface features and microstructures [62].
- **Large depth of field**: SEM images have a large depth of field, providing three-dimensional-like images of the sample surface.
- **Versatility**: SEM-EDX can analyze a wide range of materials, including metals, ceramics, polymers, and biological samples.
- **Non-destructive analysis**: In most cases, SEM-EDX analysis is non-destructive, preserving the sample for further studies.
- **Simultaneous imaging and elemental analysis**: The integration of EDX with SEM allows for correlating morphological features with elemental composition.
- **Rapid data acquisition**: Modern SEM-EDX systems can acquire high-quality images and elemental maps in minutes [61].

- **Minimal sample preparation**: Many samples can be analyzed with little or no preparation, especially when using variable pressure or environmental SEM modes.

Building on this comprehensive theoretical foundation, the next chapter will detail the experimental methodology employed in this Master Thesis, outlining the preparation, testing, and analysis procedures integral to achieving the research objectives.

3. Experimental Methodology

This chapter outlines the comprehensive experimental setup designed to evaluate the suitability of materials for ABEP intake systems. It includes details on the preparation, handling, and storage of SiC and Au-Ni samples, the plasma exposure tests conducted in PWK3, and the advanced surface analysis techniques employed to assess oxidation and surface morphology. Each methodology is tailored to ensure accuracy and reproducibility.

3.1. Sample Specifications and Preparation

This section provides detailed specifications and properties of the samples utilized in this work. It aims to clarify the origins and characteristics of the materials involved, ensuring a comprehensive understanding of the research basis and its findings.

3.1.1. SiC Samples from Previous Studies

The SiC samples from previous studies are composed of sintered SiC, each fabricated to meet ESA standard specifications A.2, including a diameter of 26.5 mm. The samples are labeled as Kaiser-1, Kaiser-2, Massuti-1, and Kaiser-3, reflecting the surnames of the researchers who conducted prior testing. These samples underwent exposure tests in the PWK3 at the IRS in Stuttgart, conducted by Clemens Kaiser [12, 13] and Bartolomeu Massuti.

Table 3.1 presents a detailed summary of the exposure conditions for each SiC sample tested in the PWK3 facility.

Table 3.1.: Detailed information of SiC exposure tests from previous studies

Sample #	**Test ID**	**Max Temperature T_{max} (K)**	**Duration (min)**	**Mass Flow (g/s)**
Kaiser-1	089	1350	20.0	3.21
Kaiser-1	090	1350	13.0	3.21
Kaiser-1	091	1350	13.0	3.21
Kaiser-2	103	1380	12.17	3.21
Kaiser-2	104	1380	11.33	3.21
Kaiser-2	105	1380	10.0*	3.21
Massuti-1	N/A	1400	20.0*	3.21
Kaiser-3	192	1388	8.87	3.21
Kaiser-3	194	1388	10.0	4.82

* Values marked with an asterisk are approximate and may contain uncertainties due to missing data.

3.1.2. New Polished SiC Samples

After evaluating various SiC options, StarCeram S (Pressureless Sintered Silicon Carbide) from Kyocera Fineceramics was identified as the optimal choice due to its exceptional mechanical and thermal properties aligning with the specific requirements of this work. Upon procurement, the SiC samples underwent an additional precision polishing phase at the IMTCCC at the University of Stuttgart. The primary goal of this polishing process was to achieve a surface roughness below 0.1 nm (approximately 1 Å). This level of roughness is particularly significant for ABEP intake applications, as it directly influences gas-surface interaction dynamics [10]. All details about communications with Kyocera Fineceramics and IMTCCC are available in the relative document available as a separate file included with the Master Thesis.

A total of six samples were procured for this research. They are conforming to the standard dimensions established by IRS A.6. The samples are labeled as IRS-01, IRS-02, IRS-03, IRS-04, IRS-05, and IRS-06. A detailed drawing of the samples is available in Appendix A.6.

3.1.2.1. Material Properties

StarCeram® S is a pressureless sintered SiC renowned for its outstanding mechanical and thermal characteristics. The material comprises 70 wt% silicon (Si) and 30 wt% carbon (C), resulting in a black, anthracite-colored appearance. The key mechanical and thermal properties of StarCeram S are summarized in Table 3.2.

Table 3.2.: Key mechanical and thermal properties of StarCeram S [64].

Property	**Value**
Density	$3.13\,\mathrm{g/cm^3}$
Closed Porosity	$> 2\,\mathrm{vol\%}$
Flexural Strength $\sigma_{b4,m}$ (RT)	375 MPa
Weibull Modulus (RT)	> 10
Young's Modulus (RT)	395 GPa
Fracture Toughness (ICL)	$3\,\mathrm{MPa}\sqrt{\mathrm{m}}$
Thermal Conductivity (RT)	$125\,\mathrm{W/(m{\cdot}K)}$
Thermal Expansion Coefficient CTE (RT-1,000°C)	$4.5 \times 10^{-6}/\mathrm{K}$
Hardness (DPH)	25 GPa
Thermal Shock Coefficient R1	180 K
Maximum Working Temperature	1,600 °C
Specific Resistance	$> 10^4\,\Omega\mathrm{cm}$

3.1.2.2. Manufacturing Process

The production of StarCeram S involves mixing SiC powder with binders and ceramic oxides, followed by pressureless sintering. During sintering, primary contamination may occur at the granule bonding stage, potentially introducing trace metal impurities. To address this, the samples undergo ultrasonic cleaning to effectively eliminate residual contaminants. Post-cleaning, the samples are packaged in polyethylene or polypropylene bags with zip seals to ensure they remain contamination-free during storage and transportation. Impurity levels are low, ranging between 60 and 80 ppm, predominantly consisting of metals such as aluminum (Al), titanium (Ti), copper (Cu), iron (Fe), and boron (B). The critical surface (the upper surface with the smallest diameter) achieves a final surface roughness (R_a) of 1 μm or better.

3.1.2.3. Polishing Procedures

The SiC samples were polished at the IMTCCC, achieving a significant improvement in surface roughness (R_a) from initial values of 1 μm to a range between 10 nm and 20 nm. Polishing was performed using metallographic suspension polishing with diamond suspension 2.7.1.4. Due to the polishing process, there might be slight variations in the tilt of the critical surface among the samples, potentially up to 1 or 2 degrees.

3.1.3. Intake Samples and PECVD Coating

After evaluating various mirror manufacturing companies, Medialario S.r.l. and Wielandts UPMT were identified as potential suppliers for the intake samples. Ultimately, two samples were procured from Medialario S.r.l., designated as 807-6 and 368-12. These samples are fabricated using Medialario's proprietary Repli-formed Optics™ technology, which enables the formation of high-precision mirrors on a mold A.1. The samples have a declared surface roughness of 0.3 nm as per the company's specifications.

3.1.3.1. Fabrication Process

The Medialario s.r.l Repli-formed Optics™ technology [65] involves several critical steps to ensure the structural integrity and optical quality of the final product.

The mirrors consist of a thin gold layer (the critical surface) adhered to a nickel alloy substrate. The gold layer serves as the reflective surface, while the underlying alloy provides the necessary rigidity and structural support. This composition ensures high reflective properties suitable for high-precision optical applications, such as X-ray telescopes. The same materials were used for the realization of the GIADA dust analyzer for the ESA Rosetta mission [66].

The fabrication process, explained in mode extensive version in Appendix A.1, can be summarized in the following steps:

- **Mandrel preparation**: Manufacturing and polishing the mandrel to achieve the desired surface smoothness.
- **Release agent application**: Coating the mandrel to facilitate later separation of layers.
- **Gold coating**: Deposition of the reflective gold layer onto the mandrel.
- **Nickel alloy electroforming**: Electrochemical formation of the structural alloy layer onto the gold-coated mandrel.
- **Cooling and separation**: Removal of the mirror from the mandrel after cooling.
- **Reuse of mandrel**: The mandrel can be reused for multiple mirror productions.
- **Final mirror**: Production of a high-quality, gold-coated, nickel-based mirror.

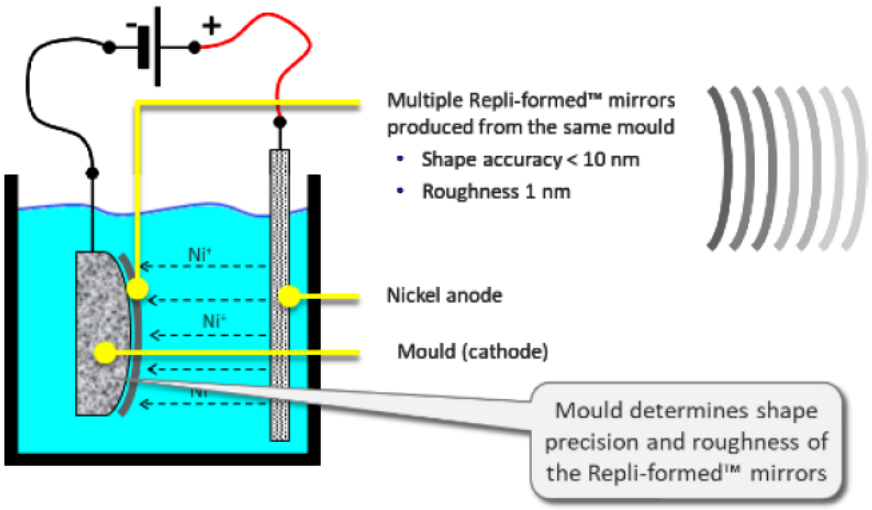

Figure 3.1.: Medialario Repli-formed Optics™ technology [65].

The surface quality of the final mirrors is highly dependent on the precision of the mandrel. Any imperfections on the mandrel are replicated in the electro-formed nickel shell. Maintaining a high-quality mandrel is crucial for ensuring the quality of the mirrors.

Both samples are cylindrical with a diameter of 50 mm and a thickness of 0.5 mm. They are fabricated using the same process but utilizing different mandrels for production.

3.1.3.2. SiO_2 Coating Procedures

The SiO_2 coating of the Gold-Nickel Intake Samples was performed at the Institut für Kunststoffverarbeitung (IKV) at RWTH Aachen using Plasma-Enhanced Chemical Vapor Deposition (PECVD). Although the IKV reactor was primarily designed for plastic coatings, it was adapted to meet the specific requirements of metallic substrates. The coating process was conducted outside a cleanroom environment, which may have introduced surface contamination affecting the uniformity and quality of the SiO_2 film.

The PECVD process was carried out in a low-pressure plasma reactor (see Figure 3.2) designed for precise control over deposition parameters. Microwave power, set to 3500 W, was utilized to generate a stable and uniform plasma essential for activating the precursor gases and facilitating the deposition of SiO_2 onto the substrate surface. To manage energy input and minimize thermal stress on the substrates, the microwave was pulsed with an on-time of 4 ms and an off-time of 100 ms.

The PECVD deposition was conducted under specific gas flow rates and pressure conditions to ensure the formation of high-quality SiO_2 layers. Hexamethyldisiloxane (HMDSO) was introduced at a flow rate of 4

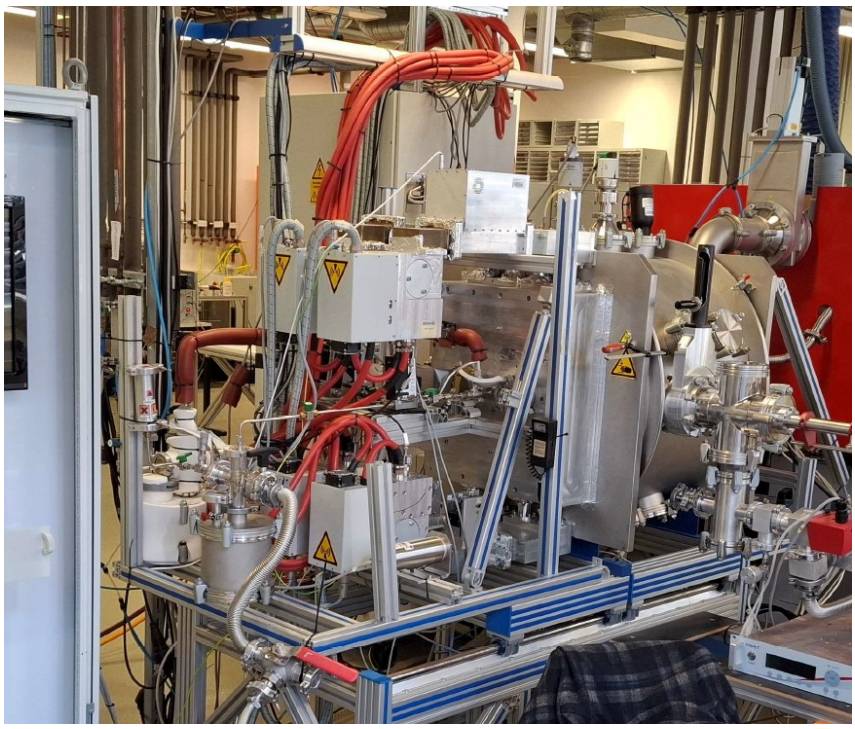

Figure 3.2.: Plasma reactor at RWTH Aachen used for the PECVD process [67].

sccm, while oxygen was supplied at 472 sccm. The presence of oxygen played a critical role in forming the silicon oxide layers [68, 41]. The absolute pressure within the reaction chamber was maintained at 5 Pa to optimize the deposition process.

The coating process was conducted over a duration of 400 seconds, based on preliminary experiments to achieve the desired coating thickness while maintaining film quality. The deposited SiO_2 layer reached an approximate thickness of 40 nm, which might be suitable for providing protective properties without significantly altering the substrate's characteristics [68, 41].

Several challenges were encountered during the PECVD process. The initial condition of the Gold-Nickel intake samples, including surface scratches and potential contamination from the non-cleanroom environment, posed challenges for achieving optimal coating quality. These imperfections can impact the adhesion and uniformity of the deposited SiO_2 layer. Additionally, the current reactor setup has limitations regarding the size of components it can accommodate. For larger geometries, such as future intake components, further modifications or alternative facilities may be necessary to ensure uniform coating across larger surfaces.

3.2. Sample Handling and Storage

The handling and storage of SiC and Gold-Nickel Intake samples were meticulously conducted within a controlled cleanroom environment at the German Aerospace Centre's (DLR) Institute of Technical Physics in Stuttgart. This process utilized essential materials and adhered to a systematic procedure to ensure the integrity and low contamination condition of the samples, in accordance with ISO 14644-5:2004 guidelines [69].

3.2.1. Utilized Materials

Table 3.3 lists the materials and items necessary for the handling and storage procedures.

Table 3.3.: Materials for sample handling and storage

Category	Items
Cleanroom Supplies	– Cleanroom-grade lint-free wipes – Powder-free nitrile gloves – Complete cleanroom attire (lab coat, hairnets, shoe covers, mask)
Cleaning Agents	– High-purity compressed air and nitrogen gas – Isopropyl alcohol (IPA), $\geq$99% purity – 10% hydrochloric acid (HCl) solution (optional)
Tools and Equipment	– Clean, non-contaminating tweezers and sample holders – Transparent transportation containers – Sterilized, dust-free Petri dishes – Antistatic bags for sample protection

3.2.2. Sample Holder and Alignment

Dust-free Petri dishes and transparent cylindrical containers provided by the cleanroom at DLR were used as sample holders during surface analysis. To ensure accurate analysis, the alignment of the samples within the holders was crucial. Two perpendicular Cartesian axes were drawn on each container (with the Y-axis in red and the X-axis in black to serve as reference points.

On the backside of the samples, two perpendicular axes were gently drawn with a pencil, intersecting at the center of the sample. This allowed for precise alignment with the Cartesian axes on the sample holder. Carbon adhesive tape was used to lightly secure the sample on the backside, preventing unwanted movement during analysis. This method ensured the sample remained stable, maintaining the required alignment and repeatability of the analysis.

3.2.3. Storage Conditions

After the experiments, the SiC samples were carefully covered using ThorLabs Lens Cleaning Tissue to protect them from contamination and mechanical damage. These samples were then stored in Petri dish containers for added protection and subsequently placed in antistatic containers to prevent electrostatic discharge. The Gold-Nickel Intake samples were securely stored in their original sample containers, provided by Medialario s.r.l, to ensure their integrity. These containers were then placed in antistatic containers for additional safety. The storage environment was maintained at a consistent temperature of 20,°C with controlled humidity levels, ensuring minimal exposure to environmental fluctuations that could affect the materials' properties or experimental results.

3.3. Nomarski Microscopy

This section describes the application of Nomarski microscopy for high-resolution imaging of surface topography. The experimental setup, imaging protocols, and calibration techniques are detailed to illustrate how Nomarski microscopy imaging facilitates the assessment of surface features and defects critical to evaluating material quality.

3.3.1. Setup

The Nomarski microscopy analysis was conducted using an BX61 microscope equipped with a DP23M camera. The system was operated with PRECIV Pro (v2.1.1), which allowed precise control over imaging parameters and enabled high-resolution image acquisition. The setup incorporated DIC optics, including Nomarski prisms and polarizers, which were meticulously aligned and calibrated to optimize image quality and contrast.

At DLR Stuttgart, the Nomarski microscope is configured as a reflective system rather than transmissive. This setup is ideal for analyzing opaque or reflective materials, such as metallic and ceramic surfaces, where light transmission is not feasible. The reflective nature of the system significantly influences imaging results. Surface properties, such as roughness, reflectivity, and microstructural variations, strongly impact the reflected signal. High reflectivity or smooth surfaces typically yield sharper images, while rough or matte surfaces may scatter light and reduce contrast.

Moreover, reflective DIC is highly sensitive to interference patterns caused by surface imperfections or layering. While this sensitivity enhances the visualization of fine details, it necessitates careful interpretation to differentiate actual surface features from optical artifacts. It is also important to note that the colors observed in Nomarski images are not real but instead represent contrasts produced by the interaction of light with the sample's surface features. These pseudo-colors are generated by the differential interference contrast technique and serve to highlight microstructural details, rather than depict true coloration.

3.3.2. Procedures

The procedures for Nomarski microscopy analysis involved several key steps to ensure accurate and high-quality imaging, for the calibration and preparation:

- **Mounting samples**: Samples were mounted on the microscope stage using appropriate holders to secure them during imaging.
- **Calibrating the microscope**: Following the manufacturer's instructions, the microscope was calibrated to ensure optimal performance and measurement accuracy. This calibration included:
  - **Adjusting focus and alignment**: Ensuring that all optical components were properly aligned and that the focus was sharp across the entire field of view.
  - **Köhler illumination setup**: Adjusting the condenser and field diaphragms to achieve uniform illumination, which is critical for high-quality DIC imaging.
  - **Calibration of DIC components**: Fine-tuning the Nomarski prisms and polarizers to maximize contrast and minimize optical artifacts.
  - **Adjustment of z-distance**: Setting the z-distance of the microscope stage to bring the sample surface into the plane of focus, allowing interference fringes to become visible. This step is essential for accurately resolving surface topography.

For the imaging procedures, the Nomarski analysis were conducted as follows:

Calibration and preparation:

- **Mounting samples**: Samples were mounted on the microscope stage using appropriate holders to secure them during imaging.
- **Calibrating the microscope**: Following the manufacturer's instructions, the microscope was calibrated to ensure optimal performance and measurement accuracy. This calibration included:
  - **Adjusting focus and alignment**: Ensuring that all optical components were properly aligned and that the focus was sharp across the entire field of view.
  - **Köhler illumination setup**: Adjusting the condenser and field diaphragms to achieve uniform illumination, which is critical for high-quality DIC imaging.
  - **Calibration of DIC components**: Fine-tuning the Nomarski prisms and polarizers to maximize contrast and minimize optical artifacts.
  - **Adjustment of z-distance**: Setting the z-distance of the microscope stage to bring the sample surface into the plane of focus, allowing interference fringes to become visible. This step is essential for accurately resolving surface topography.

Image analysis:

- **Feature identification**: Image analysis focused on identifying and characterizing surface features that could impact the qualities of the samples, such as surface roughness, defects, and signs of oxidation.
- **Quantitative measurements**: Surface profiles obtained from WLIM scans were analyzed to quantify topographical parameters and assess the uniformity and integrity of the sample surfaces.

All procedures were meticulously documented to ensure reproducibility and accuracy in the analysis of the Nomarski microscopy data.

3.4. White Light Interferometry Microscopy

WLIM is employed to accurately characterize the surface topography of SiC samples by measuring interference patterns generated by white light. This technique provides high-resolution surface profiles, enabling detailed analysis of surface features and imperfections.

3.4.1. Setup

The WLIM analysis was conducted using a Veeco Wyko NT 9100 interferometer operated with the Vision for Profilers software, version 4.20. This instrument supports both Variable Step Interferometry (VSI) and Phase Shifting Interferometry (PSI) modes. Initially, VSI was utilized; however, due to excessive noise and less precise analysis, PSI was selected for its superior sensitivity and reduced noise levels, providing clearer interference fringes essential for analyzing the surface topography of SiC samples.

For polished SiC samples, the High Definition Variable Step Interferometry (HDVSI) mode was additionally employed to complement PSI measurements. HDVSI was specifically chosen to capture detailed features, such as holes, which PSI mode could not accurately resolve. This limitation was due to the WLIM system's difficulty in obtaining complete data from deep features, often resulting in missing data at the deepest points. The combination of PSI and HDVSI ensured comprehensive characterization of the SiC samples' surface morphology.

Key specifications and components of the WLIM setup include:

- **Interferometer model**: Veeco Wyko NT 9100
- **Software**: Vision for Profilers, Version 4.20
- **Measurement modes**: VSI, PSI, HDVSI
- **Objective lens**: 10x magnification, 50x magnification

3.4.2. Procedures

The WLIM analysis procedures encompassed calibration, measurement protocols, and data collection and processing to ensure accurate and high-quality surface characterization of SiC samples.

Calibration and Measurement Preparation:

- **Manual calibration**: For each measurement position, the z-axis was manually adjusted until the maximum of the interference patterns (called also fringes) became visible on the software interface, indicating proper alignment, as shown in Figure 3.3.
- **Luminosity adjustment**: Luminosity settings were fine-tuned to enhance the visualization of interference fringes.
- **Alignment verification**: Ensured that the sample surface was accurately positioned within the plane of focus to capture the maximum of the interference patterns.

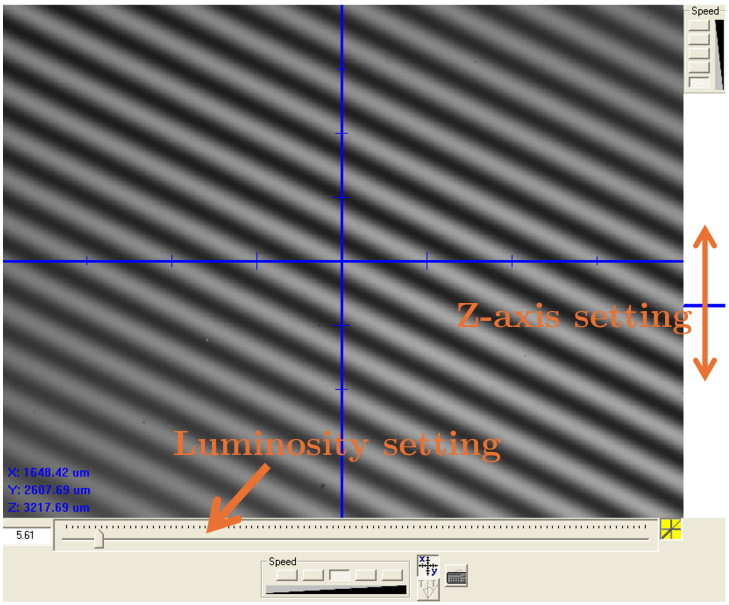

Figure 3.3.: Visualization of interference fringes during the calibration process. The z-axis adjustment is critical to achieving this optimal alignment for precise surface characterization.

Measurement Settings:

- **Measurement mode**: was selected for its high vertical resolution and sensitivity.

- **Scan length**: Configured to cover the full dynamic range of the sample's surface features, ensuring comprehensive data capture.
- **Data restoration**: After each measurement, a median data restore procedure was applied, typically correcting 10 to 35 pixels to address any missing data points due to surface discontinuities or noise.

Measurement Protocols:

- **Sample scanning**: Multiple measurements were conducted at various locations on each SiC sample to assess surface uniformity and identify localized features. At least ten locations per sample were analyzed, each covering a surface area of 640 µm × 480 µm.
- **Measurement designation**: Measurement points were designated with letters (A, B, C, ...) to systematically document and reference specific areas on the sample surfaces (see Figure 3.4).
- **Image acquisition**: Measurements were systematically performed to capture comprehensive surface profiles, ensuring that both broad overviews and detailed surface features were adequately represented.

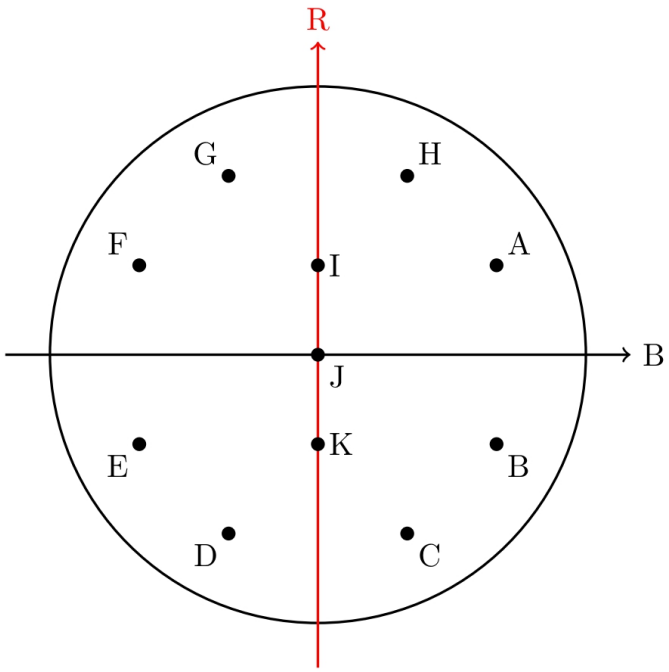

Figure 3.4.: Designation of measurement areas on the SiC sample surface for systematic WLIM imaging. The letters and axes R (red) and B (black) are references for the sample holder.

Data Collection and Processing:

- **Data acquisition**: The raw interference data obtained from the WLIM were recorded using the Vision for Profilers software.
- **Data processing**: A custom Python script developed specifically for this work was used to process the raw data. This script is provided as a separate file included with the Master Thesis.
- **Surface morphology analysis**: The processed data provided detailed information on the surface morphology of the SiC samples, serving as a baseline for comparing pre- and post-exposure conditions and evaluating the effectiveness of polishing procedures.

All procedures were meticulously followed and documented to ensure reproducibility and accuracy in the WLIM analysis of the SiC sample surfaces.

3.5. Atomic Force Microscopy

AFM is a high-resolution scanning probe technique that maps surface topography at the nanoscale by measuring the force between a sharp probe and the sample surface [57]. AFM provides three-dimensional surface profiles with nanometer resolution, making it an essential tool for characterizing surface roughness and morphology in materials science. In this work, AFM was employed to analyze the surface of the Gold-Nickel intake samples. The AFM analysis aimed to complement the data obtained from other surface techniques, providing a comprehensive understanding of the surface characteristics before and after coating.

3.5.1. Setup

3.5.1.1. Operating Principles

The AFM used in this work was a Nanosurf Easyscan 2, equipped with a silicon cantilever tip. Two primary operational modes were utilized:

- **Static (contact) mode**: The cantilever tip remains in constant contact with the sample surface, measuring deflections caused by surface features. This mode provides high-resolution imaging but can exert lateral forces on the sample, potentially causing damage to delicate surfaces.
- **Dynamic (tapping) mode**: The cantilever oscillates near its resonance frequency, intermittently contacting the sample surface. This reduces lateral forces and minimizes the risk of damaging sensitive surfaces [57].

3.5.1.2. Equipment Configuration

For the analysis of the Gold-Nickel intake samples, the AFM was operated in static mode during the initial scans. However, it was observed that this mode might have caused scratches on the soft Gold-Nickel surfaces due to the continuous contact between the tip and the sample. To mitigate this, subsequent analyses, including post-coating scans, were conducted in dynamic mode to prevent sample damage and obtain more reliable surface measurements.

3.5.2. Procedures

3.5.2.1. Sample Preparation

In the preparation of the Gold-Nickel intake samples, both pre-coating and post-coating analyses were meticulously conducted. Prior to the application of the SiO_2 coating, the samples were mounted on magnetic sample holders using a minimal amount of adhesive to ensure flatness and stability during analysis. The surfaces were then carefully cleaned with high-purity nitrogen gas to remove any loose particles and ensure a pristine surface for subsequent coating. After the SiO_2 coating was applied, the samples were prepared in a similar manner, with heightened attention to avoiding any contamination of the newly applied coating. To further mitigate the risk of scratching the SiC-coated surfaces during analysis, dynamic mode was employed, ensuring the integrity of the coated surfaces was maintained throughout the process.

3.5.2.2. Scanning Protocols

The AFM scanning protocol encompassed several critical steps to ensure precise and reliable measurements. The mode of operation was selected between Static Mode and Dynamic Mode, depending on the specific requirements of the analysis. Careful tip engagement was performed by slowly approaching the sample surface to prevent any potential damage to the tip. This process was initially conducted manually, followed by automatic control to maintain stable scanning conditions. Feedback optimization involved fine-tuning the Proportional-Integral-Derivative (PID) controller to achieve responsive feedback and ensure accurate measurements. During image acquisition, selected areas of the sample were scanned while amplitude and phase signals were continuously monitored to identify and mitigate any instabilities or artifacts that could compromise the quality of the data.

3.5.2.3. Data Collection and Processing

Data were collected using the Nanosurf Easyscan 2 software, and several processing steps were undertaken to ensure accurate and meaningful analysis. Image flattening was performed to correct for background tilt and scanner nonlinearities, employing first- or second-order flattening algorithms as needed. Noise reduction filters were applied selectively to enhance image quality without compromising the integrity of the data. Quantitative analysis involved calculating key surface roughness parameters, including arithmetic mean roughness (S_a), root mean square roughness (S_q), and maximum height (S_z). Instrument noise, such as Z-measurement noise levels, was incorporated to estimate systematic uncertainties, with a tolerance of $\pm 10\%$ for the 110 μm head, based on documented specifications. Statistical analysis further ensured the robustness of the results, as roughness metrics were calculated multiple times across various areas of each sample to assess repeatability and account for environmental and instrumental variability. These data were combined with noise values to establish error bounds for S_a, S_q, and S_z, thereby providing a comprehensive evaluation of surface characteristics.

3.5.2.4. Considerations and Limitations

Several factors significantly influenced the AFM measurements and were carefully managed to ensure data reliability. The condition of the AFM tip played a critical role, as wear or contamination could degrade image quality and measurement accuracy. To address this, regular inspections and replacements of the tips were carried out as necessary. The scanning mode also had a notable impact; the initial use of static mode on uncoated Gold-Nickel intake samples likely caused surface scratches due to the lateral forces exerted during scanning. This issue was mitigated by switching to dynamic mode for subsequent analyses, which reduced such forces and preserved surface integrity. Surface properties, including variations in chemistry and topography, posed additional challenges by affecting tip-sample interactions. The adoption of dynamic mode further alleviated these effects by minimizing direct contact between the tip and the surface. Finally, environmental conditions such as temperature and humidity fluctuations were carefully controlled, as they could otherwise introduce variability into the measurements. All scans were performed in a controlled environment to ensure consistency and accuracy in the data collected.

3.6. Scanning Electron Microscopy and Energy-Dispersive X-ray Spectroscopy

SEM combined with EDX is a powerful analytical technique for investigating surface morphology and elemental composition at the microscale [62]. Due to technical issues with the SEM equipment, analysis of the pre-coated Gold-Nickel intake samples and the pre-PWK3 tests of Samples IRS-01, IRS-03, and IRS-05 were not feasible. The SEM/EDX system underwent repairs and maintenance finished only a few weeks before the end of this project, resulting in delayed analysis capabilities.

3.6.1. Setup

The SEM/EDX analysis was conducted using a Zeiss EVO MA 10 scanning electron microscope equipped with an EDX detector. The microscope was operated using the SmartSEM software, Version 5.07 (08-Jul-14) with Service Pack 4. Key specifications of the equipment are shown in Table 3.4.

Specification	Details
Accelerating Voltage	Adjustable from 0.02 kV to 15 kV
Magnification Range	$< 7\times$ to 1,000,000$\times$
Resolution	3 nm at 15 kV (W filament)
EDX Detector	Silicon drift detector, active area varies by configuration. Capable of detecting elements from boron (B) to uranium (U)

Table 3.4.: Specifications of the Zeiss EVO MA 10 microscope [70].

Additionally, the SEM system at DLR operates under a variable pressure nitrogen atmosphere, allowing for the analysis of dielectric materials without the need for conductive coatings. This feature is advantageous for surface characterization of SiC samples, as it preserves the native surface chemistry and morphology.

Sample preparation involved the following steps:

- **Mounting**: The sample was affixed to the SEM stub using laboratory-grade double-sided conductive carbon tape to ensure good electrical grounding and minimize charging effects during electron beam exposure.
- **Alignment**: The sample was carefully positioned on the stub, aligning reference marks to maintain consistency in imaging orientation across different analyses.
- **Cleaning**: The sample was gently cleaned using high-purity compressed air to remove any loose particles or contaminants. No solvents were used to avoid introducing additional contaminants or altering the surface chemistry.

3.6.2. Procedures

The SEM imaging procedures follows these steps:

- **Electron beam energy (E_0)**: Set between 7.0 kV and 8 kV to investigate a 0.7 micrometer depth penetration (Appendix A.8).
- **Working Distance (WD)**: Adjusted between 13.5 mm and 20.5 mm to optimize detector efficiency and image resolution.
- **Imaging Mode**: Secondary Electron Imaging (SEI) was utilized, with SE1 signals employed for detailed surface topography analysis.
- **Magnification**: Ranged from 84× to 28,220× depending on the region of interest and required resolution.
- **Spot size and beam current**: Tuned to ensure sufficient beam current (e.g., 120 pA and 3 pA) while maintaining high-resolution imaging.
- **Pressure conditions**: High-vacuum conditions were maintained, with chamber pressures ranging from 9.60×10^{-5} Pa to 1.01×10^{-4} Pa to ensure optimal imaging conditions.

The EDX analysis follows these steps:

- **Spectra collection**: Spectra were recorded from various regions to capture spatial variations in elemental composition.
- **Live time**: Each spectrum was collected with a live time of 60 seconds to ensure adequate counts for accurate quantitative analysis.
- **Resolution and scale**: The analysis was performed at an accelerating voltage in the range between 7 and 8 kV, in order to understand the surface composition at 0.7 micrometers. This voltage was chosen to optimize the detection of light elements (C, O) and medium-weight elements (Ni, Si, Au) without excessive penetration depth.
- **Penetration depth**: At 7.5 kV, the electron beam penetration depth in SiC is approximately 1-2 µm, which is sufficient to analyze the surface and near-surface regions without delving too deeply into the bulk material. This ensures that the elemental analysis remains focused on the regions affected by plasma exposure.
- **Expected elements**: The analysis focused on identifying C, O, Ni, Si, and Au, corresponding to the composition of the Gold-Nickel intake samples and the SiO_2 coating.
- **Beam conditions**: The accelerating voltage was set to 7.5 kV to facilitate efficient X-ray generation for the elements of interest while limiting the penetration depth to the surface region.

3.7. Plasma Wind Tunnel PWK3

This section details the experimental testing performed in PWK3, focusing on simulating high-enthalpy enthalpy plasma environment. The operational conditions, sample alignment, diagnostic techniques, and data acquisition processes are described to ensure precise evaluation of SiC samples behavior under plasma exposure. Temperature correction and analysis methodologies are also introduced.

3.7.1. Setup

3.7.1.1. Operating Conditions and Parameters

The PWK3 facility utilizes the Inductively Heated Plasma Generator 3 (IPG3) model to generate high-temperature plasmas without electrode contamination [43, 42]. In this work, pure oxygen plasma was generated using the IPG3 generator to examine the formation of SiO_2 under high-enthalpy plasma conditions. To ensure the reliability and comparability of the results, consistent operating conditions and parameters were maintained across all tests. The key parameters utilized during both the calibration tests and the SiC sample evaluations are summarized in Table 3.5.

The measured values for the heat flux at the test position during the heat flux tests were 538 kW/m^2, while the pitot pressure at the test position during the pitot pressure tests was 143.2 Pa.

Table 3.5.: Operating conditions and parameters of PWK3 during oxygen plasma testing

Parameter	**Heat Flux Test**	**Pitot Pressure Test**
Plasma generator	IPG3	IPG3
Working gas	Pure Oxygen (O_2)	Pure Oxygen (O_2)
Mass flow rate (g/s)	3.214	3.211
Anode voltage (V)	5,865	5,851
Anode power (kW)	109.98	110.4
Chamber pressure (Pa)	52.6	52.5
x-position (mm)	228	228

A schematic defining the x-position within the PWK3 facility is shown in Figure 3.5. The x-position of 228 mm from the quartz tube end of the IPG3 was used for all tests.

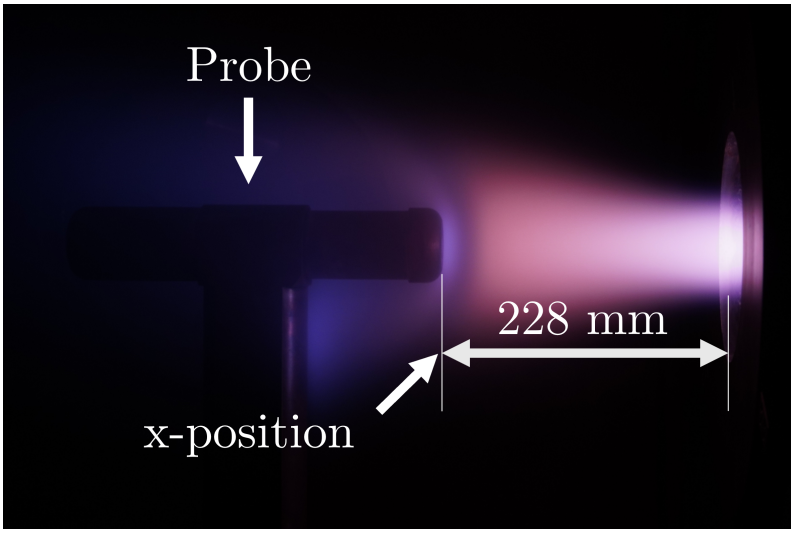

Figure 3.5.: Illustration of the x-position reference in the PWK3 facility, corresponding to the setup used for the IRS-01 sample testing.

3.7.1.2. Exposure Time Settings

Based on previous analyses of SiC samples from previous studies, exposure times were selected to investigate the oxidation behavior of SiC under different durations while maintaining consistent plasma conditions.

Three of the six polished SiC samples, designated IRS-01, IRS-03, and IRS-05, were exposed to pure oxygen plasma in PWK3 with varying exposure times. Specifically, the sample IRS-01 was exposed for 120 seconds, IRS-03 for 300 seconds, and IRS-05 for 600 seconds.

The exposure time for IRS-01 was chosen based on the time required for the sample to reach a near-steady-state temperature, as determined in previous studies [13]. Longer exposure times for IRS-03 and IRS-05 were selected to investigate the progressive effects of oxidation over extended periods.

3.7.1.3. Sample Mounting and Alignment in PWK3

Samples were mounted on the test probe designed for PWK3 experiments. The mounting procedure involved:

- **Sample installation**: The SiC sample was securely attached to the probe using high-temperature-resistant mechanical fixtures to prevent movement during testing.
- **Alignment**: The alignment of the sample, probe, and IPG3 generator was ensured using a multi-directional laser alignment system. A ruler was used to position the sample precisely at 228 mm from the IPG3 exit.
- **Verification**: Alignment was verified through visual inspection and confirmed using positioning sensors to ensure the sample surface was perpendicular to the plasma flow.

Throughout the handling process, cleanroom gloves were used to prevent contamination or damage to the sample surfaces. The samples were only touched when necessary during positioning and fitting, minimizing contact with the critical surfaces.

3.7.1.4. Diagnostic Techniques Utilized

To ensure precise monitoring, calibration, and documentation during testing, a combination of advanced diagnostic tools and techniques was employed. Temperature monitoring was conducted using the LP3 linear pyrometer, providing real-time thermal behavior data for the test samples. The surface temperature of the samples, corrected for the pyrometer's assumptions, was calculated using the following equation:

$$T_w = \frac{1}{\frac{1}{T_m} + \frac{\lambda k}{hc} \ln(\epsilon \cdot \tau)} \tag{3.1}$$

In this equation, T_m represents the measured temperature in Kelvin obtained from the LP3 pyrometer data, while the constants are defined as follows: $\lambda = 960\,\text{nm}$ is the wavelength of interest, $h = 6.62607015 \times 10^{-34}\,\text{J·s}$ is Planck's constant, $k = 1.380649 \times 10^{-23}\,\text{J/K}$ is Boltzmann's constant, and $c = 3.00 \times 10^{8}\,\text{m/s}$ is the speed of light. The factor $\tau = 0.93$ accounts for the transmissivity of the quartz window used during the experiment.

The pyrometer's default assumption of $\epsilon = 1$ for emissivity was corrected using $\epsilon = 0.52$, a value determined through multiwavelength-pyrometry measurements [13]. This correction ensures that the derived T_w values reflects better the thermal behavior of the polished SiC samples. Both T_m and T_w as functions of time were calculated using a custom Python script, which is included as a supplementary file in this master thesis.

Visual documentation of the experiments was performed using a Sony A6400 camera to capture detailed video and image records of the tests. To mitigate the effects of intense light from the plasma, a series of neutral density filters from the Hoya PROND series were utilized. For calibration tests, an ND100 filter (6 2/3 stops) was applied to reduce excessive light interference, ensuring accurate data capture. During actual testing of the polished SiC samples, an ND8 filter (3 stops) was employed to optimize image clarity under controlled lighting conditions. This combination of diagnostic techniques provided robust and reliable data for subsequent analysis.

3.7.2. Procedures

The pre-test preparation involved conducting two preliminary evaluations without samples to establish baseline Pitot pressure and heat flux values for subsequent tests. These assessments, lasting 5 and 1 minute respectively, were conducted using only the test probe. SiC samples were handled with care to

prevent contamination, stored in cleanroom-grade packaging, and cleaned prior to testing with high-purity compressed air (OKS 2731) [71] to remove dust particles. Future studies may consider using even higher-purity alternatives, such as Thorlabs CA6EU [72], although environmental impact considerations due to CFC content should be addressed. During the tests, the PWK3 chamber was first securely sealed and evacuated to approximately 52 Pa. SiC samples were positioned away from the plasma stream to avoid premature exposure during plasma ignition. The oxygen plasma was generated using the IPG3 system, and samples were precisely aligned with the plasma stream upon ignition. Exposure timing was rigorously controlled, with sample temperatures monitored via the LP3 linear pyrometer. The test was video-documented with a Sony A6400 camera equipped with neutral density filters optimized for high-temperature conditions. Upon completing the designated exposure time, the plasma generator was shut down following standard safety protocols. Post-test procedures included a cooldown period of approximately 20 minutes within the chamber to mitigate thermal shock risks before sample retrieval. The cooled samples were carefully removed using cleanroom gloves, repackaged in cleanroom-grade materials, and stored in sealed plastic bags to preserve surface integrity for subsequent analysis. All systems were systematically shut down, and atmospheric pressure was restored to the chamber to complete the testing cycle.

During and after the tests, temperature data were collected using the LP3 linear pyrometer. Video recordings were reviewed to observe any visual changes or anomalies during the exposure. All collected data were securely archived for further analysis and integration into the study. All samples were handled with care to preserve their surfaces for subsequent analysis. Cleanroom gloves were worn at all times during sample handling to prevent contamination. Contact with the samples was minimized, and critical surfaces were avoided during mounting to ensure their integrity. After testing, samples were packaged using cleanroom-grade paper specifically designed for low surface roughness materials, preventing scratching or contamination.

3.8. Test Matrix

A test matrix of the tests conducted on the polished SiC Samples is provided in Table 3.6.

Table 3.6.: Test matrix form PWK3 tests of polished SiC samples

Parameter	**IRS-01**	**IRS-03**	**IRS-05**
Sample Information			
Sample ID	IRS-01	IRS-03	IRS-05
Material	StarCeram S SiC	StarCeram S SiC	StarCeram S SiC
Surface Roughness Before Polishing (S_a)	889 nm	970 nm	720 nm
Surface Roughness After Polishing (S_a)	16.87 ± 1.79 nm	16.05 ± 1.13 nm	15.29 ± 0.91 nm
Potential Surface Tilt	Up to 1–2°	Up to 1–2°	Up to 1–2°
Plasma Wind Tunnel Test Parameters			
Test ID	219	220	221
Exposure Time (s)	120	300	600
Purpose of Exposure Time	SiO_2 layer formation	SiO_2 layer formation	SiO_2 layer formation
Plasma Generator	IPG3	IPG3	IPG3
Working Gas	Pure Oxygen (O_2)	Pure Oxygen (O_2)	Pure Oxygen (O_2)
Anode Voltage U_{Anode} (V)	5861.43 ± 16.90	5849.87 ± 18.11	5855.04 ± 15.42
Anode Current I_{Anode} (A)	18.85 ± 0.10	18.85 ± 0.12	18.75 ± 0.10
Electrical Power P_{el} (kW)	110.48 ± 0.60	110.28 ± 0.76	109.76 ± 0.64
Chamber Pressure (Pa)	52.6	51.0	54.0
Tank Pressure p_{Tank} (hPa)	0.54 ± 0.03	0.51 ± 0.03	0.54 ± 0.03
Oxygen Mass Flow Rate m_{O_2} (mg/s)	3214.92 ± 1.32	3217.63 ± 1.36	3215.46 ± 2.57
x-Position from IPG3 Exit (mm)	228	228	228
Heat Flux at Test Position (kW/m^2)	538	538	538
Pitot Pressure at Test Position (Pa)	143.2	143.2	143.2
Diagnostic Techniques and Data Collection during PWK3 Tests			
Temperature Monitoring	LP3 Pyrometer	LP3 Pyrometer	LP3 Pyrometer
Emissivity Correction ϵ	0.52	0.52	0.52
Transmissivity τ	0.93	0.93	0.93
Visual Documentation	Sony A6400 Camera	Sony A6400 Camera	Sony A6400 Camera
Neutral Density Filter Used	ND8 (3 stops)	ND8 (3 stops)	ND8 (3 stops)
Data Analysis Scripts	Custom Python Script	Custom Python Script	Custom Python Script

A test matrix of the tests conducted on the Gold-Nickel intake samples is provided in Table 3.7.

Table 3.7.: Test matrix for PECVD coating of gold-nickel intake samples

Parameter	**Sample 368-12**	**Sample 807-6**
	Sample Information	
Sample ID	368-12	807-6
Material Composition	Gold-Nickel Alloy	Gold-Nickel Alloy
Fabrication Technology	Repli-formed Optics™	Repli-formed Optics™
Initial Surface Roughness (S_a)	0.235 ± 0.100 nm	0.199 ± 0.045 nm
Surface Roughness After Coating (S_a)	4.320 ± 3.398 nm	3.660 ± 0.828 nm
Mandrel Used	Specific mandrel for 368-12	Specific mandrel for 807-6
	PECVD Coating Parameters	
PECVD Environment	Non-cleanroom	Non-cleanroom
Coating Facility	IKV, RWTH Aachen	IKV, RWTH Aachen
Precursor Gas	HMDSO (4 sccm)	HMDSO (4 sccm)
Oxygen Flow	472 sccm	472 sccm
Microwave Power	3500 W	3500 W
Microwave Pulsing	On-Time: 4 ms, Off-Time: 100 ms	On-Time: 4 ms, Off-Time: 100 ms
Chamber Pressure	5 Pa	5 Pa
Deposition Time	400 s	400 s
Coating Thickness	≈40 nm	≈40 nm

4. Results and Discussion

This chapter presents a comprehensive analysis of the experimental results obtained from the characterization of Silicon Carbide (SiC) samples and the evaluation of PECVD SiO_2 coatings on Gold-Nickel substrates. The findings are organized into two main sections: the first focuses on the oxidation behavior and surface morphology of SiC samples, while the second examines the deposition and characterization of SiO_2 coatings on metallic substrates. Each section systematically discusses the methodologies, observations, and implications of the results, providing insights into the feasibility and challenges associated with developing protective and reflective coatings for Advanced Biomimetic Electrospray Propulsion (ABEP) intake systems in Very Low Earth Orbit (VLEO) environments.

4.1. Silicon Carbide Results and Discussion

This section investigates the oxidation behavior, surface morphology evolution, and elemental composition changes of SiC samples exposed to high-enthalpy oxygen plasma under conditions relevant to future ABEP intakes in VLEO. The analyses employ Nomarski microscopy and SEM/EDX microscopy for surface characterization, and WLIM microscopy for roughness measurements. The central question driving this investigation is whether a SiO_2 layer can form on initially low-roughness SiC surfaces to achieve specular reflectivity and enhance the efficiency of an ABEP intake. By comparing oxidation responses at different exposure times and examining previously tested samples, this section evaluates the feasibility and challenges of developing a stable, uniform, and specularly reflective SiO_2 surface optimized for future ABEP systems.

4.1.1. Characterization of SiC Samples from Previous Studies

To anticipate the behavior of the new polished SiC samples, four previously unexamined SiC samples (Samples Kaiser-1, Kaiser-2, Massuti-1, and Kaiser-3) from earlier studies [12, 13] were analyzed. The naming convention for these samples reflects the surnames of the researchers who exposed them to the PWK3 facility at IRS Stuttgart in past experiments. These samples had been exposed to high-enthalpy oxygen plasma in the PWK3 facility but lacked detailed surface examinations. This preliminary analysis provides insights into oxidation behavior and surface morphology changes induced by plasma exposure, setting expectations for the new polished samples.

4.1.1.1. Sample Kaiser-1

After three exposure tests in the PWK3 facility, Sample Kaiser-1 (Figure 4.1) exhibited a dark black-grey surface with prominent irregularities, especially towards the center. These features suggest significant plasma-induced surface roughness and potential damage due to thermal stresses.

Surface Roughness

WLIM measurements of the whole sample (Section 3.4.2) in PSI mode at 10x magnification provided quantitative surface roughness parameters. The S_a of the whole sample was $1.214\,\mu$m with a standard deviation of $1.565\,\mu$m. The S_q was $4.374\,\mu$m, and the R_z reached a mean value of $63.457\,\mu$m. These high roughness values reflect the severe surface damage due to prolonged plasma exposure under the test conditions described in Section 3.1.1.

Surface Morphology

Nomarski microscopy at 50x magnification (Figure 4.2) revealed distinct and complex surface features. Pronounced cracks and localized erosion were evident, likely resulting from thermal stresses and aggressive plasma-material interactions. The surface displayed iridescent patches, probably indicative of a thin SiO_2 layer forming unevenly across the sample, suggesting variations in oxide thickness. Additionally, regions of heightened surface roughness and pitting were observed, which could be attributed to partial sintering or

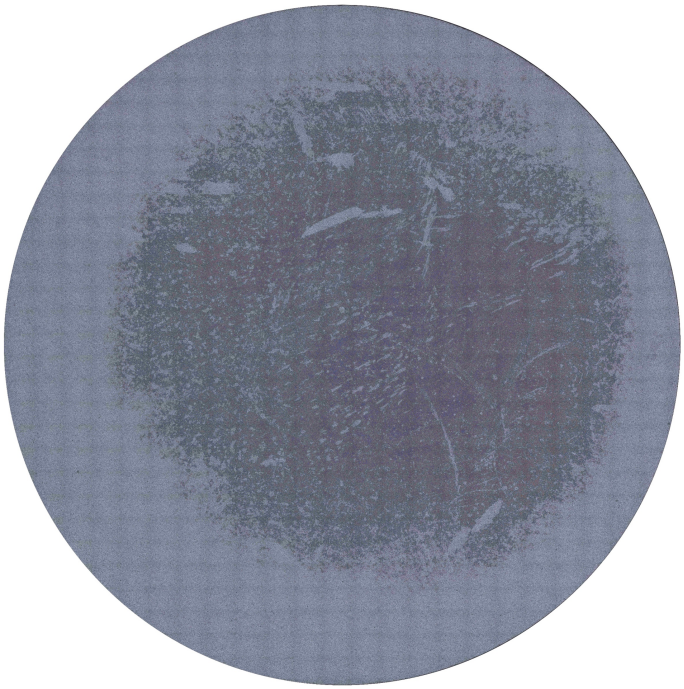

Figure 4.1.: Stitched Nomarski microscopy image of Sample Kaiser-1 after exposure tests, showing surface irregularities.

selective material removal during plasma exposure. These morphological changes highlight the significant impact of the high-enthalpy plasma environment on the SiC surface.

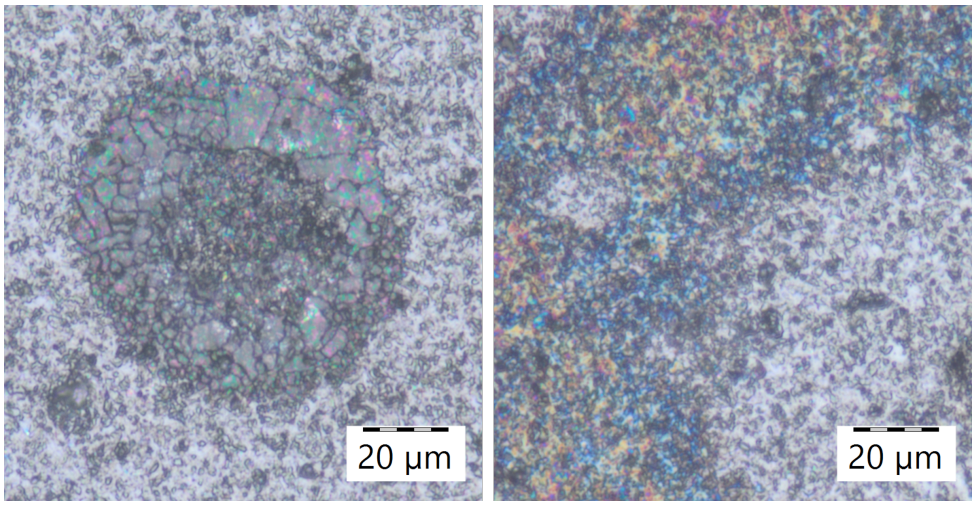

Figure 4.2.: Nomarski microscopy images of sample Kaiser-1 at 50x magnification showing (left) crack formation and (right) non-uniform oxide layer formation.

4.1.1.2. Sample Kaiser-2

Sample Kaiser-2 presented a smoother dark gray surface without visible irregularities, suggesting a uniform oxidation layer (Figure 4.3).

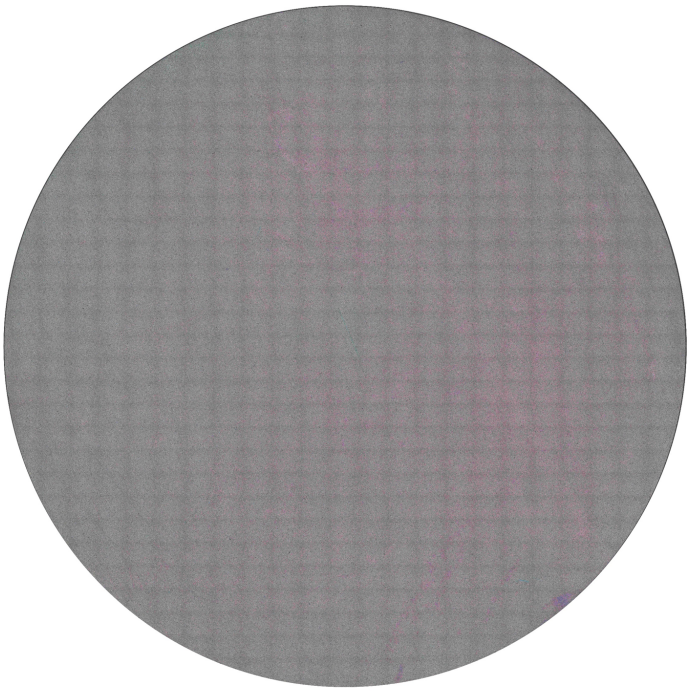

Figure 4.3.: Stitched Nomarski microscopy image of sample Kaiser-2 after exposure tests.

Surface Roughness

WLIM measurements of the whole sample (Section 3.4.2) indicated an S_a of 118.36 nm with a standard deviation of 12.93 nm. The S_q was 149.77 nm, and R_z was 1319.22 nm. These values demonstrate a notably smooth surface, aligning with visual assessments that highlighted a uniform oxide layer and minimal defect presence. The consistently low S_a, S_q, and R_z values can be directly attributed to the controlled plasma exposure conditions detailed in Section 3.1.1, which facilitated the formation of a homogeneous SiO_2 layer while minimizing surface disruptions.

Surface Morphology

Nomarski microscopy at 50x magnification (Figure 4.4) revealed significant surface characteristics. The surface showed increased iridescence, suggesting the formation of a more uniform SiO_2 layer across the sample, which may indicate enhanced oxidation. Localized defects, including larger craters up to 400 nm in size, were observed and are potentially linked to the material's inherent porosity, suggesting incomplete or uneven oxide layer formation in these regions. Additionally, the surface exhibited variable roughness, with smoother areas interspersed among rougher patches. Notably, in the right image of Figure 4.4, a clear blue hue in the central area may indicate the presence of a multi-layered oxide structure, reflecting complex material interactions under plasma exposure.

4.1.1.3. Sample Massuti-1

Sample Massuti-1 exhibited a fully oxidized surface with minimal visible damage, indicating strong resistance to plasma conditions (Figure 4.5).

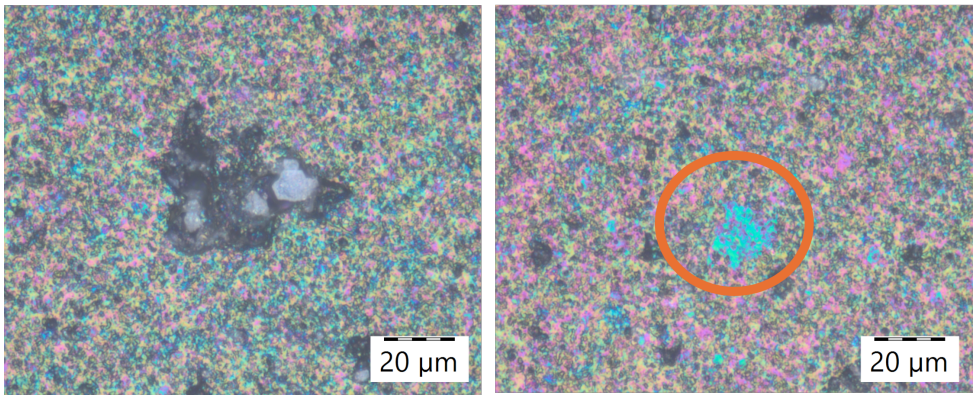

Figure 4.4.: Nomarski microscopy images of sample Kaiser-2 at 50x magnification showing a porous area (left) and a potential multi-layer oxide formation indicated by the central blue region (right).

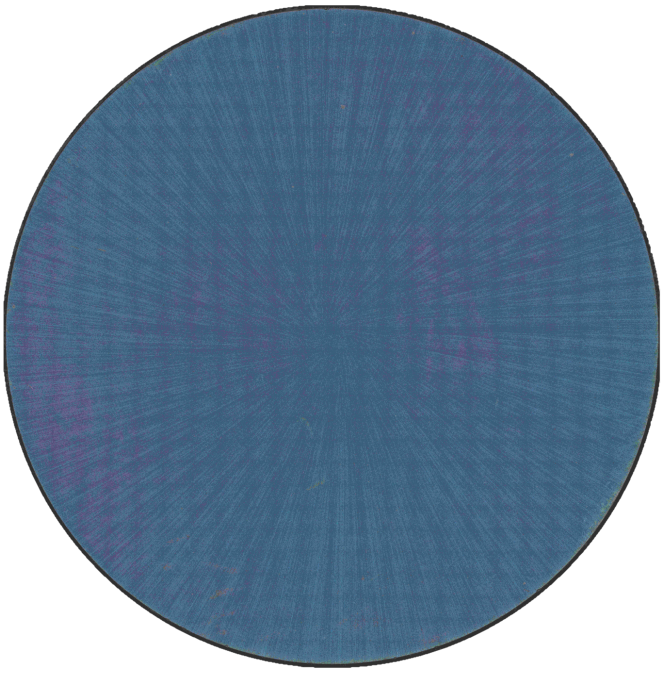

Figure 4.5.: Stitched Nomarski microscopy image of sample Massuti-1 after exposure test.

Surface Roughness

WLIM measurements across the entire sample (Section 3.4.2) revealed an S_a of 101.89 nm with a standard deviation of 2.97 nm, an S_q of 125.13 nm, and an R_z of 1063.54 nm. These results indicate a remarkably smooth surface, strongly suggesting the formation of a uniform and well-distributed SiO_2 layer. This sample stands out as the only one subjected to plasma exposure a single time, a key factor contributing to its consistently low S_a, S_q, and R_z values. The controlled plasma exposure conditions detailed in Section 3.1.1 played a crucial role in facilitating the formation of a homogeneous SiO_2 layer while effectively minimizing surface irregularities and defects. The single exposure appears to have been sufficient to achieve the desired surface characteristics without introducing relevant disruptions.

Surface Morphology

Nomarski microscopy at 50x magnification (Figure 4.6) revealed a surface characterized by a uniform oxide layer and minimal defects. The consistent iridescence observed across the sample indicated the formation of a homogeneous and protective SiO_2 layer, with subtle variations in coloration suggesting the possibility of multiple oxide layers. Defects were infrequent and minor, likely attributable to the inherent porosity of the material rather than damage induced by plasma exposure. The area highlighted

in Figure 4.6 (right) appears to exhibit localized thickening of the oxide layer, potentially resulting from contaminant interaction or the accumulation of SiO_2. This suggests the development of a multi-layer structure in some regions. Conversely, the defect shown in Figure 4.6 (left) reflects partial oxidation. The smoother edges and comparable coloration to the surrounding surface imply that the defect is a natural consequence of the material's porous microstructure.

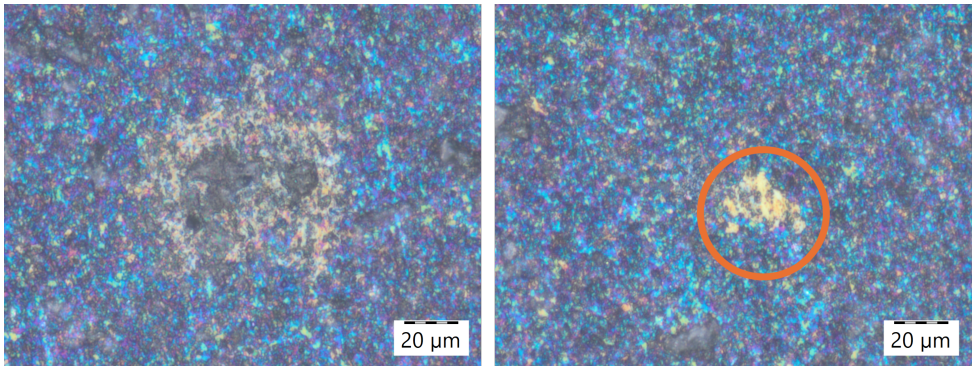

Figure 4.6.: Nomarski microscopy image of sample Massuti-1 at 50x magnification showing a surface defect due to the porous structure of the material (left) and a possible multi-layer formation (right).

4.1.1.4. Sample Kaiser-3

Following two exposure tests, the second of which was conducted at a notably high mass flow rate of 4.82 g/s, double that used for the other samples (Section 3.1.1), Sample Kaiser-3 exhibited pronounced discoloration and visible surface defects (Figure 4.7).

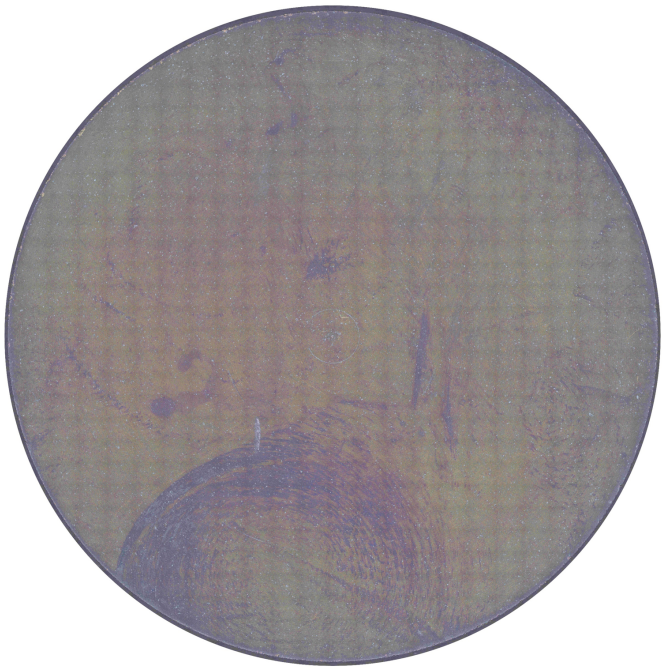

Figure 4.7.: Stitched Nomarski microscopy image of sample Kaiser-3 after exposure tests.

Surface Roughness

WLIM measurements of the whole sample (Section 3.4.2) showed an S_a of 6681.88 nm with a standard deviation of 659.24 nm. The S_q was 8969.55 nm, and R_z reached 143.90 μm in the most rough areas. These elevated roughness values reflect the severe surface degradation, likely due to the higher mass flow rates of oxygen during testing, which intensified the plasma-material interactions.

Surface Morphology

Nomarski microscopy at 50x magnification (Figure 4.8) revealed significant surface alterations indicative of intense plasma-material interactions. The surface displayed erosion, characterized by craters, pits, and roughened areas, suggesting aggressive material removal under testing conditions. Additionally, possible white deposits were observed across the surface, which are likely remnants of material redeposition, possibly resulting from reorganization of SiO_2 during plasma exposure. These features underscore the severe impact of high-enthalpy plasma on the sample's surface integrity.

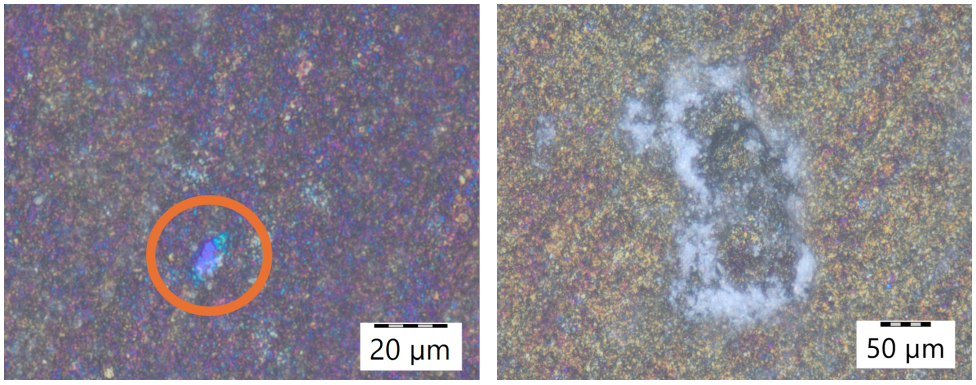

Figure 4.8.: Nomarski microscopy images of sample Kaiser-3 at 50x magnification showing a likely erosion area (left) and possible white material deposits (right).

4.1.1.5. Insights from Previous Studies

The comparative analysis of the SiC samples previously tested in the PWK3 facility, namely Kaiser-1, Kaiser-2, Massuti-1, and Kaiser-3, reveals how different exposure conditions influence the formation of oxide layers and the resultant surface morphology. Kaiser-1 underwent prolonged and repeated exposure under moderate conditions and emerged with pronounced roughness, severe crack formation, and non-uniform oxide growth. In contrast, Kaiser-2 displayed more uniform oxidation behavior, forming a smoother and more homogeneous SiO_2 layer, although still exhibiting some localized defects and slight variations in thickness. Massuti-1, with only a single controlled exposure, retained a remarkably smooth surface and a well-distributed oxide layer, characterized by minimal defects and a stable underlying morphology that suggests the controlled growth of a protective SiO_2 film. Kaiser-3, exposed to a notably higher mass flow rate and subjected to more aggressive plasma conditions, manifested massive roughening, widespread erosion features, and possible redeposited matter indicative of vigorous material sputtering and volatile species formation.

The nature of these results confirms that the overall quality and protective characteristics of the oxide layer strongly depend on exposure parameters such as temperature, plasma composition, mass flow rate, and exposure duration. Samples that formed relatively uniform and stable SiO_2 layers, like Kaiser-2 and Massuti-1, reflect conditions that favored passive oxidation and stable oxide growth. Conversely, samples like Kaiser-1 and especially Kaiser-3 demonstrate that harsher conditions can push the material toward more active oxidation regimes, ultimately leading to roughness escalation and structurally compromised surfaces. The observed differences in oxide homogeneity, surface roughness parameters, and defect distribution provide valuable insights into the role of operational conditions on SiC oxidation and the subsequent formation of protective layers relevant to ABEP intake applications in VLEO environments.

Table 4.1.: Summary of Surface Roughness, Oxide Layer Uniformity, and Exposure Parameters for SiC Samples from Previous Studies

Sample	No. Tests	Exposure Time	max O_2 Mass Flow	max T_m achieved	S_a	Oxide Layer Uniformity
Kaiser-1	3	46 min	3.12 g/s	1350 K	1.214 ± 0.495 µm	Non-uniform, irregular thickness
Kaiser-2	3	23.5 min	3.12 g/s	1380 K	0.118 ± 0.004 µm	Relatively uniform, minor defects
Massuti-1	1	20 min	3.12 g/s	1400 K	0.102 ± 0.001 µm	Highly uniform, minimal defects
Kaiser-3	2	18.87 min	4.82 g/s	1350 K	6.682 ± 0.199 µm	Severely disrupted, non-uniform

4.1.2. Characterization of Polished SiC Samples

Following the analysis of the SiC samples from previous studies (Section 4.1.1), which provided valuable insights into the oxidation behavior and surface morphology changes induced by plasma exposure, the attention is turned to the characterization of the newly procured SiC samples. These samples, designated as IRS-01 to IRS-06, were subjected to enhanced polishing procedures to achieve significantly lower surface roughness, aiming to improve their quality for their successive applications.

4.1.2.1. Surface Preparation and Polishing Results

The new SiC samples were provided by Kyocera Fineceramics with an initial surface roughness (S_a) in the range of 681–992 nm. To verify if a lower roughness level could influence positively the formation of SiO_2 that could possibly be specularly reflective, the samples were subjected to an additional polishing process at the IMTCCC Institute of University of Stuttgart. The polishing aimed to reduce the surface roughness to tens of nanometers.

The effectiveness of the polishing process was evaluated by comparing the surface roughness before and after polishing. Table 4.2 summarizes the results.

Table 4.2.: Surface roughness (S_a) of SiC samples before and after polishing

Sample	**Before Polishing** (S_a)	**After Polishing** (S_a)	**Improvement (%)**
IRS-01	889 nm	16.87 ± 1.79 nm	98.1
IRS-02	992 nm	15.63 ± 1.64 nm	98.4
IRS-03	970 nm	16.05 ± 1.13 nm	98.3
IRS-04	723 nm	16.17 ± 1.50 nm	97.8
IRS-05	720 nm	15.29 ± 0.91 nm	97.9
IRS-06	681 nm	16.19 ± 1.20 nm	97.6

The results indicate a significant reduction in surface roughness across all samples, achieving an improvement of over 97% in S_a. This substantial decrease is anticipated to enhance the uniformity of oxidation, thereby facilitating the formation of the SiO_2 layer.

4.1.2.2. Visual Inspection After Polishing

Before polishing, the SiC samples exhibited a uniform dark appearance with visible inclusions characteristic of sintered SiC. The critical surfaces showed uneven texture, and the lack of reflectivity suggested high surface roughness. After polishing, the critical surfaces transitioned to a glossy, deep black finish with mirror-like reflectivity. The polished surfaces reflected light uniformly, indicating significant improvement in smoothness and elimination of micro-texture. The color remained consistent (black) but with enhanced visual clarity and a metallic-like sheen due to the improved surface quality.

4.1.2.3. Baseline Analysis of Unexposed Samples

To establish a robust baseline for comparison with the plasma-exposed samples, three of the six polished SiC samples (IRS-02, IRS-04, and IRS-06) were designated as unexposed references. All six samples were initially characterized by WLIM and Nomarski microscopy. These analyses consistently confirmed that the samples shared a similar starting morphology, featuring low roughness and a uniform texture resulting from the extensive polishing process. The observed similarities among all six samples ensured that any subsequent changes in surface characteristics could be attributed to the plasma exposure rather than initial variability.

Although all unexposed samples (IRS-02, IRS-04, and IRS-06) exhibited the same initial surface features, practical constraints influenced the choice of which sample would undergo more detailed elemental and microstructural analysis by SEM/EDX. Due to the late availability of the SEM/EDX facility following instrument maintenance, only one unexposed sample could be comprehensively examined within the remaining timeframe of this work. Sample IRS-02 was selected for this purpose because it presented a

higher density of potentially contaminated areas, likely introduced during polishing or sample preparation, which made it particularly interesting for compositional analysis. By focusing on IRS-02, it was possible to obtain a representative baseline for elemental composition and surface microstructure before plasma interaction.

4.1.2.4. SEM/EDX Surface and Elemental Analysis of the Unexposed IRS-02 Sample

SEM observations of the IRS-02 sample revealed a homogeneous surface matrix punctuated by small crater-like features due to the porosity of the material (Figure 4.9). These craters, typically 1–10 µm in diameter, displayed well-defined boundaries and circular to semi-circular geometries. The overall uniformity in gray-scale contrast across the sample suggested compositional homogeneity, while the presence of craters and pores indicated areas of localized structural variation inherent to the sintered SiC substrate.

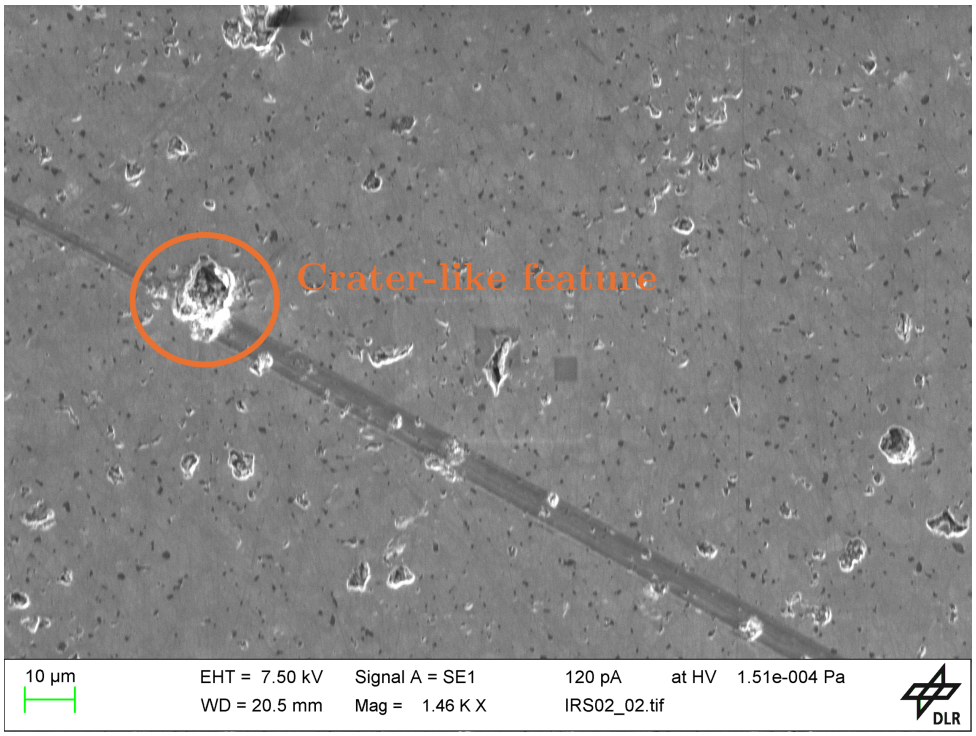

Figure 4.9.: SEM image of the IRS-02 sample at 1.46K× magnification, showing a crater-like feature due to the porosity of the material.

4.1.2.5. Elemental Composition of the Unexposed IRS-02 Sample

Figure 4.10 illustrates the EDX spectra obtained from two distinct regions of the unexposed IRS-02 sample: a defect-free surface (left) and a large crater-like structure (right). These analyses confirm that Si and C are the primary constituents of the sintered SiC material, consistent with its stoichiometric composition. Minor oxygen (O) signals detected across the surface suggest slight surface oxidation prior to exposure, while trace aluminum (Al) peaks, visible in the crater-like region, point to the possible introduction of contaminants during polishing or machining, such as from aluminum oxide abrasives or contact with aluminum tools.

In the defect-free regions (Figure 4.10, left), silicon counts ranged from approximately $0.700 - 0.750\,\mathrm{cps/eV}$, while carbon counts were around $0.400\,\mathrm{cps/eV}$. These values suggest a relatively uniform elemental distribution typical of well-prepared SiC surfaces. By contrast, inside the crater-like structures (Figure 4.10, right), carbon signals increased significantly to $0.800\,\mathrm{cps/eV}$, while silicon signals decreased to $0.100\,\mathrm{cps/eV}$.

The elevated carbon levels within the crater-like structures of the IRS-02 sample are most likely due to a combination of residual polishing contaminants and the inherent ability of surface defects to trap and retain carbonaceous materials. To mitigate such issues in future sample preparations, enhancing cleaning protocols, and employing contamination-free polishing techniques could be beneficial.

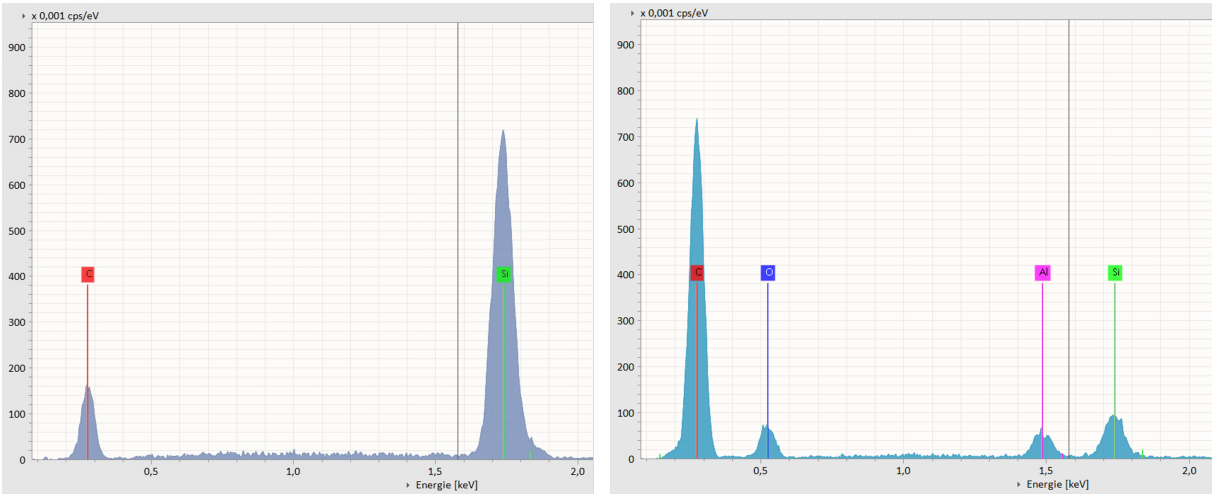

Figure 4.10.: EDX spectra of the unexposed IRS-02 sample: (left) defect-free surface, showing consistent Si and C signals, and (right) crater-like region, showing elevated C and trace Al signals.

4.1.3. Results for IRS-01 (120 s Exposure)

Sample IRS-01 was exposed to oxygen plasma for 2 minutes in the PWK3 facility. The plasma parameters achieved during the test are provided in the Test Matrix in Section 3.8 (Test ID: 219). The sample temperature was recorded using the LP3 linear pyrometer. As shown in Figure 4.11, the maximum measured temperature T_m was 1276.50 K at 120.79 s, corresponding to a corrected maximum temperature T_w of 1360.63 K. The sample did not reach a steady-state temperature before the end of the test.

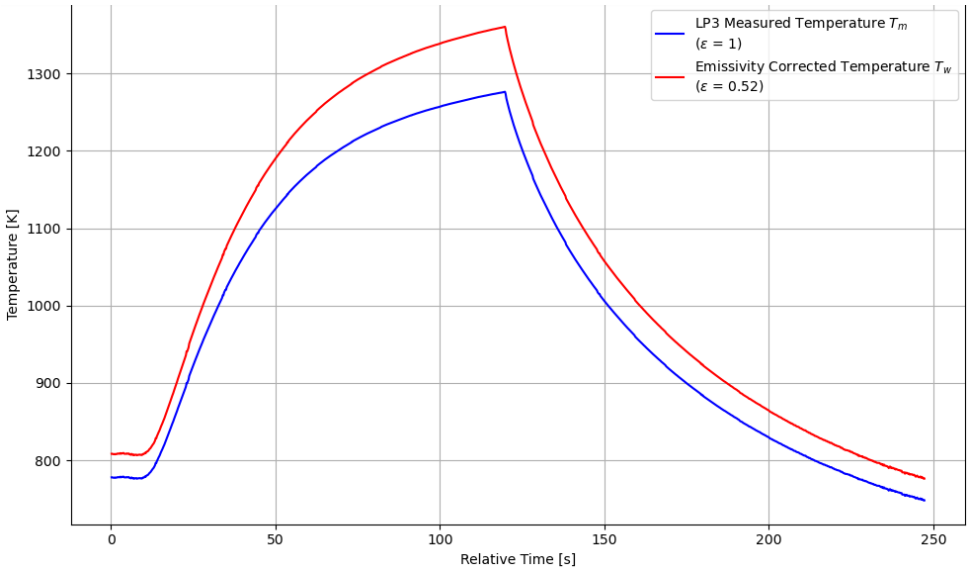

Figure 4.11.: Temperature-time profile of sample IRS-01 during the PWK3 test and subsequent cooling period.

4.1.3.1. Surface Roughness Measurements with WLIM

Table 4.3 presents the surface roughness parameters of IRS-01 before and after exposure to PWK3 plasma flow for 120 s.

The S_a and S_q both show modest increases after exposure, but the S_z increases dramatically, indicating the development of significant topographical features. This pronounced rise in S_z suggests that the initial oxidation process and the formation of a SiO_2 layer are not uniformly distributed across the surface. Instead, localized protrusions or surface irregularities may have formed, potentially due to partial oxidation

Table 4.3.: Surface roughness parameters for sample IRS-01 before and after plasma exposure

Parameter	Pre-Exposure	Post-Exposure
Arithmetic Mean Roughness (S_a), nm	16.87 ± 1.79	19.28 ± 1.38
Root Mean Square Roughness (S_q), nm	25.26 ± 3.78	51.36 ± 7.56
Maximum Height of the Surface (S_z), nm	320.58 ± 54.26	4233.32 ± 678.70

or redeposition processes rather than a smooth, protective oxide film. The short exposure time may have been insufficient to establish a stable and uniform SiO_2 layer, resulting in a less controlled and more irregular morphology.

4.1.3.2. Visual Results After the Test

After exposure to oxygen plasma for 2 minutes, sample IRS-01 exhibited significant visual changes. During the test, the critical surface (exposed to the plasma) became gold/red and remained in this state for several minutes due to the high temperature achieved. Post-test, the critical surface showed a noticeable reduction in reflectivity and transitioned to a matte black visual appearance, contrasting with the high gloss observed in the pre-test polished condition. Surface discoloration and a darker tone suggest possible oxidation or material interaction with the oxygen plasma. No visible mechanical damage was observed, indicating that the structural integrity of the sample was maintained during the 2-minute exposure.

4.1.3.3. Surface Analysis with Nomarski Microscopy

Before the PWK3 test (Figure 4.12, left), sample IRS-01 exhibited a light blue coloration with minimal surface irregularities, characterized by a uniform texture and minimal optical contrast. In contrast, after 2 minutes of oxygen plasma exposure (Figure 4.12, right), the surface transformed to a brownish tint with visible surface irregularities, probably indicating the beginning of the passive oxidation regime.

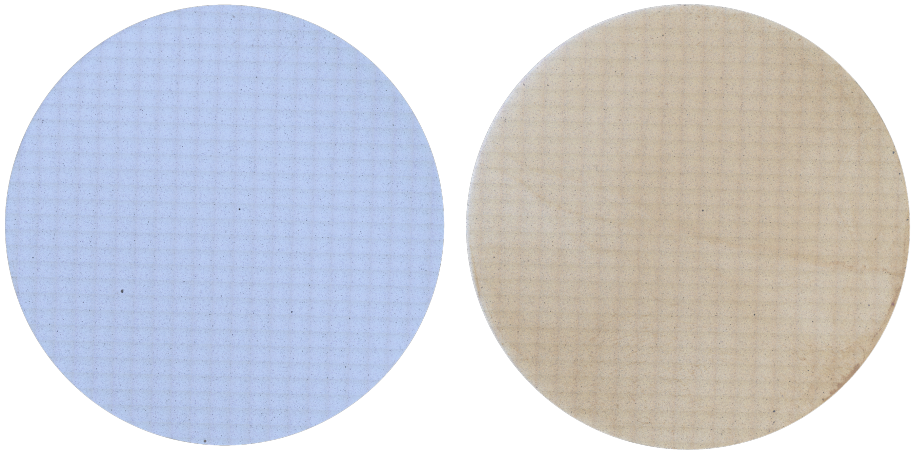

Figure 4.12.: Stitched Nomarski microscopy images of sample IRS-01 at 10x magnification: before (left) and after (right) PWK3 test.

At higher magnification (Figure 4.13, left), the pre-exposure surface displays distributed dark regions representing material porosity, with pore sizes ranging from approximately 1–10 µm and a density of 15–20 pores per 100 µm^2. After plasma exposure (Figure 4.13, right) exhibits distinct optical interference patterns (crystalline structures) and local discolorations.

Such coloration occurs when light encounters a thin oxide film, causing constructive and destructive interference of reflected light at different wavelengths. The fact that the surface can produce these interference colors demonstrates that a reasonably uniform and transparent oxide has formed. This suggests that oxidation of SiC into SiO_2 did occur, even in a relatively short, 120 seconds exposure.

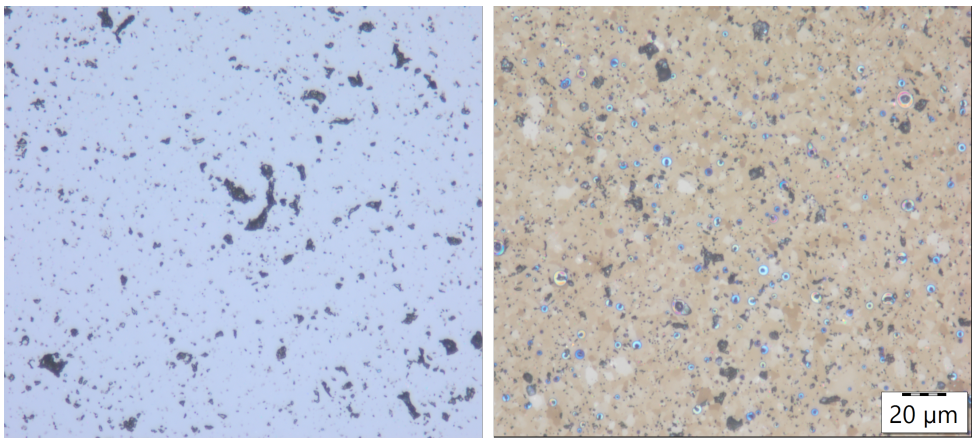

Figure 4.13.: Nomarski microscopy images of sample IRS-01 at 50x magnification: before (left) and after (right) PWK3 test.

Surface Defect Due to Porous Structure

The following Figure shows one of the largest surface defects on the surface of IRS-01. Before plasma exposure (Figure 4.14, left) the defect is a large, irregular dark formation approximately 40–50 µm in diameter with non-uniform internal structure and irregular boundaries. After plasma exposure (Figure 4.14, right), the defect maintains its size and shape but exhibits enhanced internal contrast and a lighter central region, that might indicate localized oxidation.

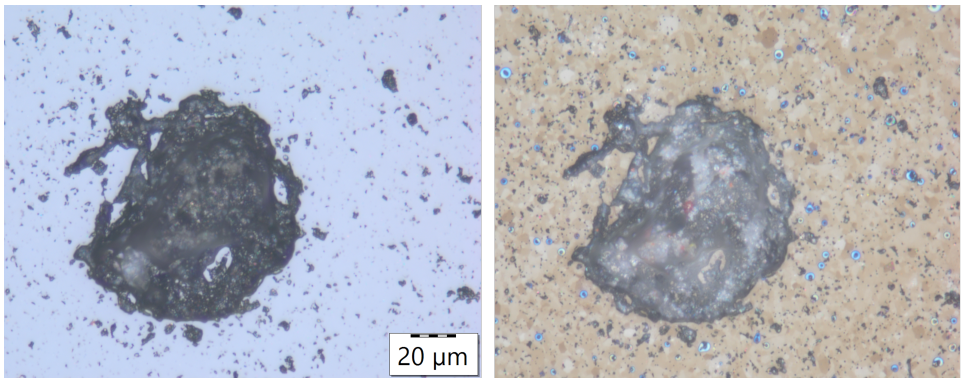

Figure 4.14.: Nomarski microscopy images of a surface defect in sample IRS-01 at 50x magnification: before (left) and after (right) PWK3 test.

Such localized defects could negatively impact the overall smoothness and specularity of the surface. In other words, while a SiO_2 film may be present, the presence of these scattered defects could disrupt the mirror-like reflectivity required for an efficient specular intake design.

4.1.3.4. Surface and Element Analysis Using SEM/EDX

The SEM/EDX analysis of the plasma-exposed IRS-01 sample provided valuable insights into the elemental composition of the near-surface region. While EDX does not determine the exact chemical states or the thickness of layers, the detection of key elements and their relative distributions strongly suggests that the oxidation of SiC to SiO_2 occurred during plasma exposure.

Regions corresponding to defects associated with porosity exhibited minimal oxidation and trace levels of Al. This indicates that these areas may have been less exposed to the oxidative environment or shielded by intrinsic material properties.

A detailed SEM examination (Figure 4.15, left) of one of the larger crystalline structures, previously observed under Nomarski microscopy, revealed a complex surface morphology. The EDX spectra (Figure 4.15, right) detected the presence of boron, which is hypothesized to originate from the manufacturing or polishing processes. During polishing, boron nitride (BN) is commonly used as a protective coating

for some samples. Residual BN, which was not entirely removed prior to plasma testing, may have been mechanically introduced into the surface during machining or polishing, leading to contamination. This contamination highlights the critical need for meticulous cleaning and preparation steps to ensure reliable material characterization and to avoid misleading results. Additionally, darker regions in the SEM image exhibited the highest oxygen levels, suggesting more extensive oxidation in these areas. This observation reinforces the hypothesis that these regions serve as the initial sites for the formation of the SiO_2 layer.

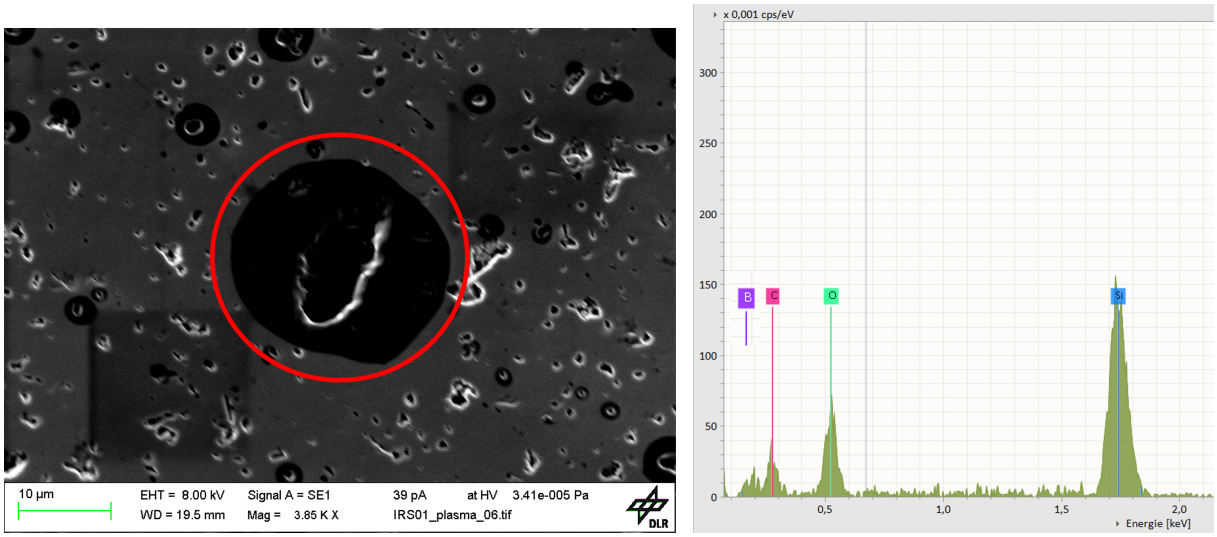

Figure 4.15.: SEM image of a crystalline structure (left) and EDX spectra of the area highlighted in red (right) in sample IRS-01.

4.1.4. Results for IRS-03 (300 s Exposure)

Sample IRS-03 was exposed to oxygen plasma for 5 minutes in the PWK3 facility. The plasma parameters achieved during the test are provided in the Test Matrix in Section 3.8 (Test ID: 220). The sample temperature was recorded using the LP3 linear pyrometer. As shown in Figure 4.16, the maximum measured temperature T_m was 1334.30 K at 300.95 s, corresponding to a corrected maximum temperature T_w of 1426.50 K. The sample did not reach a steady-state temperature before the end of the test.

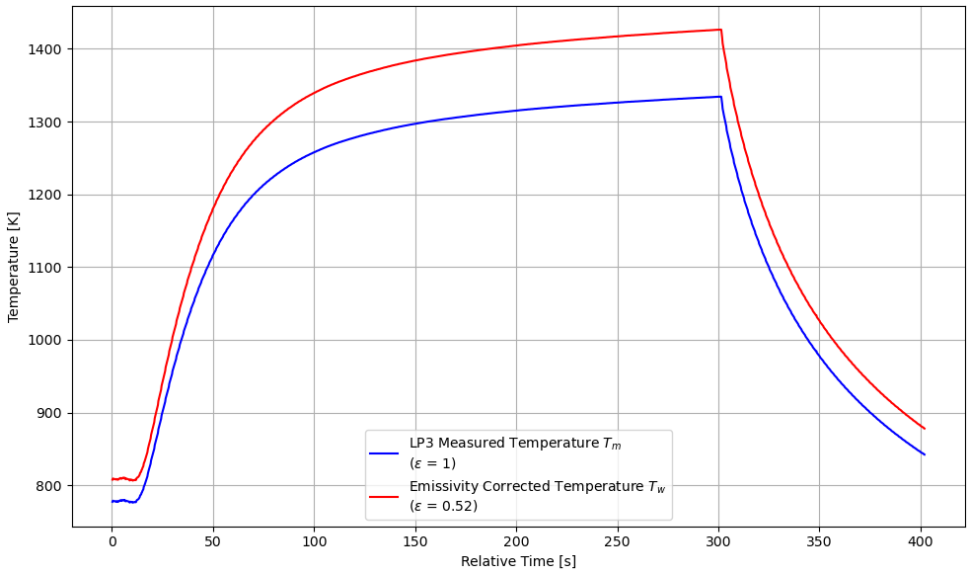

Figure 4.16.: Temperature-time profile for sample IRS-03 during PWK3 test and subsequent cooling period.

4.1.4.1. Surface Roughness Measurements with WLIM

Table 4.4 summarizes the surface roughness parameters of IRS-03 before and after plasma exposure for 300 s.

Table 4.4.: Surface roughness parameters for sample IRS-03 before and after plasma exposure

Parameter	Pre-Exposure	Post-Exposure
Arithmetic Mean Roughness (S_a), nm	16.05 ± 1.13	18.35 ± 0.54
Root Mean Square Roughness (S_q), nm	24.58 ± 2.01	30.23 ± 2.75
Maximum Height of the Surface (S_z), nm	334.20 ± 35.77	1066.70 ± 503.58

This behavior suggests that a more uniform oxidation process may be taking place over the longer exposure period, potentially allowing for a more coherent SiO_2 layer to form. Although not perfectly smooth, the relative moderation in surface feature growth after a 300 s exposure may indicate a trend toward the controlled development of an oxide film. Such a partial transition toward a more stable SiO_2 layer could be beneficial in achieving improved properties necessary for specular reflectivity in ABEP intakes.

4.1.4.2. Visual Results After the Test

During the test, the critical surface became gold/red and remained so for several minutes due to the high temperatures achieved. After the 5-minute exposure, sample IRS-03 underwent a notable transformation in visual appearance, transitioning from a light, polished finish to a darkened, matte black state. The central area of the sample appeared significantly darker and more uniform compared to part of the surrounding edge, which was lighter in color. This observation suggests differences in oxidation or heat distribution during the test. The lighter-colored edge effect may be caused by non-uniform plasma heating, material interaction with the fixture causing thermal gradients, or diffusion of oxygen affecting the sample edge. Additionally, the sample exhibited a slight violet hue when viewed from certain angles, indicating interference effects due to oxide layer thickness variations.

4.1.4.3. Surface Analysis with Nomarski Microscopy

The initial surface condition (Figure 4.17, left) shows a uniform light blue coloration with minimal surface texture variations. After 5 minutes of oxygen plasma exposure (Figure 4.17, right), the surface exhibits a pronounced shift to a deeper blue coloration, indicating oxide layer formation. The post-exposure surface maintains the original surface topography and shows significant color transformation and the development of thin-film interference effects, suggesting non-uniform oxide thickness.

At 50x magnification (Figure 4.18, left), the pre-exposure surface exhibits dark regions representing material porosity. After plasma exposure (Figure 4.18, right), a continuous crystalline-like surface oxide layer with intense blue coloration forms over the porous structure.

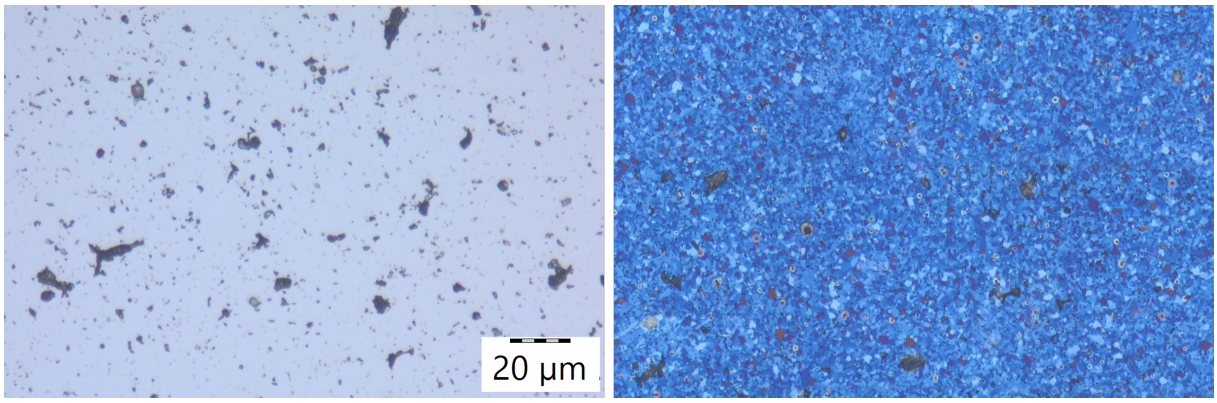

Figure 4.18.: Nomarski microscopy images of sample IRS-03 at 50x magnification: before (left) and after (right) PWK3 test.

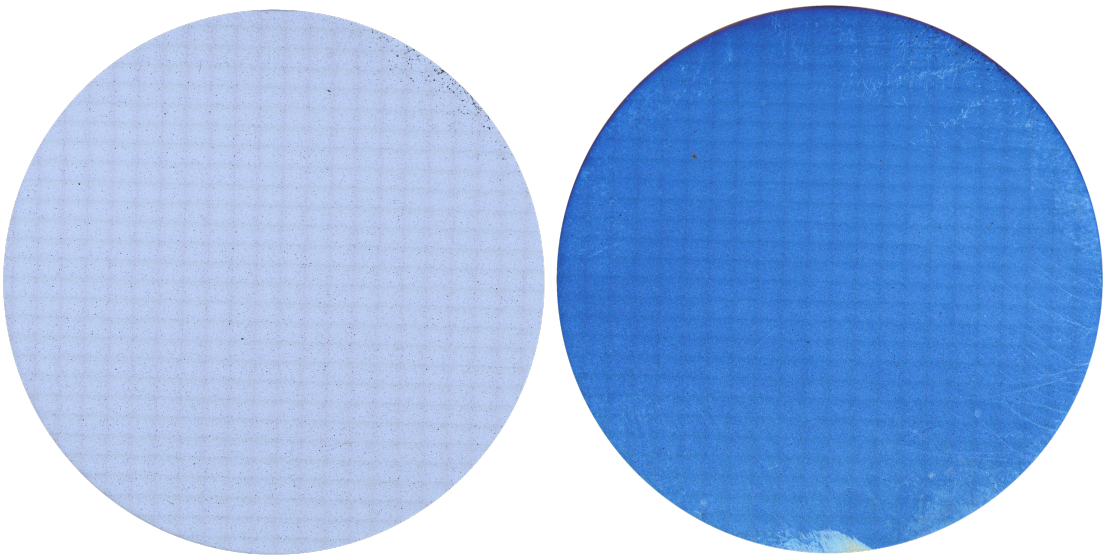

Figure 4.17.: Stitched Nomarski microscopy images of sample IRS-03 at 10x magnification: before (left) and after (right) PWK3 test.

The surfaces of the exposed samples reveal distinctive features that immediately stand out due to their unique morphology. These peculiar structures, which differentiate themselves from the surrounding areas, could provide critical insights into the processes and transformations occurring under plasma exposure. Among these features, dendritic-like structures and circular formations represent two key morphological phenomena observed post-exposure.

The pre-exposure micrograph (Figure 4.19, left) reveals a metallic-like region with a gold-colored hue and an irregular morphology, indicative of surface contamination, potentially Al. Following plasma exposure (Figure 4.19, right), this region evolves into a dendritic-like structure approximately 200 µm in diameter, characterized by radial branching patterns. This transformation suggests the breakdown and restructuring of the contaminant under the influence of plasma conditions.

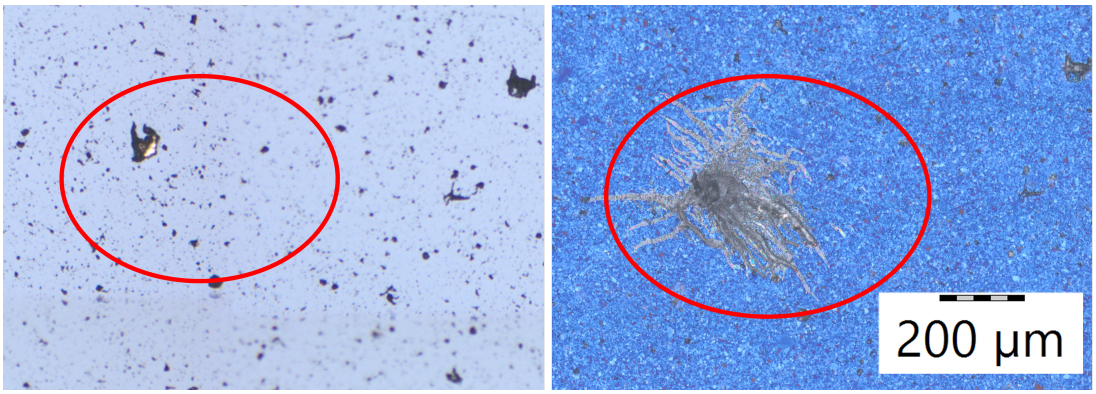

Figure 4.19.: Nomarski microscopy images of a dendritic-like structure in sample IRS-03: pre-exposure (left) and post-exposure (right) during the PWK3 test.

After exposure (Figure 4.20, right), there is the formation of circular structures that exhibit pronounced purple-gold oxidation rings, likely indicating incomplete oxide layer formation.

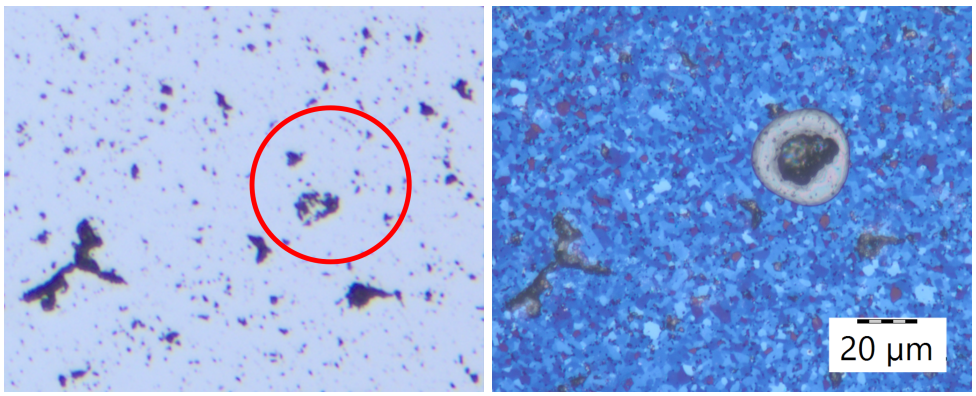

Figure 4.20.: Nomarski microscopy images of a circular formation in sample IRS-03 at 50x magnification: before (left) and after (right) PWK3 test.

4.1.4.4. Surface and Element Analysis with SEM/EDX

In defect-free regions of sample IRS-03, EDX analysis revealed a significant increase in oxygen content compared to the pre-plasma state. The measured counts (0.3 cps/eV for oxygen, 0.95 cps/eV for silicon, and 0.1 cps/eV for carbon) provide strong evidence for surface oxidation and the formation of a SiO_2 layer.

A detailed SEM image of a circular void structure is presented in Figure 4.21 (left). The void displays a well-defined circular morphology with a diameter of approximately 3 µm. EDX analysis of this area revealed elevated oxygen counts relative to silicon, with minimal carbon detected. This indicates that these structures are regions of advanced oxidation. Notably, the centers of the voids exhibited incomplete oxidation, as only silicon was detected, suggesting ongoing oxidation processes.

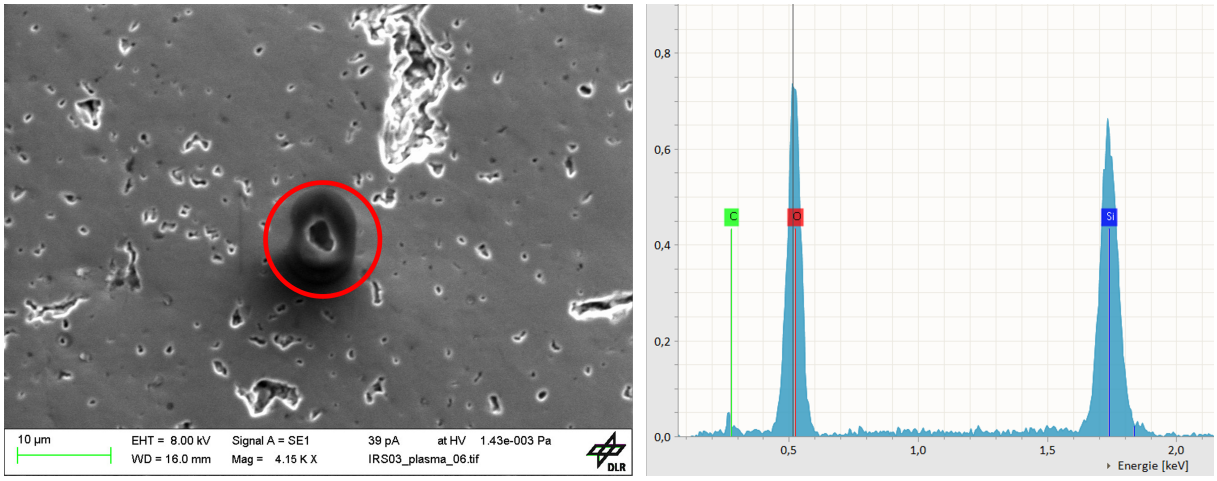

Figure 4.21.: SEM image of a circular void structure on the surface of sample IRS-03 after plasma exposure (left) and EDX spectra of the area highlighted in red (right).

Attempts to perform EDX analysis on the dendritic-like structures were unsuccessful due to signal interference, likely resulting from their complex morphology and possible charging effects. Further investigation is required to fully characterize these unique surface features. For sample IRS-03, which underwent a 300-second plasma exposure, a more robust formation of the SiO_2 layer was observed. This was evidenced by optical interference patterns and strong EDX indications of oxygen incorporation. While defects and non-uniformities persist, the longer exposure duration demonstrates the chemical feasibility of forming a silica coating under these conditions.

4.1.5. Results for IRS-05 (600 s Exposure)

Sample IRS-05 was exposed to oxygen plasma for 10 minutes in the PWK3 facility. The plasma parameters achieved during the test are provided in the Test Matrix in Section 3.8 (Test ID: 221). The sample temperature was recorded using the LP3 linear pyrometer. As shown in Figure 4.22, the maximum

measured temperature T_m was 1351.10 K at 575.33 s, corresponding to a corrected maximum temperature T_w of 1445.72 K. The sample achieved a steady-state temperature towards the end of the test, as indicated by the plateau in the temperature-time profile.

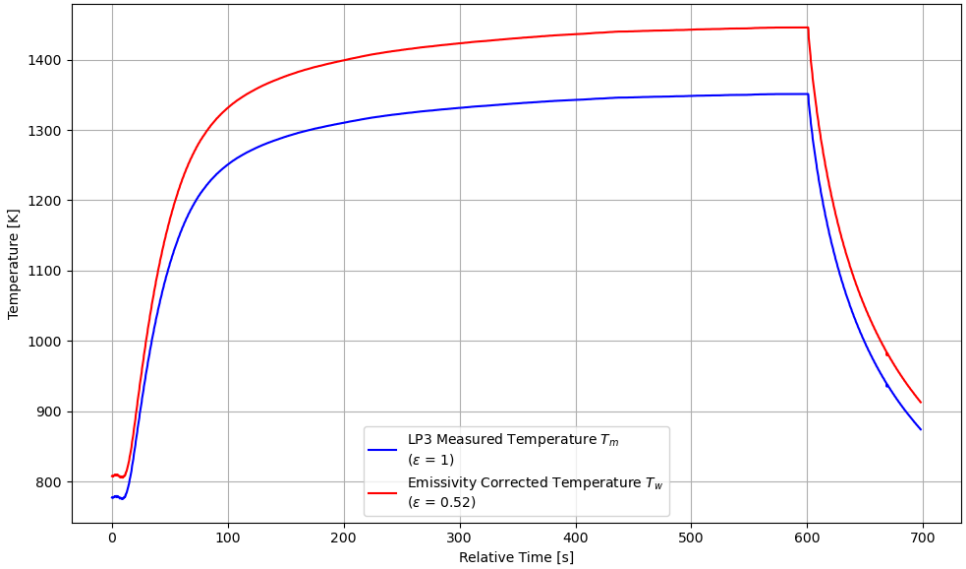

Figure 4.22.: Temperature-time profile for sample IRS-05 during PWK3 test and subsequent cooling period.

4.1.5.1. Surface Roughness Measurements with WLIM

Table 4.5 presents the surface roughness parameters of IRS-05 before and after plasma exposure for 600 s.

Table 4.5.: Surface roughness parameters for sample IRS-05 before and after plasma exposure

Parameter	**Pre-Exposure**	**Post-Exposure**
Arithmetic Mean Roughness (S_a), nm	15.29 ± 0.91	19.38 ± 0.99
Root Mean Square Roughness (S_q), nm	23.19 ± 2.62	46.84 ± 10.11
Maximum Height of the Surface (S_z), nm	432.63 ± 88.23	1901.02 ± 749.41

The S_a and S_q increase notably, and the S_z rises substantially. The intermediate severity of roughness escalation suggests that, over this extended duration, oxidation processes may have facilitated the growth of a thicker SiO_2 layer. While the surface still becomes rougher, the morphological changes might be more systematic and less erratic than those observed for shorter exposures. This could imply that prolonged exposure fosters a more stable and cohesive oxide formation, although it may remain imperfect.

4.1.5.2. Visual Results After the Test

During the test, the critical surface became gold/red and remained so for several minutes due to the high temperatures achieved. After the 10-minute exposure, sample IRS-05 displayed a noticeable darkening or matte effect, indicative of surface oxidation or deposition of a plasma-induced layer. The reflectivity decreased significantly compared to the pre-test state, evidencing an increase in surface roughness or microstructural alterations due to high-temperature plasma interaction. Additionally, a reddish-like area was observed at one edge of the critical surface, standing out against the otherwise darkened surface. This discoloration suggests a localized reaction or contamination during the test, potentially due to localized overheating or contamination from the probe or surroundings.

4.1.5.3. Surface Analysis with Nomarski Microscopy

The pre-exposure Nomarski image (Figure 4.23, left) shows a uniformly polished surface with a uniform light blue and minimal topographical variations. After 600 s of plasma exposure (Figure 4.23, right), the surface exhibits a turquoise-green coloration and interference patterns indicative of oxide formation. A distinct reddish-like area appears at the bottom edge might indicate localized thermal or chemical interactions.

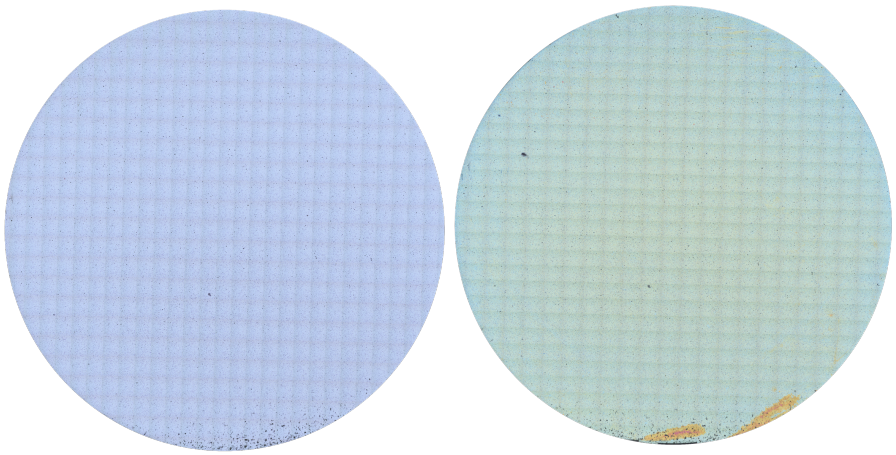

Figure 4.23.: Stitched Nomarski microscopy images of sample IRS-05 at 10x magnification: before (left) and after (right) PWK3 test.

At higher magnification (Figure 4.24), the post-exposure surface shows intense interference colors, reflecting variations in oxide thickness across the porous substrate. Dendritic-like and bubble-like features are also noted, reminiscent of those found on IRS-03.

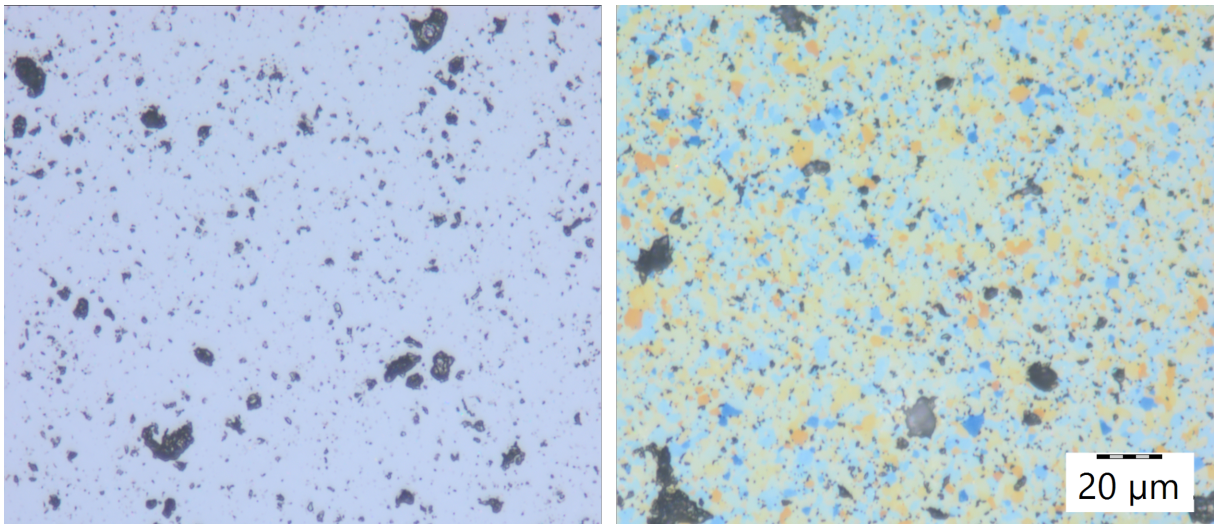

Figure 4.24.: Nomarski microscopy images of sample IRS-05 at 50x magnification: before (left) and after (right) PWK3 test.

4.1.5.4. SEM/EDX Surface and Elemental Analysis

A detailed SEM/EDX investigation was performed to confirm the chemical composition changes associated with prolonged plasma exposure. Figure 4.25 shows a representative SEM micrograph of a region on the plasma-exposed IRS-05 surface. The image reveals a network of crystalline-like oxide structures and

localized defects, including circular voids and dendritic formations, similar to those noted under Nomarski microscopy.

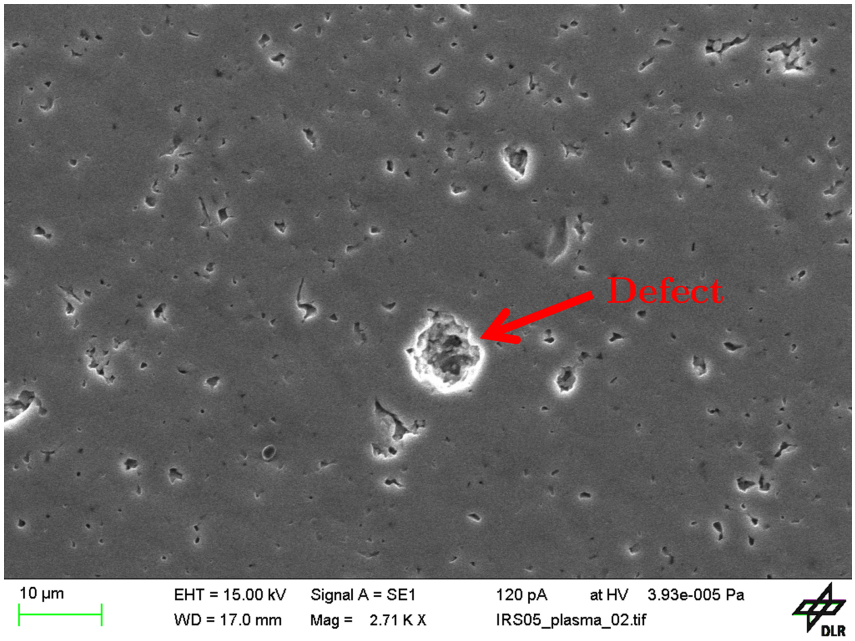

Figure 4.25.: SEM image of IRS-05 after 600 s plasma exposure, showing crystalline-like oxide structures and localized defects due to the porous material.

EDX analyses performed on smoother regions of the sample consistently detected silicon and oxygen as the dominant elements, with significantly low carbon signals. This elemental signature strongly indicates the formation of an SiO_2 layer. Figure 4.26 illustrates a typical EDX spectrum obtained from a relatively uniform area of the oxide surface. The dominant Si and O peaks, coupled with the reduced C, support the conclusion that a stable silica layer has formed.

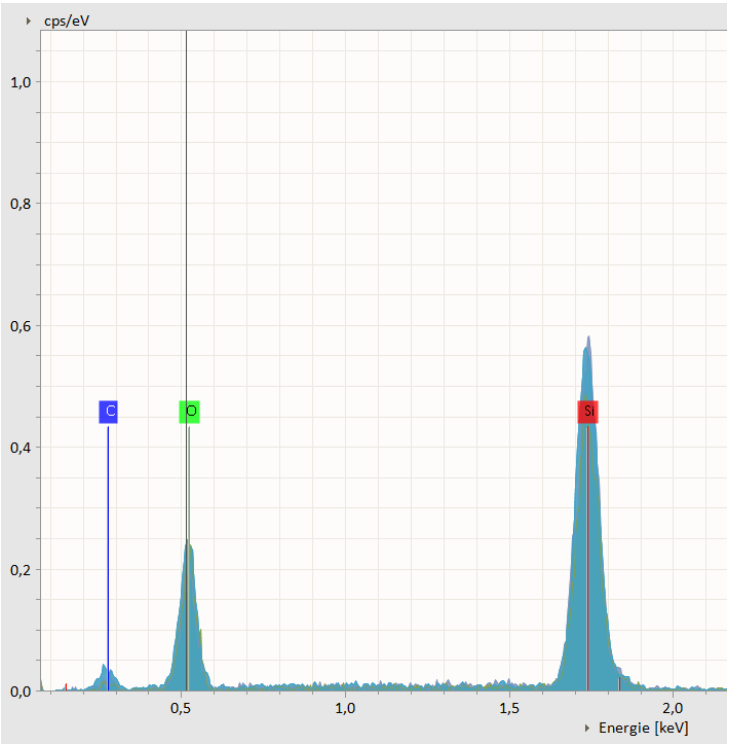

Figure 4.26.: Representative EDX spectrum of a clean area IRS-05 after plasma exposure, showing prominent Si and O signals consistent with a SiO_2 layer.

4.1.6. Surface Roughness Considerations

Across all exposure conditions, WLIM measurements indicate that S_a, S_q, and S_z generally increase after plasma exposure, reflecting the development of more complex surface morphologies. Longer exposure times tend to produce more systematic oxide formation, suggesting a partial transition toward stable SiO_2 layers. However, variations in roughness values obtained from different WLIM setups, as well as comparisons to AFM measurements, highlight the sensitivity of these results to instrument configuration and measurement modes. Additional details regarding the variability in WLIM measurements and their dependence on system parameters are provided in Appendix A.7.

4.1.7. SiC Samples Overall Results

The PWK3 tests conducted provided initial insights into the progressive oxidation behavior of polished SiC under high-temperature oxygen plasma exposure. By maintaining consistent plasma conditions (see Appendix A.5), observed variations in oxide formation could be linked primarily to exposure duration. Longer exposures led to more pronounced interference patterns, altered surface topography, and evidence of a thicker oxide scale as inferred from microscopy and SEM/EDX analyses.

However, it is important to note that the presented quantitative estimates for the relative percentages of SiC and SiO_2 in Table 4.6 are preliminary and require further validation. The SEM/EDX scans were conducted at accelerating voltages (E_0) of approximately 7–8 keV. According to the normogram discussed in Appendix A.8, for SiC with a density of 3.17 g/cm^3, an electron beam energy of 1 kV roughly corresponds to a penetration depth of 0.1 μm. Thus, at 7–8 keV, the estimated penetration depth would be on the order of 0.7 μm. Since the objective here was to characterize the oxide layer, analyzing at these voltages may introduce signals from deeper substrate regions, potentially skewing the compositional interpretation. In other words, the detected oxygen may be influenced by both near-surface oxide and underlying SiC, making the precise quantification of SiO_2 challenging without more refined EDX conditions.

Table 4.6.: Calculated relative percentages of SiC, SiO_2, and SiO on defect-free surface areas of samples IRS-01, IRS-03, and IRS-05 after plasma exposure (E_0 = 7 to 8 KeV).

Sample	**SiC (%)**	**SiO_2 (%)**
IRS-01 (120 s)	79.51	20.49
IRS-03 (300 s)	61.91	38.09
IRS-05 (600 s)	38.95	61.05

For IRS-05, an additional scan was performed at $E_0 = 15$ keV, which resulted in detecting less oxygen compared to the 7–8 keV scan. This suggests that the deeper interaction volume at higher accelerating voltages encompasses more of the SiC substrate and dilutes the apparent surface oxide signature. Such results imply that the previously discussed percentages may not be entirely accurate as they do not isolate the topmost oxide layer. Instead, they represent a convolution of surface oxide and underlying substrate contributions. To more confidently characterize the SiO_2 layer, it will be necessary to vary E_0 systematically, performing multiple EDX scans at different accelerating voltages and comparing the resulting element distributions.

Future SEM/EDX investigations should include lower E_0 scans (e.g., 3–5 keV) to probe less depths and more accurately reflect the true surface oxide composition. Cross-sectional analyses, if feasible, and complementary techniques such as X-ray Photoelectron Spectroscopy (XPS) or Transmission Electron Microscopy (TEM) coupled with Electron Energy Loss Spectroscopy (EELS) may further clarify the oxide layer's thickness and composition.

In summary, although the current results suggest an increasing SiO_2 content with longer exposure times, the actual oxide percentages are subject to uncertainty due to penetration depth effects and substrate interference. Additional studies are required to resolve these ambiguities and to confirm whether the SiO_2 enrichment inferred here accurately represents the true state of the near-surface oxide layer.

4.2. PECVD SiO_2 Coating Characterization

Building upon the insights gained from the SiC polished passivation results presented in Section 4.1, this section focuses on evaluating the feasibility of achieving a specular SiO_2 coating on Gold-Nickel intake

substrates via PECVD. By comparing the outcomes, it is possible to discern differences in layer formation mechanisms, substrate interactions, and the ultimate viability of these coatings for applications in ABEP intake systems.

This section examines the behavior of Gold-Nickel intake samples subjected to a SiO_2 coating process via PECVD. The central objective of this investigation is to determine whether a specular SiO_2 layer can be achieved on these metallic substrates and, if not, to understand the factors that prevent the formation of an optically smooth and uniform oxide film. The analysis focuses on characterizing the surface both before and after coating, using Nomarski microscopy, SEM/EDX, and AFM techniques. Particular attention is paid to the formation of irregular features such as hemispherical protrusions, defects, and clustered regions, as well as their implications for surface quality and the potential impact on ABEP applications.

4.2.1. Visual Inspection

The Gold-Nickel intake samples, labeled as 368-12 and 807-6, were examined visually prior to the coating process. Both samples displayed a distinctive gold hue with pronounced luminescence and a smooth, polished surface, indicative of high-quality fabrication (Figure 4.27). Notably, the samples were produced using different mandrels, a factor that may have contributed to variations in their surface details that will be discussed in this section.

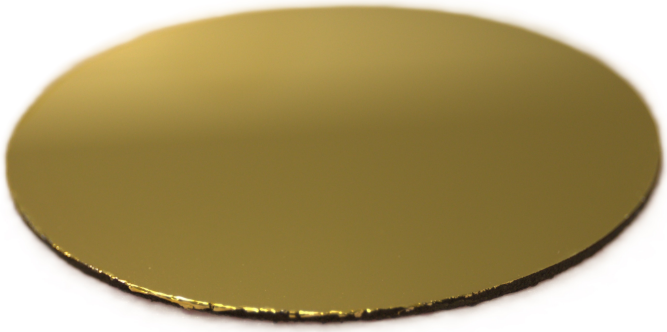

Figure 4.27.: Gold-Nickel intake sample 807-6 prior to coating. Both samples display a gold color with high luminescence and a highly polished surface.

Post-coating evaluation revealed a slight increase in surface scratches, likely introduced during transportation, the coating process, or possibly during the AFM static mode measurements. However, the overall appearance of the surface remained similar to the pre-coating condition in terms of color and reflectivity.

4.2.2. Surface Roughness Results

In the previous investigations on SiC samples, the reduction in surface roughness and controlled oxidation underscored the importance of achieving a smooth and uniform passivation layer to maintain specular reflection properties. For the Gold-Nickel samples, the initial roughness levels were even lower than the polished SiC surfaces, suggesting a promising starting point for creating a high-quality SiO_2 coating. However, the outcomes after PECVD deposition differed significantly.

Initially, the WLIM was employed to analyze the roughness of the samples before coating. However, due to the WLIM's limitations in measuring roughness below 1 nm (see Appendix A.2), even in PSI mode, the AFM was utilized instead. The AFM provided more accurate and detailed information on the nanoscale surface characteristics of the Gold-Nickel intake samples, both before and after the SiO_2 coating. Detailed roughness analysis for both samples in different areas before and after coating is provided in Appendix A.3.1.

Tables 4.7 and 4.8 summarize the roughness parameters for samples 368-12 and 807-6, respectively, before and after the PECVD SiO_2 coating. For the pre-coating analysis on 368-12, all investigated areas were

relatively clean and defect-free, while the post-coating areas deliberately included hemispherical features to capture the most significant changes. Similarly, for 807-6, representative areas were chosen to highlight surface evolution after coating.

Table 4.7.: AFM roughness parameters for sample 368-12 (pre- and post-coating)

Condition	$\mathbf{S_a}$ (nm)	$\mathbf{S_q}$ (nm)	$\mathbf{R_z}$ (nm)
Pre-coating	0.235 ± 0.100	0.372 ± 0.158	15.31 ± 6.52
Post-Coating	4.320 ± 3.398	8.670 ± 5.060	327.34 ± 272.33

Table 4.8.: AFM roughness parameters for sample 807-6 (pre- and post-coating)

Condition	$\mathbf{S_a}$ (nm)	$\mathbf{S_q}$ (nm)	$\mathbf{R_z}$ (nm)
Pre-Coating	0.199 ± 0.045	0.655 ± 0.633	62.70 ± 74.29
Post-Coating	3.660 ± 0.828	12.07 ± 11.66	1153.7 ± 1366.9

The increase in surface roughness after coating is substantial. Before coating, both samples exhibited sub-nanometer scale roughness, reflecting their high-quality, mirror-like finish. Such low roughness values are essential for applications requiring specular reflection. After the SiO_2 deposition, roughness parameters escalated by more than an order of magnitude, introducing highly irregular topographies with prominent nanoscale features. This sharp increase in roughness suggests that the deposited oxide layer was not uniformly smooth and may have formed through non-ideal nucleation or growth mechanisms, leading to a pronounced deterioration in the specular properties that the original substrates possessed.

4.2.2.1. Detailed AFM Analysis

The pre-coating surface of sample 368-12 exhibits a relatively uniform topography, with an average roughness (S_a) of around 0.235 nm. The AFM images (Appendix A.3.1) show a smooth morphology, indicating a substrate well-suited for receiving a conformal and uniform SiO_2 layer.

After the SiO_2 coating, the surface of 368-12 demonstrates a dramatic increase in roughness, with S_a rising to approximately 4.320 nm. This jump in roughness is even more striking when considering R_z, which escalates from about 15 nm to over 300 nm, revealing the development of significant vertical features. The topographical data reveal a distinct pattern of hemispherical protrusions and irregular surface structures scattered across the surface. These features vary in diameter and height, as shown in the derived topographical maps.

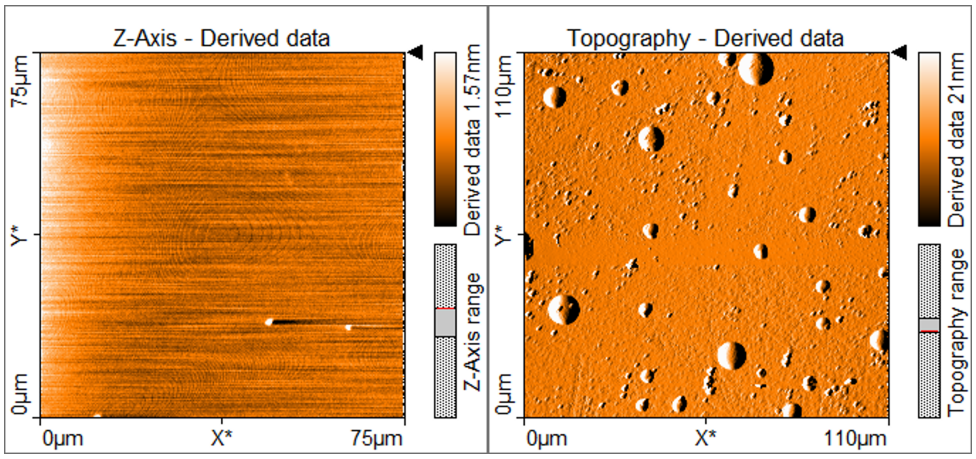

Figure 4.28.: AFM microscopy images of sample 368-12: (left) Pre-coating surface in static mode; (right) Post-coating surface in dynamic mode. The post-coating surface shows pronounced hemispherical features and increased roughness. Dark regions near these features are tip-shadowing artifacts due to steep topography.

As shown in Figure 4.28, the pre-coating scan presents a relatively uniform surface with only minor nanoscale variations. In contrast, the post-coating scan reveals large, dome-like formations. The dark regions adjacent to these hemispherical structures in the post-coating image represent AFM artifacts resulting from the tip's limited ability to accurately trace highly curved or steep surfaces.

Hemispherical Surface Features Characterization

Further insights into the hemispherical surface features were obtained by rescanning the same area twice. During the first scan, the dome-shaped protrusion appeared intact. However, a second scan over the same area showed a ring-like depression at the feature's center (Figure 4.29). This deformation indicates that the AFM tip may have mechanically disrupted the feature, potentially puncturing a thin SiO_2 shell or collapsing a gas-filled pocket within the coating.

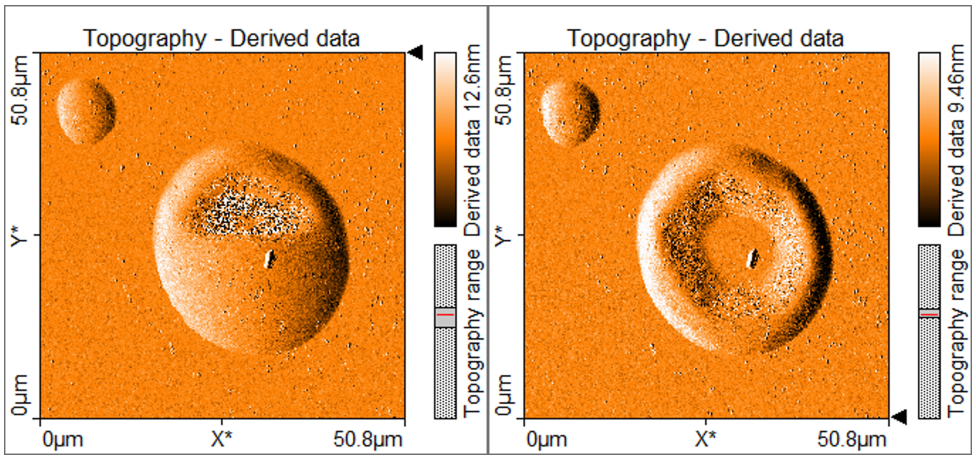

Figure 4.29.: AFM images of sample 368-12 post-coating, Area H: (left) First scan shows an intact hemispherical feature; (right) Second scan reveals a ring-like depression, suggesting mechanical damage inflicted by the AFM tip.

The susceptibility of these hemispherical structures to mechanical damage implies that the coating may be fragile or non-densified. Such fragility reduces the likelihood of obtaining a stable and mechanically resilient specular layer. Instead, these dome-like features could be weaknesses in the coating, prone to cracking or flaking under operational stresses.

Cluster Structure

In addition to hemispherical protrusions, cluster formations were identified on the coated surface. The cluster depicted in Figure 4.30 shows an irregular, elevated region with a Z-range of approximately 20 nm. This localized agglomeration likely results from non-uniform deposition, contamination acting as nucleation sites, or plasma instabilities during the PECVD process.

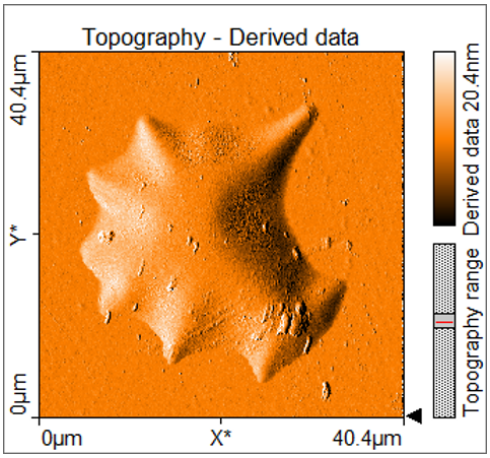

Figure 4.30.: AFM image of sample 368-12 post-coating, Area F. The cluster formation shows significant height variations, suggesting localized agglomeration of coating material.

Such clusters not only increase roughness but may also induce stress concentrations within the coating. Their presence could compromise mechanical stability or adhesion, ultimately reducing the coating's durability and uniformity.

Amplitude Data Analysis

Amplitude data from the AFM measurements did not indicate significant differences in interaction forces or material properties between hemispherical features and the surrounding areas. This uniformity in amplitude response suggests that the hemispherical protrusions and clusters arise from morphological changes rather than compositional inhomogeneities at the nanoscale. In other words, the underlying material—SiO_2—appears similar in character, but the deposition process or environmental factors have created uneven thicknesses or trapped pockets of gas.

4.2.2.2. Overall AFM Observations and Considerations

In contrast to the relatively stable and progressive passivation observed in SiC samples exposed to high-enthalpy oxygen plasma (Section 4.1), the SiO_2 coatings on Gold-Nickel substrates exhibit a range of irregular topographical features after PECVD. The AFM analysis reveals:

- **A dramatic increase in surface roughness,** transforming the mirror-like pre-coating substrate into a surface studded with dome-like protrusions and clustered formations.
- **Hemispherical features that are mechanically fragile,** as evidenced by their deformation under repeated AFM scanning.
- **Localized clusters and non-uniform depositions** that suggest contamination, non-ideal process conditions, or inadequate surface preparation prior to coating.

These findings indicate that achieving a smooth, stable SiO_2 coating capable of supporting specular reflection is challenging under the current PECVD conditions, especially considering the non-cleanroom environment in which the deposition was performed. The irregularities and features identified by AFM not only compromise the optical and aerodynamic requirements for potential ABEP intakes but also raise concerns about the mechanical robustness and long-term stability of the coating.

Moreover, the absence of pronounced compositional differences—implied by uniform amplitude response—points to process-related issues rather than fundamental material incompatibility. Adjusting plasma parameters, improving substrate cleaning procedures, or optimizing precursor flow and deposition conditions might help mitigate these irregularities. Without such improvements, the SiO_2 coatings produced under the given conditions may fail to match the smoothness and uniformity necessary for high-performance ABEP intake applications.

4.2.3. Analysis with Nomarski and SEM/EDX Microscopy

Having established the significant roughness increase and the presence of hemispherical features and clusters via AFM analysis, the next step involves examining the samples through Nomarski microscopy and SEM/EDX. These additional techniques provide complementary perspectives on surface morphology and composition. While SEM/EDX was not available before coating due to maintenance, the post-coating analysis helps infer changes induced by the deposition process and offers clues about the layer formation mechanisms.

4.2.3.1. Surface Differences Pre and Post Coating

Nomarski microscopy was employed to examine the surface morphology of the samples before and after the SiO_2 coating process. Because SEM/EDX analysis could not be performed prior to coating, the comparison relies mainly on the optical observations from Nomarski microscopy for the pre-coating state and on SEM/EDX for the post-coating state.

Before coating (Figure 4.31a), both samples appeared relatively smooth and uniform, displaying a light beige hue and minimal surface imperfections. Sample 807-6 exhibited slightly more surface defects than 368-12, potentially attributable to the use of an older mandrel during its fabrication. Nonetheless, these imperfections were not severe and did not significantly disrupt the overall smoothness. After SiO_2 deposition (Figure 4.31b), the surface morphology under Nomarski microscopy changed notably. Although

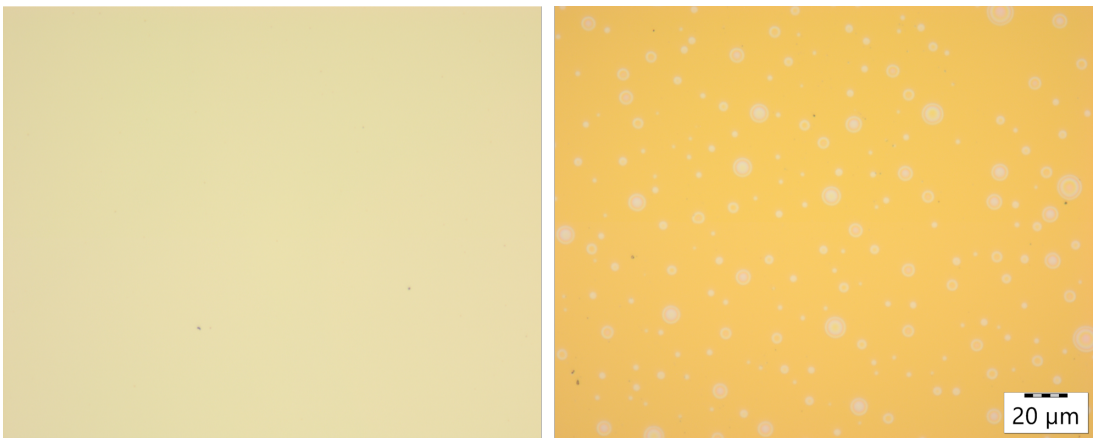

Figure 4.31.: Nomarski microscopy images of sample 807-6 at 50x magnification: (left) before coating, (right) after coating. The color differences observed are due to optical interference effects of Nomarski microscopy rather than actual material color changes.

the observed color variations primarily stem from optical interference effects intrinsic to the Nomarski technique, a distinct pattern of hemispherical surface features became evident. These features range from a few micrometers up to tens of micrometers in diameter and appear regularly distributed. Such a transformation strongly suggests that the coating process influenced surface topography, introducing new structures not present before.

Hemispherical Surface Features Observed under SEM/EDX

Further insights into the hemispherical surface features were obtained by examining them with SEM/EDX. An SEM scan of sample 368-12 at 2,210x magnification and $E_0 = 8$ keV is shown in Figure 4.32. Under SEM, the hemispherical protrusions appear darker than the surrounding areas, indicating possible topographic or compositional variations from the surrounding matrix.

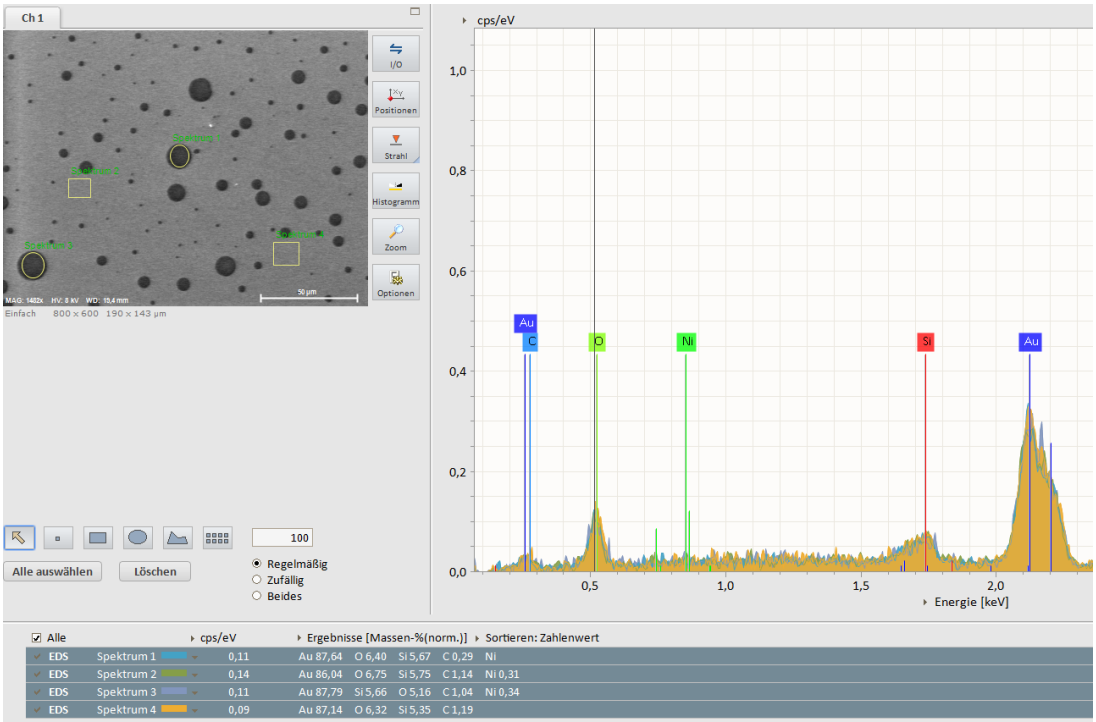

Figure 4.32.: SEM/EDX scan of sample 368-12 post-coating at 2,210x magnification and $E_0 = 8$ keV. Hemispherical features appear darker, suggesting morphological or compositional differences from the surrounding matrix.

Preliminary EDX analysis on various regions—both those containing hemispherical features and cleaner areas—indicates similar elemental compositions, with Si and O peaks expected from the SiO_2 coating. Interestingly, gold (Au) signals are also detected in both types of regions, suggesting that the electron beam at $E_0 = 8$ keV penetrates through the relatively thin oxide layer, reaching the underlying gold layer. This implies that the oxide thickness may be quite small, or that the coating is not entirely uniform. The relative intensities of Si, O, and Au peaks vary, but no clear compositional distinction emerges between the hemispherical protrusions and the flat areas. This uniformity in composition suggests that the hemispherical features are not due to a different material but likely arise from structural or mechanical effects during deposition.

It must be noted that the choice of $E_0 = 7$–8 keV was constrained by experimental limitations. Without precise knowledge of the coated layer's density and thickness, this energy level was selected as a compromise to achieve signal from both the coating and the underlying substrate. Additional EDX scans at varying accelerating voltages could refine the understanding of layer thickness and composition. However, due to the complexity of analyzing these samples and equipment constraints, no such systematic voltage variation was performed. As a result, the current compositional insights remain preliminary and warrant further investigation.

4.2.3.2. Uniform Regions Without Hemispherical Formations

In certain areas, the post-coating surface appears more uniform and free of dome-like structures. Such regions typically appear as elliptical patches a few hundred micrometers in size (Figure 4.33). Their uniformity and lack of hemispherical features suggest that these areas represent more ideal coating conditions, potentially where surface contaminants, local chemistry, or process instabilities were minimized.

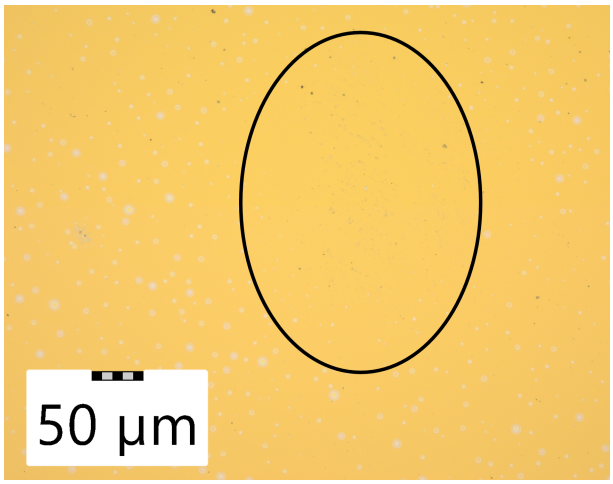

Figure 4.33.: Nomarski microscopy image illustrating a uniformly coated region without hemispherical surface features. These "clean" areas highlight the possibility of achieving more homogeneous coatings under optimized conditions.

These uniform patches are promising: they indicate that the PECVD process can produce smooth, defect-free coatings if conditions are favorable. The challenge is to replicate these conditions consistently over the entire substrate, ensuring a continuous, specular-quality SiO_2 layer.

4.2.3.3. Holes and Cavities

Pre-coating defects, such as holes or cavities in the gold-nickel substrate, persist after coating and remain partially or fully exposed (Figure 4.34). The presence of these larger flaws, measuring tens to hundreds of micrometers, can interrupt coating continuity and serve as vulnerability points.

SEM/EDX Analysis of Hole Features

SEM and EDX on these hole features (Figure 4.35) confirm the substrate's exposure. Spectrum analysis indicates high Ni content and reduced Au and Si signals in the hole's center, implying that the coating and upper layers were removed or never fully formed in these zones.

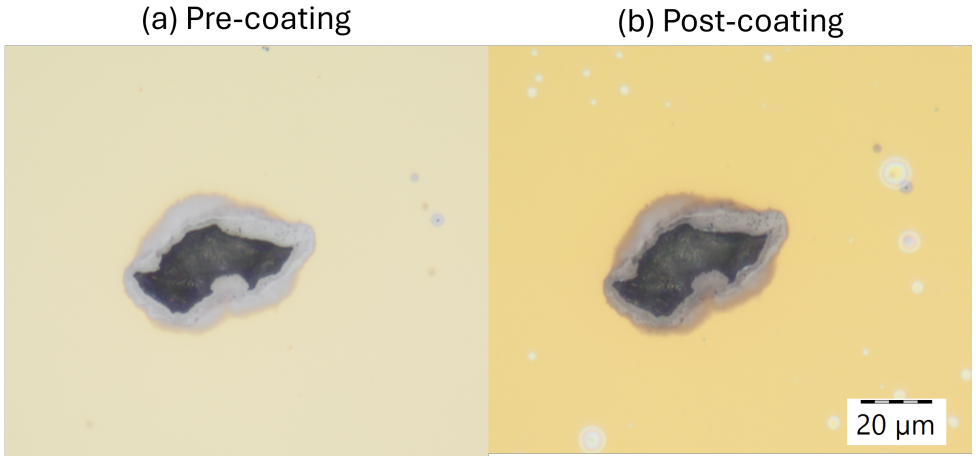

Figure 4.34.: Nomarski microscopy images of sample 807-6 at 50x magnification showing a hole feature: (left) before coating, (right) after coating. The hole persists post-coating, indicating incomplete coverage in defect regions.

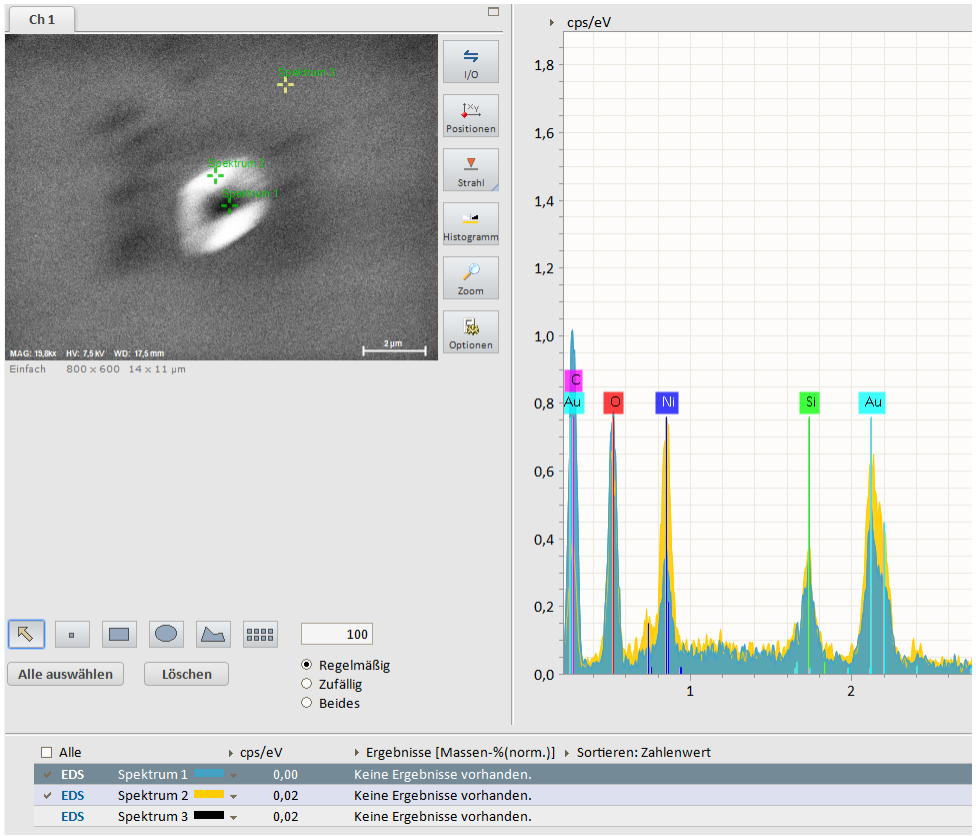

Figure 4.35.: SEM and EDX scan of a hole feature on sample 807-6. Due to the difficulties of the noise, the scan is not complete but could provide interesting results.

Given that the SiO_2 layer appears absent in the central areas of these holes, such defects could become hotbeds for corrosion or rapid oxidation in VLEO conditions. Testing these samples in an experimental apparatus [10] could quantify the degradation rate, providing insights into long-term performance.

4.2.3.4. Center Area Feature of Sample 807-6

The center area of sample 807-6 shows post-coating defects possibly introduced or exacerbated by AFM static mode measurements (Figure 4.36). Switching to dynamic mode measurements after coating indicates an awareness of tip-induced damage, highlighting the fragility of the coating. Minimizing mechanical contact and ensuring gentler characterization techniques could preserve the coating integrity and yield more representative data.

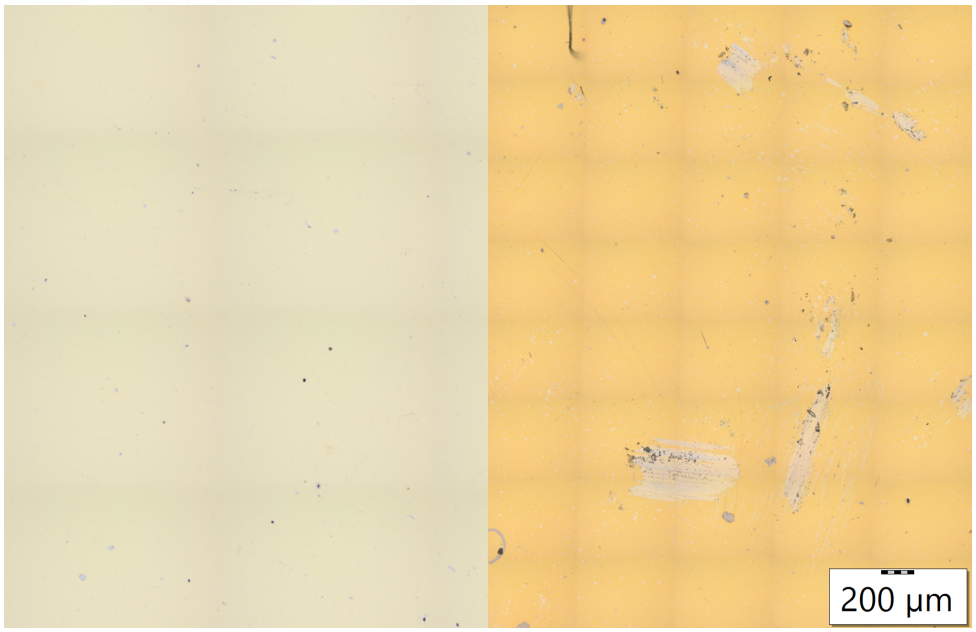

Figure 4.36.: Nomarski microscopy images of sample 807-6 at 50x magnification in the center area: (left) before coating, (right) after coating. Post-coating defects may be related to the AFM static mode measurements.

4.2.3.5. Cluster Formation After Coating

Clusters observed post-coating (Figure 4.37) resemble coalesced hemispherical features or regions where gas pockets and coating irregularities accumulate. These topographically elevated zones could be stress concentration points and may impact mechanical stability.

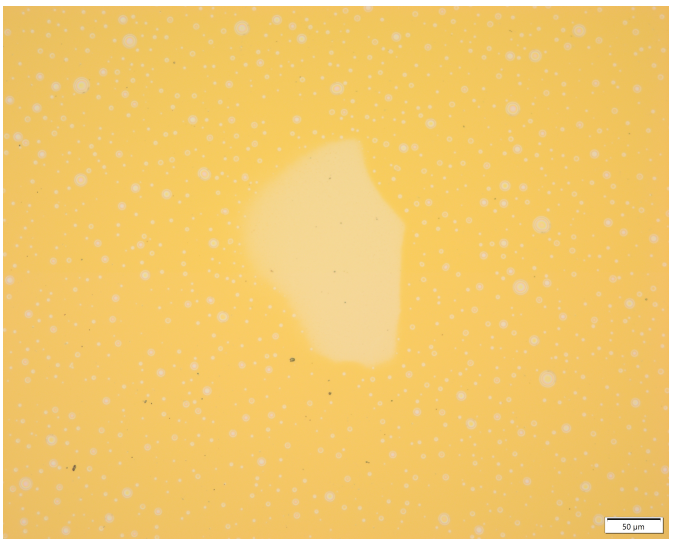

Figure 4.37.: Nomarski microscopy image of sample 368-12 at 50x magnification showing a cluster formation after coating. Such agglomerations represent localized coating anomalies that may affect reflectivity and mechanical stability.

These cluster formations further confirm that the coating lacks uniformity, possibly due to gas entrapment, contamination, or plasma-related non-uniformities during deposition.

4.2.3.6. Orb-like Feature Post Coating

Orb-like features, about 50–150 μm in diameter, appear in small numbers on both samples (Figure 4.38). Their distinct morphology suggests localized differences in nucleation conditions or surface chemistry during coating. Understanding and eliminating such anomalies would be essential to achieving a consistently uniform SiO_2 layer.

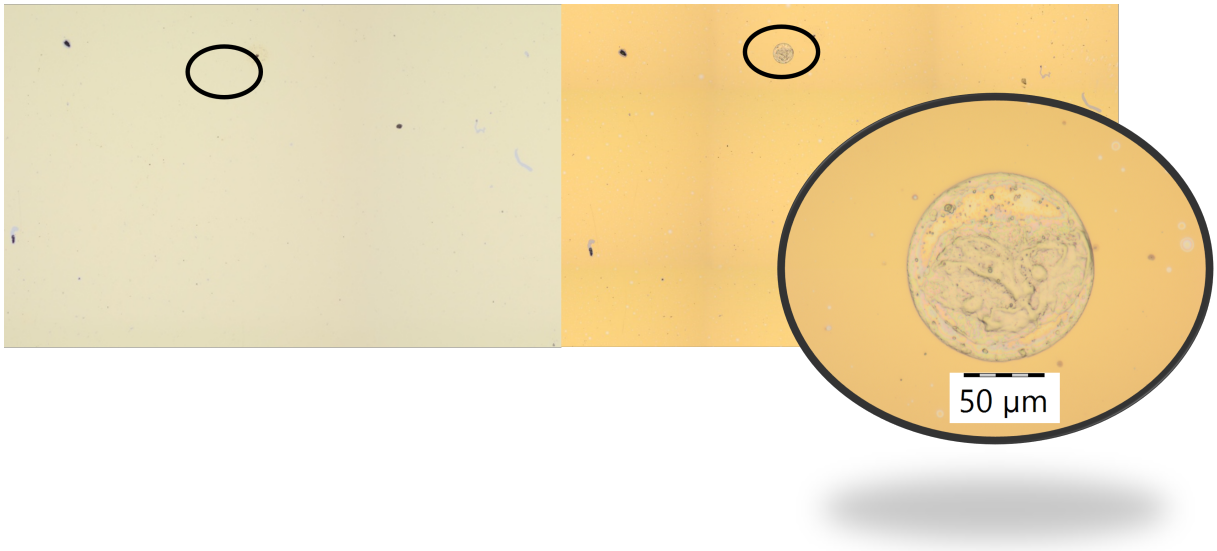

Figure 4.38.: Nomarski microscopy image of sample 807-6 at 50x magnification showing an Orb-like feature after coating. Such structures highlight localized irregularities in the deposition process.

4.2.3.7. Cross-Section Analysis with SEM/EDX Microscopy

A cross-sectional SEM/EDX examination of sample 807-6 provides additional insight into layer structure and adhesion. Although the examined section is from a rough edge (unpolished) area, the image reveals distinct layers and element distributions.

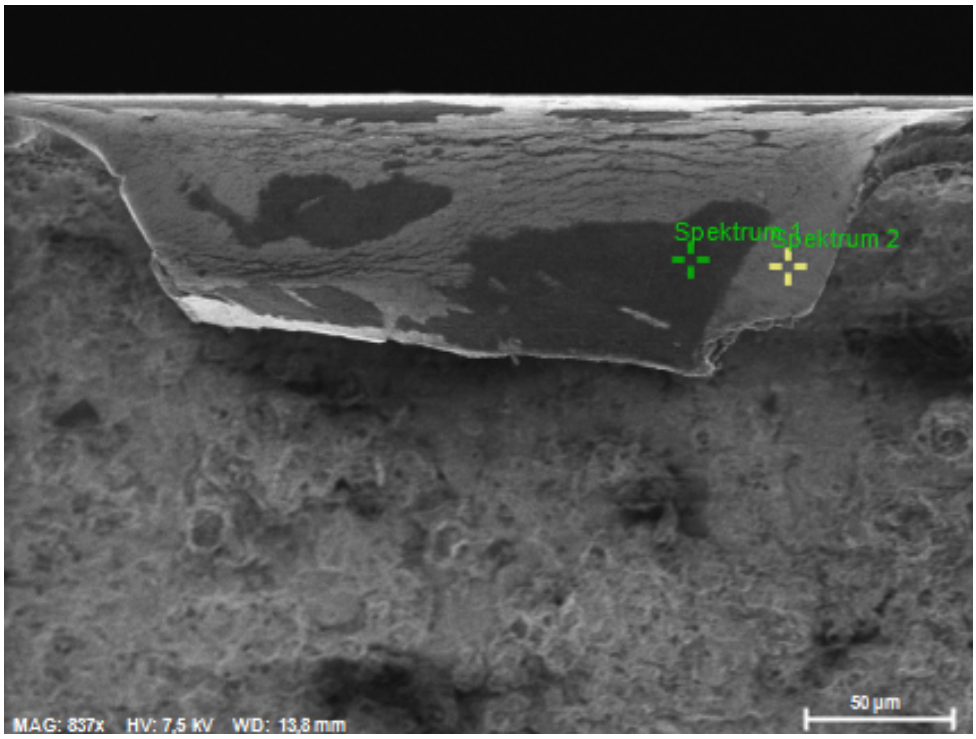

Figure 4.39.: Cross-sectional SEM image of sample 807-6 post-coating. The darker upper region is the SiO_2 coating, while the brighter lower region is the Gold-Nickel substrate. EDX confirms Si and O in the upper layer and Au, Ni in the substrate.

The SiO_2 layer appears darker due to lower average atomic number, while the underlying Au-Nickel substrate is brighter. EDX spectra confirm Si and O in the top layer, and Au, Ni in the substrate. However, uneven coating thickness and partial detachment in some spots highlight adhesion issues. Such imperfections could arise from thermal mismatches, contamination, or insufficient substrate preparation prior to deposition.

Since the exact density and thickness of the coating remain uncertain, choosing $E_0 = 7$–8 keV for EDX was a practical compromise. This energy range allowed the beam to penetrate the thin oxide and reach the underlying Au, confirming substrate presence. However, without systematic variation in E_0, accurately gauging layer thickness or isolating the coating's exact composition remains challenging. Future work should involve lower E_0 scans for surface-focused analysis or complementary analytical methods such as XPS or TEM/EELS for more precise layer characterization.

4.2.3.8. Summary of Nomarski and SEM/EDX Partial Results

Nomarski microscopy and SEM/EDX analyses corroborate the AFM findings: the SiO_2 coatings are non-uniform, with hemispherical protrusions, clusters, hole exposures, and orb-like anomalies. While certain regions achieve relative smoothness, the overall picture is one of spatial heterogeneity. The compositional analysis suggests no significant difference between domed and flat areas, pointing to morphological, rather than compositional, origins of these features.

The chosen E_0 values for EDX (7–8 keV) were constrained by practical limitations. This accelerating voltage, while sufficient to detect substrate elements, also reduces the compositional specificity of the near-surface layer. Systematic EDX scans at multiple energies, or alternate analytical methods, would refine understanding of the coating thickness and uniformity.

In conclusion, the Nomarski and SEM/EDX results reinforce the notion that the current PECVD conditions yield coatings with undesirable morphological features. Achieving a uniform, specular SiO_2 layer on these Gold-Nickel substrates will require further process optimization, improved substrate preparation, and possibly in-situ diagnostics to ensure stable and uniform layer growth.

4.2.4. Possible Origins of the Hemispherical Surface Features

The presence of hemispherical surface features represents one of the most striking outcomes of the PECVD SiO_2 coating process on the Gold-Nickel intake samples. These dome-like protrusions, revealed by AFM, Nomarski microscopy, and confirmed in SEM observations, are not observed in the pre-coated surfaces and are not characteristic of a uniformly deposited thin film.

While the exact formation mechanism remains unclear, several plausible explanations emerge:

Volmer-Weber Growth Mechanism

One well-known growth mechanism in thin-film deposition is the Volmer-Weber (VW) mode, where three-dimensional islands form on the substrate surface rather than a layer-by-layer film. In the VW growth mode, the film does not immediately spread uniformly; instead, isolated islands (or nuclei) form and grow as deposition continues. Eventually, these islands may coalesce, leading to non-uniform coverage and the formation of protrusions or dome-like structures.

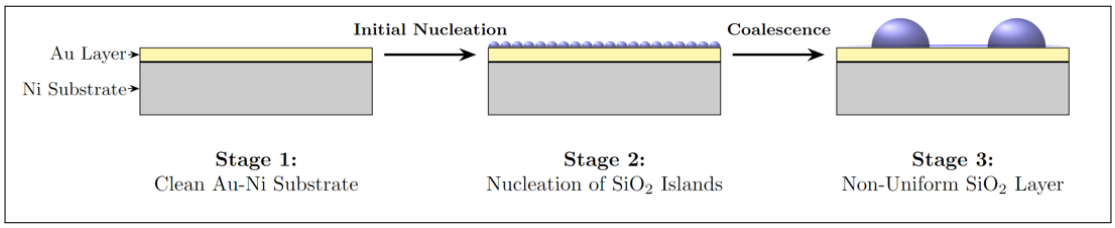

Figure 4.40.: Schematic representation of a Volmer-Weber growth scenario: (Stage 1) a clean Au-Ni substrate, (Stage 2) initial nucleation of SiO_2 islands, and (Stage 3) coalescence into non-uniform structures.

As illustrated in Figure 4.40, the initial SiO_2 deposition may not form a continuous film. Instead, discrete islands nucleate. Over time, these islands can grow and coalesce, potentially leaving behind dome-like features if the local conditions favor isolated, three-dimensional growth rather than uniform spreading.

Gas Entrapment and Bubble Formation

Another plausible origin is the entrapment of gas at the interface between the newly deposited SiO_2 and the underlying gold layer. During PECVD, gaseous precursors dissociate in plasma, forming reactive species that condense on the substrate. If small pockets of gas become trapped beneath the growing film, these pockets might inflate like bubbles, forming the observed hemispherical features. Subsequent solidification of the layer around the gas pocket would stabilize these dome-like structures. The AFM evidence of mechanical fragility—where re-scanning the same area altered the shape of a hemisphere—supports this theory, suggesting a thin, possibly hollow dome rather than a solid protrusion.

Localized Non-Uniform Nucleation

If, at certain surface sites, precursor adsorption or local plasma conditions lead to faster nucleation and growth, tiny mounds may form. Over time, continued deposition could produce dome-shaped protrusions. Variations in local surface energy, contamination, or microscopic surface defects could all favor nucleation at specific points, resulting in these structures. This scenario is closely related to the Volmer-Weber mechanism, where early-stage islands fail to coalesce into a smooth film.

Substrate Surface Chemistry Variations

Differences in substrate chemistry, such as residual hydrocarbons, microscopic particles, or patches of oxide, may influence how the SiO_2 layer grows. These chemical inhomogeneities could alter the precursor reactivity, causing abnormal growth patterns that manifest as domes or bubble-like features. Where the substrate is not perfectly uniform, local growth conditions may encourage three-dimensional island formation rather than a uniform film.

Plasma-Driven Instabilities

Non-uniform plasma density, local temperature fluctuations, or transient instabilities in the PECVD chamber could lead to uneven deposition rates. Such variations might cause localized stresses that deform the growing film, trapping and shaping pockets of material or gas into hemispheres. Combined with the VW growth mode, these plasma instabilities can intensify or sustain non-uniform island growth.

Thermal Expansion Mismatches

Differences in the coefficients of thermal expansion (CTE) between SiO_2, gold, and the underlying nickel substrate can generate stresses during film growth or subsequent cooling. Stressed regions might form out-of-plane protrusions. While this mechanism alone may not fully explain the dome shapes, it could contribute to their stabilization or growth once initially formed by other means.

In summary, the hemispherical surface features likely arise from a combination of factors. Volmer-Weber type island growth, gas entrapment, substrate chemistry variations, plasma-driven instabilities, and thermal effects all offer plausible contributions. Understanding and controlling these factors—through improved substrate preparation, refined PECVD parameters, and enhanced diagnostics—may enable more uniform SiO_2 coatings free from these dome-like anomalies.

4.2.5. PECVD Coating Overall Results

The collective findings from AFM, Nomarski microscopy, SEM/EDX analyses, and the inferred origins of the hemispherical features paint a complex picture of the PECVD SiO_2 coatings on Gold-Nickel substrates:

- **Substantial increase in roughness**:
  The pristine, low-roughness surfaces of the gold-nickel samples were transformed into topographies dominated by hemispherical protrusions, clusters, and orb-like features. Instead of achieving a uniform and specular oxide layer, the coating yielded a heterogeneous landscape with pronounced irregularities.
- **Morphological rather than compositional variations**:
  Despite the topographical diversity, preliminary EDX investigations suggest no major compositional differences between domed and flat regions—both appear to contain SiO_2 with underlying Au and Ni signals. This points toward processing conditions, surface contaminants, or localized gas entrapment as the principal culprits, rather than any phase separation or chemical inhomogeneity.
- **Fragility of the coating**:
  AFM scans showed that some dome-like features were mechanically sensitive. Repeated scans resulted in morphological changes, hinting at thin-walled structures that can be mechanically compromised. Such fragility is undesirable, as it indicates that the coating may not be robust enough to withstand mechanical stresses—whether from handling, launch vibrations, or operational conditions in a satellite environment.
- **Non-uniform deposition and potential contamination**:
  The appearance of "clean" elliptical regions without hemispherical features, holes that remained uncovered, and orb-like formations all underscore process-related instabilities. Subtle differences in substrate preparation, contamination, or local plasma conditions likely played a role. Achieving a truly uniform coating would necessitate stricter control over chamber environment, substrate cleaning procedures, and PECVD parameters.
- **Implications for ABEP applications**:
  The ultimate goal was to form a SiO_2 layer that could serve as a protective, specularly reflective coating for ABEP intakes in VLEO conditions. These results suggest that, under the current deposition conditions, such a film is not readily attainable. The hemispherical features, clusters, and defects would disrupt the aerodynamic properties and degrade optical specularity, potentially impairing particle collection efficiency and long-term durability.
- **Path forward for process optimization**:
  To realize the desired coating properties, further investigation and optimization are necessary. Strategies may include:
  - Using a cleanroom environment to minimize contamination.
  - Adjusting PECVD parameters (pressure, gas flow, power, temperature) to reduce instabilities and promote uniform nucleation.
  - Exploring different precursor chemistries or introducing post-deposition annealing steps to densify and smooth the oxide layer.

- Employing complementary characterization techniques (e.g., TEM cross-sections, XPS surface analysis, lower E_0 EDX measurements) to refine the understanding of film thickness, composition, and structure.

In conclusion, the PECVD SiO_2 coatings produced under the tested conditions fall short of achieving the specular, defect-free surface desired for ABEP intake applications. The presence of hemispherical features and other anomalies points to underlying issues in the deposition process and substrate preparation. Although not ideal in their current form, these findings provide valuable guidance on where and how process improvements should be targeted to eventually meet the stringent requirements of VLEO missions.

5. Conclusions

This thesis investigated the feasibility of forming protective SiO_2 layers on substrates relevant to ABEP intake systems operating in VLEO. The work encompassed two primary material, sintered SiC and gold-nickel substrates, each subjected to different oxidation or coating processes. By characterizing surface morphology, roughness, and elemental composition under simulated conditions or via plasma-enhanced techniques, this work has elucidated key factors governing oxide layer formation, surface quality, and potential specularity for ABEP applications.

For the SiC samples, the central question revolved around whether a passivating SiO_2 layer could be generated under high-enthalpy oxygen plasma exposure, and if this layer could provide a specularly reflective surface conducive to ABEP intake efficiency. The results indicate that, under controlled plasma conditions, SiC indeed forms a protective SiO_2 layer capable of mitigating atomic oxygen erosion. When starting from a highly polished, low-roughness SiC surface, the formation of a relatively smooth oxide film is more likely. Although perfect specularity was not fully realized in this first set of experiments, the oxide scales were significantly more uniform and less rough than those formed on coarser substrates. This demonstrates promising progress toward achieving a stable, durable, and potentially specular oxide that could serve as a functional ABEP intake surface in VLEO conditions. In essence, while further optimization of exposure parameters, temperature control, and sample finishing are necessary, the SiC samples have shown that it is possible to create a protective SiO_2 layer approaching the smoothness required for specular reflection. Such a development paves the way for realizing SiC-based ABEP intakes, potentially extending satellite lifetimes, improving aerodynamic efficiency, and reducing reliance on onboard propellant reserves.

For the gold-nickel intake samples, the work sought to evaluate the feasibility of achieving a uniform and optically smooth SiO_2 coating deposited via Plasma-Enhanced Chemical Vapor Deposition (PECVD) on the substrate. The results demonstrated that, although a SiO_2 layer was successfully deposited under the experimental conditions, its surface morphology was suboptimal. Specifically, the coating exhibited hemispherical dome-like features, clustered formations, and orb-like anomalies across the substrate, which significantly increased the surface roughness. This irregular morphology compromised the coating's specularity and raised critical concerns regarding its mechanical integrity and long-term durability. These findings indicate that the current PECVD process did not produce a SiO_2 layer with the smooth and specular quality necessary for effective use in Atmosphere-Breathing Electric Propulsion (ABEP) intake systems. To address these challenges and achieve a functional SiO_2 layer capable of supporting specular reflection under the harsh conditions of Very Low Earth Orbit (VLEO), several refinements in the coating process are required. First, improving substrate cleaning and preparation is essential to eliminate contaminants and establish uniform nucleation sites, which are critical for consistent coating formation. Second, more precise control over PECVD parameters, including gas flow rates, plasma power, and chamber pressure, is necessary to minimize plasma instabilities and reduce defect formation. Third, the introduction of interlayers could be explored to enhance adhesion and alleviate stress mismatches between the substrate and the coating, potentially mitigating crack propagation and delamination. Finally, conducting experiments in cleaner and more controlled environments would help prevent inadvertent particle deposition or gas entrapment, which are common sources of surface irregularities. By implementing these refinements, it is anticipated that the SiO_2 coatings could be transformed into smooth and uniform layers, meeting the stringent requirements for ABEP intake applications and enhancing their performance in VLEO conditions.

The insights gained from both sets of samples suggest multiple strategies for further development:

For the SiC Passivation Approach:

- **Enhanced substrate and surface preparation**: Additional polishing steps and contamination control could lead to even lower initial roughness and improve oxide uniformity.
- **Optimization of plasma processes**: Fine-tuning plasma parameters (exposure time, pressure, mass flow rates) could yield more stable and uniform oxide growth.
- **Advanced characterization and diagnostics**: Techniques such as TEM, XPS, or lower E_0 EDX measurements could better resolve oxide thickness and composition.

- **Material selection and refinement**: Investigating alternative SiC grades or doping strategies might lead to better oxidation kinetics and smoother oxide films.
- **Extended theoretical and computational analysis**: Modeling gas-surface interactions and oxide growth could inform experimental parameter choices and predict long-term stability under VLEO conditions.

For the PECVD Coating Approach:

- **Refine plasma parameters and PECVD conditions**: Systematic variation of deposition parameters may help mitigate dome formation and improve coating uniformity.
- **Investigation of interlayer and adhesion strategies**: Employing underlayers or graded interfaces might reduce stress and prevent bubble formation.
- **Transport and handling improvements**: More careful sample handling, storage, and transportation procedures could minimize contamination and mechanical damage.
- **Specularity and gas-surface interaction studies**: Complementary wind tunnel or plasma facility experiments to measure how altered roughness affects particle reflection and ABEP efficiency.

In conclusion, this work highlights the importance of material selection, surface preparation, and process optimization for advancing ABEP VLEO missions. The SiC-based approach demonstrated clear potential for achieving stable and reflective oxide coatings, while the PECVD system provided insights into the challenges that remain. By addressing these challenges and improving each step of substrate preparation, coating application, and testing, future work can pave the way for durable and efficient intake materials. Achieving a smooth and protective SiO_2 layer will not only enhance the performance and lifespan of ABEP systems but also support the long-term viability of satellite operations in Very Low Earth Orbit.

Bibliography

[1] Roberts, P. C. Crisp, N. H. Edmondson, S. Haigh, S. J. Lyons, R. E. Oiko, V. T. Rojas, A. M. Smith, K. L. Becedas, J. González, G.: "DISCOVERER: Radical Redesign of Earth Observation Satellites for Sustained Operation at Significantly Lower Altitudes". In: *68th International Astronautical Congress*. Adelaide, Australia: International Astronautical Federation, Sept. 2017, pp. 1–9.

[2] Roberts, P. Crisp, N. Abrao Oiko, V. Edmondson, S. Haigh, S. Huyton, C. Livadiotti, S. Lyons, R. Smith, K. Sinpetru, L. Straker, A. Worrall, S. Romano, F. Herdrich, G. Boxberger, A. Chan, Y.-A. Traub, C. Fasoulas, S. Smith, K. Outlaw, R. Becedas, J. Domínguez, R. González, D. Hanessian, V. Mølgaard, A. Nielsen, J. Bisgaard, M. Garcia-Almiñana, D. Rodriguez-Donaire, S. Sureda, M. Kataria, D. Villain, R. Perez, J. S. Conte, A. Belkouchi, B. Schwalber, A. Heißerer, B.: "DISCOVERER – Making commercial satellite operations in very low earth orbit a reality". In: *70th International Astronautical Congress*. IAC-19.C2.6.1x50774. Washington D.C., USA, 2019.

[3] Roberts, P. C. Crisp, N. H. Edmondson, S. Haigh, S. J. Holmes, B. E. Livadiotti, S. Macario-Rojas, A. Oiko, V. T. Smith, K. L. Sinpetru, L. A. Becedas, J. Domínguez, R. M. Sulliotti-Linner, V. Christensen, S. Jensen, T. K. Nielsen, J. Bisgaard, M. Chan, Y.-A. Herdrich, G. H. Romano, F. Fasoulas, S. Traub, C. Garcia-Almiñana, D. Garcia-Berenguer, M. Rodriguez-Donaire, S. Sureda, M. Kataria, D. Belkouchi, B. Conte, A. Seminari, S. Villain, R. Schwalber, A.: "DISCOVERER: Developing Technologies to Enable Commercial Satellite Operations in Very Low Earth Orbit". In: *71st International Astronautical Congress (IAC) – The CyberSpace Edition*. IAC-20,C2,6,12,x59301. 12-14 October, CyberSpace Edition, 2020.

[4] Crisp, N. Roberts, P. Romano, F. Smith, K. Oiko, V. Sulliotti-Linner, V. Hanessian, V. Herdrich, G. García-Almiñana, D. Kataria, D. Seminari, S.: "System Modelling of Very Low Earth Orbit Satellites for Earth Observation". In: *Acta Astronautica* (2021).

[5] Roberts, P. C. Crisp, N. H. Oiko, V. T. Edmondson, S. Romano, F. Rodriguez-Donaire, S. Garcia-Almiñana, D. Haigh, S. J. Holmes, B. E. Livadiotti, S. Macario-Rojas, A. Smith, K. L. Sinpetru, L. A. Becedas, J. Sulliotti-Linner, V. Christensen, S. Jensen, T. K. Nielsen, J. Bisgaard, M. Chan, Y.-A. Herdrich, G. H. Fasoulas, S. Traub, C. Sureda, M. Kataria, D. Belkouchi, B. Conte, A. Seminari, S. Villain, R. Schwalber, A.: "Early Results from the DISCOVERER Project". In: *72nd International Astronautical Congress (IAC)*. IAC-21-C2,6,8,x66171. Dubai, United Arab Emirates, 25-29 October, 2021.

[6] Romano, F. Herdrich, G. Chan, Y.-A. Crisp, N. Roberts, P. Holmes, B. Edmondson, S. Haigh, S. Macario-Rojas, A. Oiko, V. Sinpetru, L. Smith, K. Becedas, J. Sulliotti-Linner, V. Bisgaard, M. Christensen, S. Hanessian, V. Jensen, T. K. Nielsen, J. Fasoulas, S. Traub, C. García-Almiñana, D. Rodríguez-Donaire, S. Sureda, M. Kataria, D. Belkouchi, B. Conte, A. Seminari, S. Villain, R.: "Design of an intake and a thruster for an atmosphere-breathing electric propulsion system". In: *CEAS Space Journal* (2022). DOI: 10.1007/s12567-022-00452-1.

[7] Rapisarda, C.: "Modelling and simulation of atmosphere-breathing electric propulsion intakes via direct simulation Monte Carlo". In: *CEAS Space Journal* (2021). DOI: 10.1007/s12567-021-00414-z.

[8] Romano, F. Espinosa-Orozco, J. Pfeiffer, M. Herdrich, G. Crisp, N. Roberts, P. Holmes, B. Edmondson, S. Haigh, S. Livadiotti, S. Macario-Rojas, A. Oiko, V. Sinpetru, L. Smith, K. Becedas, J. Sulliotti-Linner, V. Bisgaard, M. Christensen, S. Hanessian, V. Jensen, T. K. Nielsen, J. Chan, Y.-A. Fasoulas, S. Traub, C. García-Almiñana, D. Rodríguez-Donaire, S. Sureda, M. Kataria, D. Belkouchi, B. Conte, A. Seminari, S. Villain, R.: "Intake design for an Atmosphere-Breathing Electric Propulsion System (ABEP)". In: *Acta Astronautica* 187 (2021). DOI: 10.1016/j.actaastro.2021.06.033.

[9] Herdrich, G. Fertig, M. Löhle, S. Pidan, S. Auweter-Kurtz, M. Laux, T.: "Oxidation behavior of silicon carbide-based materials by using new probe techniques". In: *Journal of Spacecraft and Rockets* 42.5 (2005).

[10] Murray, V. J. Pilinski, M. D. Jr., E. J. S. Qian, M. Minton, T. K. Madzunkov, S. M. Darrach, M. R.: "Gas-Surface Scattering Dynamics Applied to Concentration of Gases for Mass Spectrometry in Tenuous Atmospheres". In: *Journal of Physical Chemistry C* 121 (2017). DOI: 10.1021/acs.jpcc.7b00456.

[11] Herdrich, G. Auweter-Kurtz, M. Fertig, M. Löhle, S.: "Catalytic and oxidative behaviour of silicon carbide based materials for thermal protection materials". In: *Proceedings of the 9th European Space Thermal Analysis Workshop*. European Space Agency (ESA). 2004.

[12] Kaiser, C. Burghaus, H. Pagan, A. S. Herdrich, G.: "In-situ spectral emissivity assessment of sintered silicon carbide (SSiC) in high-enthalpy flows for catalysis investigations". In: *Proceedings of the FAR Conference*. 2022.

[13] Kaiser, C. F. Burghaus, H. Herdrich, G.: "Infrared Multiwavelength Pyrometry of SSiC and Ti6Al4V Surfaces in High-Enthalpy Oxygen Flows". In: *Aviation* (2024).

[14] Media Lario S.r.l.: *Optical Systems*. https://www.medialario.com/products/optical-systems. Accessed: 2024-11-29.

[15] Kirchheim, D. Wilski, S. Jaritz, M. Mitschker, F. Oberberg, M. Trieschmann, J. Banko, L. Brochhagen, M. Schreckenberg, R. Hopmann, C.: "Improved homogeneity of plasma and coating properties using a lance matrix gas distribution in MW-PECVD". In: *Journal of Coatings Technology and Research* 16.2 (2019), pp. 573–583. DOI: 10.1007/s11998-018-0138-4.

[16] Commission, E.: *Horizon 2020 - Funding Programmes and Open Calls*. https://research-and-innovation.ec.europa.eu/funding/funding-opportunities/funding-programmes-and-open-calls/horizon-2020_en. Accessed: 2024-11-28.

[17] Herdrich, G. Papavramidis, K. Maier, P. Skalden, J. Hild, F. Beyer, J. Pfeiffer, M. Fugmann, M. Klinker, S. Fasoulas, S. Souhair, N. Ponti, F. Walther, M. Wiegand, A. Walpot, L. Duesmann, B. Borras, E. Roberts, P. Crisp, N.: "System Design Study of a VLEO Satellite Platform Using the IRS RF Helicon-Based Plasma Thruster". In: *Acta Astronautica* 215 (2024). Published by Elsevier Ltd., pp. 245–259. DOI: 10.1016/j.actaastro.2023.11.009. URL: https://doi.org/10.1016/j.actaastro.2023.11.009.

[18] Consortium, D.: *SOAR (Satellite for Orbital Aerodynamics Research)*. https://discoverer.space/soar-satellite-for-orbital-aerodynamics-research/. Accessed: 2024-11-28.

[19] Center, N. G. R.: *Materials International Space Station Experiment (MISSE)*. https://www1.grc.nasa.gov/space/iss-research/misse/. Accessed: 2024-11-28.

[20] Orozco, J. E.: "Intake Design and Optimization for an Atmosphere-Breathing Electric Propulsion System". IRS-20-S-066. MA thesis. Stockholm, Sweden and Stuttgart, Germany: KTH Royal Institute of Technology and University of Stuttgart, Nov. 2020. URL: https://www.irs.uni-stuttgart.de.

[21] Feng, K.: "Investigation of a Novel Atmosphere-Breathing Electric Propulsion Platform and Intake". MA thesis. Stockholm, Sweden: KTH Royal Institute of Technology, Dec. 2022. URL: https://www.irs.uni-stuttgart.de.

[22] Weismann, S.: "Design of a Parabolic Intake to Test an Atmosphere Breathing Electric Propulsion Thruster". IRS-23-S-008. MA thesis. Stuttgart, Germany: Institute of Space Systems, University of Stuttgart, Dec. 2023. URL: https://www.irs.uni-stuttgart.de.

[23] Picone, J. M. Hedin, A. E. Drob, D. P. Aikin, A. C.: "NRLMSISE-00 empirical model of the atmosphere: Statistical comparisons and scientific issues". In: *Journal of Geophysical Research: Space Physics* 107.A12 (2002), SIA 15-1–SIA 15-16. DOI: 10.1029/2002JA009430.

[24] Center, N. G. S. F.: *Community Coordinated Modeling Center (CCMC)*. https://science.gsfc.nasa.gov/heliophysics/projects/184. 2024.

[25] Romano, F. Massuti-Ballester, B. Binder, T. Herdrich, G. Fasoulas, S. Schönherr, T.: "System analysis and test-bed for an atmosphere-breathing electric propulsion system using an inductive plasma thruster". In: *Acta Astronautica* 147 (2018). DOI: 10.1016/j.actaastro.2018.03.031.

[26] Takahashi, K.: "Thirty percent conversion efficiency from radiofrequency power to thrust energy in a magnetic nozzle plasma thruster". In: *Scientific Reports* (2022). DOI: 10.1038/s41598-022-22789-7.

[27] Romano, F. Chan, Y.-A. Herdrich, G. Traub, C. Fasoulas, S. Roberts, P. Crisp, N. Holmes, B. Edmondson, S. Haigh, S. Livadiotti, S. Macario-Rojas, A. Oiko, V. Sinpetru, L. Smith, K. Becedas, J. Sulliotti-Linner, V. Bisgaard, M. Christensen, S. Hanessian, V. Kauffman Jensen, T. Nielsen, J. Garcia-Almiñana, D. Garcia-Berenguer, M. Rodriguez-Donaire, S. Sureda, M. Kataria, D. Belkouchi, B. Conte, A. Seminari, S.: "Design, Set-Up, and First Ignition of the RF Helicon-based Plasma Thruster". In: *SPACE PROPULSION 2020+1*. 2021.

[28] Romano, F. Chan, Y.-A. Herdrich, G. Traub, C. Fasoulas, S. Roberts, P. Smith, K. Edmondson, S. Haigh, S. Crisp, N. Oiko, V. Worrall, S. Livadiotti, S. Huyton, C. Sinpetru, L. Straker, A. Becedas, J. Domínguez, R. González, D. Cañas, V. Sulliotti-Linner, V. Hanessian, V. Mølgaard, A. Nielsen, J. Garcia-Almiñana, D. Rodriguez-Donaire, S. Sureda, M. Kataria, D. Outlaw, R. Villain, R. Perez, J. Conte, A. Belkouchi, B. Schwalber, A. Heißerer, B.: "RF Helicon-based Inductive Plasma Thruster (IPT) Design for an Atmosphere-Breathing Electric Propulsion system (ABEP)". In: *Acta Astronautica* 176 (2020), pp. 476–483. DOI: 10.1016/j.actaastro.2020.07.008.

[29] Maxwell, J. C.: "On Stresses in Rarefied Gases Arising from Inequalities of Temperature". In: *Philosophical Transactions of the Royal Society of London* 170 (1879). DOI: https://doi.org/10.1098/rspl.1878.0052.

[30] Prieto, D. M. Graziano, B. P. Roberts, P. C.: "Spacecraft Drag Modelling". In: *Progress in Aerospace Sciences* 64 (2014). DOI: 10.1016/j.paerosci.2013.10.002. URL: https://research.manchester.ac.uk/files/52641369/SCDragModPreprint.pdf.

[31] Kulych, V. Fesenko, I. Kovtiukh, M. Tkach, V. Kaidash, O. Kuzmenko, Y. Chasnyk, V. Ivzhenko, V.: "Microstructure and Thermal Conductivity of Reaction-Sintered SiC". In: *Journal of Superhard Materials* 45.2 (2023). Translated from Nadtverdi Materialy, Vol. 45, No. 2, pp. 94–96, pp. 158–160. DOI: 10.3103/S1063457623020065.

[32] Pidan, S. Auweter-Kurtz, M. Herdrich, G. Fertig, M.: "Recombination coefficients and spectral emissivity of silicon carbide-based thermal protection materials". In: *Journal of Thermophysics and Heat Transfer* 19.4 (2005).

[33] Ioffe Institute: *NSM Archive - Silicon Carbide (SiC) - Thermal Properties*. https://www.ioffe.ru/SVA/NSM/Semicond/SiC/thermal.html. Accessed: 2024-12-04.

[34] Harris, G. L., ed.: *Properties of Silicon Carbide*. Vol. 13. EMIS Datareviews Series. London: Institution of Engineering and Technology, 1995. ISBN: 978-0852968703.

[35] Precise Ceramic: *Boron Nitride Overview: Properties, Production, and Uses*. Accessed: 2024-12-04. 2024. URL: https://www.preciseceramic.com/blog/boron-nitride-overview-properties-production-and-uses.html.

[36] *Diamond-Like Carbon*. https://www.sciencedirect.com/topics/engineering/diamond-like-carbon.

[37] Balat, M. Flamant, G. Male, G. Pichelin, G.: "Active to passive transition in the oxidation of silicon carbide at high temperature and low pressure in molecular and atomic oxygen". In: *Journal of Materials Science* 27 (1992).

[38] Laux, T.: "Untersuchungen zur Hochtemperaturoxidation von Siliziumkarbid in Plasmaströmungen". PhD thesis. Universität Stuttgart, 2004.

[39] Wagner, C.: "Theoretical analysis of the diffusion processes determining the oxidation rate of alloys". In: *Journal of The Electrochemical Society* 99.10 (1952).

[40] Turkdogan, E. T. Grieveson, P. Darken, L. S.: "Enhancement of Diffusion-Limited Rates of Vaporization of Metals". In: *Metallurgical and Materials Transactions B* 1.8 (1963). DOI: 10.1007/BF02670848. URL: https://doi.org/10.1007/BF02670848.

[41] Hegemann, D.: "Plasma Polymer Deposition and Coatings on Polymers". In: *Comprehensive Materials Processing*. Ed. by Elsevier. Elsevier Ltd., 2014, pp. 201–225. DOI: 10.1016/B978-0-08-096532-1.00426-X.

[42] Herdrich, G. H.: "Aufbau, Qualifikation und Charakterisierung einer induktiv beheizten Plasmawindkanalanlage zur Simulation atmosphärischer Eintrittsmanöver". PhD thesis. Universität Stuttgart, 2004.

[43] Herdrich, G. Auweter-Kurtz, M. Kurtz, H. Laux, T. Winter, M.: "Operational Behavior of Inductively Heated Plasma Source IPG3 for Entry Simulations". In: *Journal of Thermophysics and Heat Transfer* 16.3 (2002).

[44] Herdrich, G. Auweter-Kurtz, M. Kurtz, H.: "New Inductively Heated Plasma Source for Reentry Simulations". In: *Journal of Thermophysics and Heat Transfer* 14.2 (2000), pp. 218–225. DOI: 10.2514/2.6507. URL: https://doi.org/10.2514/2.6507.

[45] Laux, T.: "High-temperature oxidation of SSiC in plasma flows". In: *Proceedings of the CEAS Conference 2007*. 2007.

[46] *Geometrical Product Specifications (GPS) - Surface Texture: Profile Method - Terms, Definitions, and Surface Texture Parameters*. Updated version of ISO 4287:1997. Geneva, Switzerland: International Organization for Standardization, 2021. URL: https://www.iso.org/standard/72226.html.

[47] QATM: *Metallographic Polishing*. Website. Accessed: 2024-11-09. URL: https://www.qatm.com/knowledge/metallographic-polishing/.

[48] Kemet International: *Diamond Suspension for Metallography*. Website. Accessed: 2024-11-09. URL: https://www.kemet.co.uk/products/metallography/diamond-suspension-for-metallography.

[49] Nomarski, G.: "Application à la métallographie des méthodes interférentielles à deux ondes polarisées". In: *Revue de Métallurgie* 52.2 (1955), pp. 121–134. DOI: 10.1051/metal/195552020121.

[50] Pluta, M.: "Nomarski's DIC microscopy: A review". In: *Proceedings of SPIE* 1846 (1994). DOI: 10.1117/12.174146.

[51] Davidson, M. W. Abramowitz, M.: "Optical Microscopy". In: *Microscopy Today* (2013).

[52] Groot, P. de: "Principles of interference microscopy for the measurement of surface topography". In: *Advances in Optics and Photonics* 7.1 (2015). DOI: 10.1364/AOP.7.000001.

[53] Damian, V. Bojan, M. Schiopu, P. Iordache, I. Ionita, B. Apostola, D.: "White light interferometry applications in nanometrology". In: *Proceedings of SPIE* (2022).

[54] O'Mahony, C. Hill, M. Brunet, M. Duane, R. Mathewson, A.: "Characterization of micromechanical structures using white-light interferometry". In: *Measurement Science and Technology* 14 (2003). DOI: 10.1088/0957-0233/14/10/310.

[55] Boneberg, J. Kruger, R. Leiderer, P. Herminghaus, S.: "Laser Micromachining of Coated $YBa_2Cu_3O_{6+x}$ Superconducting Thin Films". In: *ResearchGate* (1998). Accessed: 2024-11-03. URL: https://www.researchgate.net/publication/1944428_Laser_Micromachining_of_Coated_YBa2Cu3O6x_Superconducting_Thin_Films.

[56] Binnig, G. Quate, C. F. Gerber, C.: "Atomic Force Microscope". In: *Physical Review Letters* 56.9 (1986), pp. 930–933. DOI: 10.1103/PhysRevLett.56.930.

[57] Institute of Solid State Physics, G. U. o. T.: *Nanosurf Easyscan 2 AFM Operating Instructions*. https://lampz.tugraz.at/~hadley/semi/ch9/instruments/afm/Nanosurf_Easyscan_2_v3.8.pdf. 2017.

[58] AG, N.: *How Does AFM Work?* Accessed: 2024-10-20. 2024. URL: https://www.nanosurf.com/en/support/how-does-afm-work.

[59] N. Umeda, S. I. Uwai, H.: "Scanning attractive force microscope using photothermal vibration". In: *Journal of Vacuum Science & Technology B* 9.2 (1991), pp. 1318–1322. DOI: 10.1116/1.585187.

[60] Sader, J. E. Chon, J. W. M. Mulvaney, P.: "Calibration of Rectangular Atomic Force Microscope Cantilevers". In: *Review of Scientific Instruments* 70.10 (1999). DOI: 10.1063/1.1150021.

[61] Newbury, D. E. Ritchie, N. W. M.: "Is Scanning Electron Microscopy/Energy Dispersive X-ray Spectrometry (SEM/EDS) Quantitative?" In: *Scanning* 35 (2013), pp. 141–168. DOI: 10.1002/sca.21041. URL: https://onlinelibrary.wiley.com/doi/10.1002/sca.21041.

[62] Goldstein, J. I. Newbury, D. E. Michael, J. R. Ritchie, N. W. M. Scott, J. H. J. Joy, D. C.: *Scanning Electron Microscopy and X-Ray Microanalysis*. 4th. New York: Springer, 2018. ISBN: 978-1-4939-6676-9. DOI: 10.1007/978-1-4939-6676-9. URL: https://link.springer.com/book/10.1007/978-1-4939-6676-9.

[63] Yao, S. Li, H. Pang, S. Zhu, B. Zhang, X. Fatikow, S.: "A Review of Computer Micro-Vision-Based Precision Motion Measurement: Principles, Characteristics, and Applications". In: *IEEE Transactions on Instrumentation and Measurement* Accepted for future publication (2021). This work is licensed under a Creative Commons Attribution-NonCommercial-NoDerivatives 4.0 License. DOI: 10.1109/TIM.2021.3065436. URL: https://doi.org/10.1109/TIM.2021.3065436.

[64] *Kyocera Fineceramics Europe GmbH - StarCeram S Material Data Sheet*. https://www.kyocera-fineceramics.de/fileadmin/user_upload/Download/werkstoffdatenblaetter/siliziumcarbid/Kyocera_Fineceramics_Europe_StarCeram_R__S.pdf. 2023.

[65] *Medialario S.r.l. - High Precision Optics and Components Manufacturer*. https://www.medialario.com/.

[66] *ESA - GIADA - Grain Impact Analyzer and Dust Accumulator*. https://www.esa.int/Science_Exploration/Space_Science/Rosetta/GIADA.

[67] Institut für Kunststoffverarbeitung (IKV): *Institut für Kunststoffverarbeitung (IKV) at RWTH Aachen University*. https://www.ikv-aachen.de/. Accessed: 2024-12-03. 2024.

[68] Rubner, J. Stellmann, L. Mertens, A.-K. Tepper, M. Roth, H. Kleines, L. Dahlmann, R. Wessling, M.: "Organosilica coating layer prevents aging of a polymer with intrinsic microporosity". In: *Plasma Processes and Polymers* 19.5 (2022), e2200016. DOI: 10.1002/ppap.202200016.

[69] *Cleanrooms and Associated Controlled Environments—Part 5: Operations*. ISO 14644-5:2004. Available from: https://www.iso.org/standard/33658.html. International Organization for Standardization. Geneva, Switzerland, 2004.

[70] *Carl Zeiss Microscopy GmbH - Instruction Manual: ZEISS EVO Scanning Electron Microscope*. Accessed: 2024-11-20. Jena, Germany, Nov. 2021. URL: https://www.zeiss.com/microscopy.

[71] *OKS Spezialschmierstoffe GmbH - Safety Data Sheet: OKS 2731*. Version 1.8. According to REACH Regulation (EC) No 1907/2006, amended by UK REACH Regulations SI 2019/758 - GB. Ganghoferstr. 47, D-82216 Maisach-Gernlinden, Germany, July 2022. URL: https://www.oks-germany.com.

[72] *Thorlabs GmbH - Ultra Pure Duster CA6-EU Label*. Compressed air spray label for CA6-EU. Information about usage, safety, and contents in multiple languages. Muenchner Weg 1, D-85232 Bergkirchen, Germany, n.d. URL: https://www.thorlabs.de.

[73] Veeco Wyko NT9100 Optical Profilometer - AggieFab, T. A. U. https://aggiefab.tamu.edu/equipment/veeco-wyko-nt9100/. 2022.

[74] Veeco Wyko NT9100 Operation Specifications - AggieFab, T. A. U. https://aggiefab.tamu.edu/equipment/veeco-wyko-nt9100/. 2022.

A. Appendix

A.1. Gold-Nickel Intake Samples Fabrication Process

The step-by-step fabrication process of Medialario S.r.l.[65] samples is detailed in Table A.1, outlining the procedures involved in producing high-quality gold-nickel mirrors suitable for optical applications.

Table A.1.: Step-by-step fabrication process of Medialario S.r.l.[65] samples

Step	Description
Mandrel preparation	The mandrel, typically made of aluminum, is manufactured and polished to achieve a surface roughness of approximately 0.2 to 0.3 nm, ensuring high-quality mirror replication.
Mandrel coating	A release agent is applied to the polished mandrel to facilitate the clean separation of the electroformed layer in subsequent steps.
Gold coating application	A uniform and adherent thin layer of gold is deposited onto the mandrel, forming the reflective surface of the mirror.
Nickel/Nickel-Cobalt alloy formation	The gold-coated mandrel is immersed in an electroforming bath where nickel or a nickel-cobalt alloy is electroformed to the required thickness, guided by finite element analysis (FEA) to balance structural integrity and weight.
Thickness optimization	FEA is utilized to optimize the electroformed layer's thickness, ensuring sufficient rigidity while minimizing material usage.
Cooling and separation	The mandrel is removed from the electroforming bath and cooled. Differential contraction between the aluminum mandrel and the nickel shell facilitates the clean separation of the mirror from the mandrel.
Mirror removal	The cooled nickel shell, retaining the gold layer, is separated from the mandrel without damaging the gold coating. The mandrel can be reused multiple times due to the effective release process.
Quality replication	The electroformed nickel shell replicates the mandrel's surface quality, maintaining the target roughness and precision necessary for optical applications.
Final product	The final mirror exhibits a shiny, gold-colored surface with a top gold layer and a nickel-based structural layer, suitable for use in high-precision optical systems.

A.2. Detailed Comparison of WLIM and AFM Specifications

A detailed comparative analysis of the specifications of the Veeco Wyko NT9100 White Light Interferometry Microscope (WLIM) system and the Nanosurf Easyscan 2 AFM system is presented in Table A.2. This comparison highlights the complementary nature of the two technologies, emphasizing their respective strengths and limitations across key metrics.

Table A.2.: Specifications of WLIM (Veeco Wyko NT9100)[73, 74] and AFM (Nanosurf Easyscan 2)[57]

Metric	**Veeco Wyko NT9100**	**Nanosurf Easyscan 2**
Vertical Resolution	$< 0.1\,\text{nm}$ (sub-nanometer)	$\sim 1\,\text{nm}$ (dependent on tip and conditions)
Lateral Resolution	$0.1\,\mu\text{m}$ to $13.2\,\mu\text{m}$ (varies with magnification)	5–10 nm (depends on AFM tip radius)
Measurement Speed	Fast (seconds to minutes, depending on area)	Slow (minutes to hours, varies by scan size and resolution)
Measurement Range	Up to several mm (with stitching)	Limited to $\sim 100\,\mu\text{m}$, extendable with specialized setups
Sample Interaction	Non-contact (optical-based)	Contact (static), tapping (dynamic), or non-contact modes
Surface Roughness (R_a)	Accurate for $R_\text{a} > 1\,\text{nm}$	Accurate for $R_\text{a} > 0.1\,\text{nm}$
Instrument Hardware	Veeco Wyko NT9100 with dual LED illumination	Nanosurf Easyscan 2 AFM with TableStable TS-150 vibration table
Software	Vision for Profilers Version 4.20	Nanosurf Easyscan 2 Version 3.8

A.3. Detailed AFM Scanning Configurations and Parameters

The scanning parameters for the AFM analysis were carefully optimized to balance image resolution, scan speed, and data quality. Tables A.3 and A.4 summarize the detailed scan parameters and system configurations used for both pre- and post-coating analyses.

Table A.3.: AFM system and measurement configuration

Parameter	Details
Cantilever Type	NCLR silicon cantilever
Resonance Frequency	Approximately 175 kHz
Operating Mode	Dynamic Force Mode (pre- and post-coating scans)
Measurement Environment	Air
Feedback Algorithm	Adaptive PID control
Software Versions	
Pre-Coating Analysis	Nanosurf Easyscan 2, version 3.8.8.13
Post-Coating Analysis	Nanosurf Easyscan 2, version 3.10.0.36
Scan Heads	
Pre-Coating	`Uncal_EZ2-AFM_110u.hed` (Static Mode)
Post-Coating	`10-07-254.hed` (Dynamic Mode)

Table A.4.: AFM scanning parameters

Parameter	Details
Scan Area	$5\,\mu$m $\times$ $5\,\mu$m to $110\,\mu$m $\times$ $110\,\mu$m
Image Resolution	512 points per line, 512 lines
Time per Line	1 to 4 seconds
Setpoint	50% of the free oscillation amplitude
Vibration Amplitude	60–200 mV
Excitation Amplitude	10–500 mV
Feedback Parameters	
Proportional Gain (P-Gain)	2000 to 10,000
Integral Gain (I-Gain)	1000 to 5000
Line Mode	Standard

A.3.1. AFM Roughness Data for the Intake Au-Ni Samples

The AFM roughness data for the intake Au-Ni samples, both before and after coating, are presented in the following tables. These tables provide comprehensive measurements of surface roughness parameters, highlighting the changes induced by the coating process.

Table A.5.: AFM analysis of sample 368-12 before coating in static mode

Sample	Measurement Type	Position	Side (µm)	ID	Area (µm²)	S_a (pm)	S_q (nm)	R_z (nm)	δS_a (pm)	δS_q (nm)	δR_z (nm)	Notes
368-12	Pre-Coating (Static-mode)	A	27.25	001	748.3	341.37	0.510	22.8570	34.14	0.051	2.29	Clean area
		B	25.00	002	629.9	295.92	0.448	11.2720	29.59	0.045	1.13	Clean area
		C	75.00	003	5669.0	214.26	0.356	21.9180	21.43	0.036	2.19	Clean area
		D	25.00	004	629.9	85.46	0.175	7.2015	8.55	0.018	0.72	Clean area

Table A.7.: AFM analysis of aample 807-6 before coating in static mode

Sample	Measurement Type	Position	Side (µm)	ID	Area (µm²)	S_a (pm)	S_q (pm)	S_z (nm)	δS_a (pm)	δS_q (pm)	δS_y (nm)	Notes
807-6	Pre-Coating (Static-mode)	A	25.00	014	629.9	182.63	1545.8	191.17	18.26	154.58	19.12	clean area
		B	25.00	015	629.9	201.05	481.52	41.331	20.11	48.15	4.13	clean area
		C	25.00	016	629.9	99.63	189.12	6.2622	9.96	18.91	0.63	clean area
		D	50.00	017	1259.8	309.77	403.28	10.02	30.98	40.33	1.00	clean area

Table A.6.: AFM analysis of sample 368-12 after coating in dynamic mode

Sample	Measurement Type	Position	Side (µm)	ID	Area (µm²)	S_a (pm)	S_q (nm)	R_z (nm)	δS_a (pm)	δS_q (nm)	δR_z (nm)	Notes
		A	48.05	005	2327.0	1461.6	2.7759	63.1140	146.16	0.278	6.31	Clean area with bubbles
		B	110.00	006	12 190.0	2328.8	6.5905	445.2500	232.88	0.659	44.53	Clean area with bubbles
368-12	Post-Coating (Dynamic-mode)	C	26.21	007	692.4	1607.9	2.6490	98.5720	160.79	0.265	9.86	Rough area
		D	110.00	008	12 190.0	5961.9	15.1400	944.1900	596.19	1.514	94.42	Scratched area with bubbles
		E	110.00	009	12 190.0	2431.1	6.5809	280.6300	243.11	0.658	28.06	Scratched area with bubbles
		F	40.39	010	1644.0	2758.2	4.3211	283.5100	275.82	0.432	28.35	Possible cluster area
		G	6.324	011	40.6	1051.8	1.4255	36.3160	105.18	0.143	3.63	Bubble
		H	28.56	012	827.3	4191.1	8.7062	406.1900	419.11	0.871	40.62	Bubble damaged
		I	110.00	013	12 190.0	11 736.0	17.7910	415.3600	1173.60	1.779	41.54	Cluster area

Table A.8.: AFM analysis of sample 807-6 after coating in dynamic mode

Sample	Measurement Type	Position	Width (µm)	ID	Area (µm²)	S_a (pm)	S_q (pm)	S_z (nm)	δS_a (pm)	δS_q (pm)	δS_y (nm)	Notes
		A	27.730	018	775.20	170.98	1.7107	162.05	17.10	0.171	16.21	Clean area with bubbles and holes.
		B	24.220	019	591.10	428.09	2.1845	252.99	42.81	0.218	25.30	Clean area with holes.
		C	20.120	020	407.90	554.68	4.5016	623.00	55.47	0.450	62.30	Clean area.
		D	20.700	021	432.00	483.76	1.7139	188.56	48.38	0.172	18.86	Clean area with bubbles.
807-6	Post-Coating (Dynamic-mode)	E	7.683	022	59.49	1.2840	4.2594	344.85	0.13	0.43	34.49	Single bubble.
		F	110.000	023	12.19	3.8273	10.8870	302.81	0.38	1.09	30.28	Clean area with surface defects.
		G	110.000	024	12.19	3.9352	11.1430	308.93	0.39	1.11	30.89	Clean area with surface defects.
		H	25.000	025	0.6299	494.64	936.07	57.373	49.46	93.61	5.74	Clean area with bubbles.
		I	25.000	026	0.6299	1328.9	1867.4	102.23	132.89	186.74	10.22	Clean area with bubbles.
		J	5.000	027	0.0252	603.42	808.14	12.093	60.34	80.81	1.21	Clean area.

A.4. Statistical Methods Employed

This appendix outlines the statistical methods employed for analyzing and interpreting the experimental data obtained from the PWK3 test parameters and surface roughness analysis. These methods were utilized to ensure rigorous and consistent evaluation of the results, allowing for meaningful comparisons and robust conclusions.

A.4.1. Descriptive Statistics

Descriptive statistics were applied to summarize and interpret the data derived from various experimental measurements, including the PWK3 test parameters and the surface roughness analysis conducted via WLIM and AFM scans.

Mean The mean represents the central tendency of the measured parameters, calculated as the arithmetic average of all observed values. This measure was particularly critical for characterizing average test conditions in the PWK3 environment and for summarizing the roughness parameters of the samples.

Standard Deviation (SD) The SD quantifies the variability or dispersion of the data around the mean, indicating the consistency of the experimental conditions and the variability in surface roughness across the samples.

Standard Error (SE) The SE was used to estimate the precision of the mean values. It was calculated using the formula:

$$\mathrm{SE} = \frac{\mathrm{SD}}{\sqrt{n}}$$

where n represents the number of observations. This parameter provided insight into the reliability of the mean values as representative of the population.

95% Confidence Interval (CI) The CI was computed to provide a range within which the true mean of the measured parameters is expected to fall with 95% confidence. The CI offered statistical assurance of the reliability and reproducibility of the results.

A.4.2. Surface Roughness Analysis

In the surface roughness analysis performed using WLIM and AFM scans, additional statistical metrics were utilized to account for variability and uncertainty in the measurements.

Absolute and Relative Error The absolute error was calculated as the difference between the measured value and its true or reference value, while the relative error was computed as the ratio of the absolute error to the true value, expressed as a percentage. These metrics were critical for assessing the accuracy of the surface roughness measurements.

Mean and Error Propagation For the AFM roughness analysis, mean roughness values were reported alongside the absolute error values, providing a comprehensive representation of the central tendency and associated uncertainty. Error propagation methods were employed where necessary to combine uncertainties from multiple contributing factors.

A.5. PWK3 Test Parameters

Detailed plasma parameters for the PWK3 tests calculated from the `.dat` files on samples IRS-01, IRS-03, and IRS-05 are provided in this appendix. The calculations were performed using a Python script provided as a separate file attached to the thesis.

A.5.1. Sample IRS-01 (Test ID: 219)

Table A.9.: Plasma parameters for sample IRS-01 test

Parameter	Mean	Standard Deviation
Anode Current I_{Anode}, A	18.85	0.10
Anode Voltage U_{Anode}, V	5861.43	16.90
Electrical Power P_{el}, kW	110.48	0.60
Tank Pressure p_{Tank}, hPa	0.54	0.03
Oxygen Mass Flow Rate m_{O_2}, mg/s	3214.92	1.32

A.5.2. Sample IRS-03 (Test ID: 220)

Table A.10.: Plasma parameters for sample IRS-03 test

Parameter	Mean	Standard Deviation
Anode Current I_{Anode}, A	18.85	0.12
Anode Voltage U_{Anode}, V	5849.87	18.11
Electrical Power P_{el}, kW	110.28	0.76
Tank Pressure p_{Tank}, hPa	0.51	0.03
Oxygen Mass Flow Rate m_{O_2}, mg/s	3217.63	1.36

A.5.3. Sample IRS-05 (Test ID: 221)

Table A.11.: Plasma parameters for sample IRS-05 test

Parameter	Mean	Standard Deviation
Anode Current I_{Anode}, A	18.75	0.10
Anode Voltage U_{Anode}, V	5855.04	15.42
Electrical Power P_{el}, kW	109.76	0.64
Tank Pressure p_{Tank}, hPa	0.54	0.03
Oxygen Mass Flow Rate m_{O_2}, mg/s	3215.46	2.57

A.6. Drawings

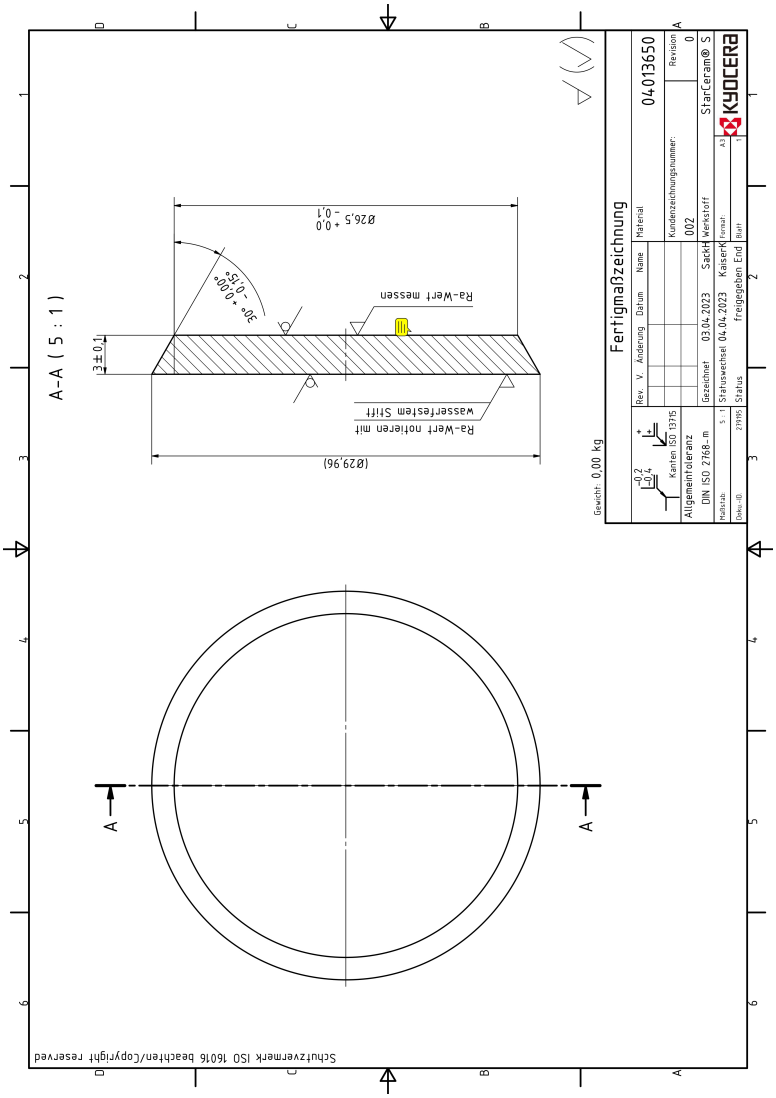

Figure A.1.: Drawing of the SiC samples from Kyocera Fineceramics procured for this work [64]

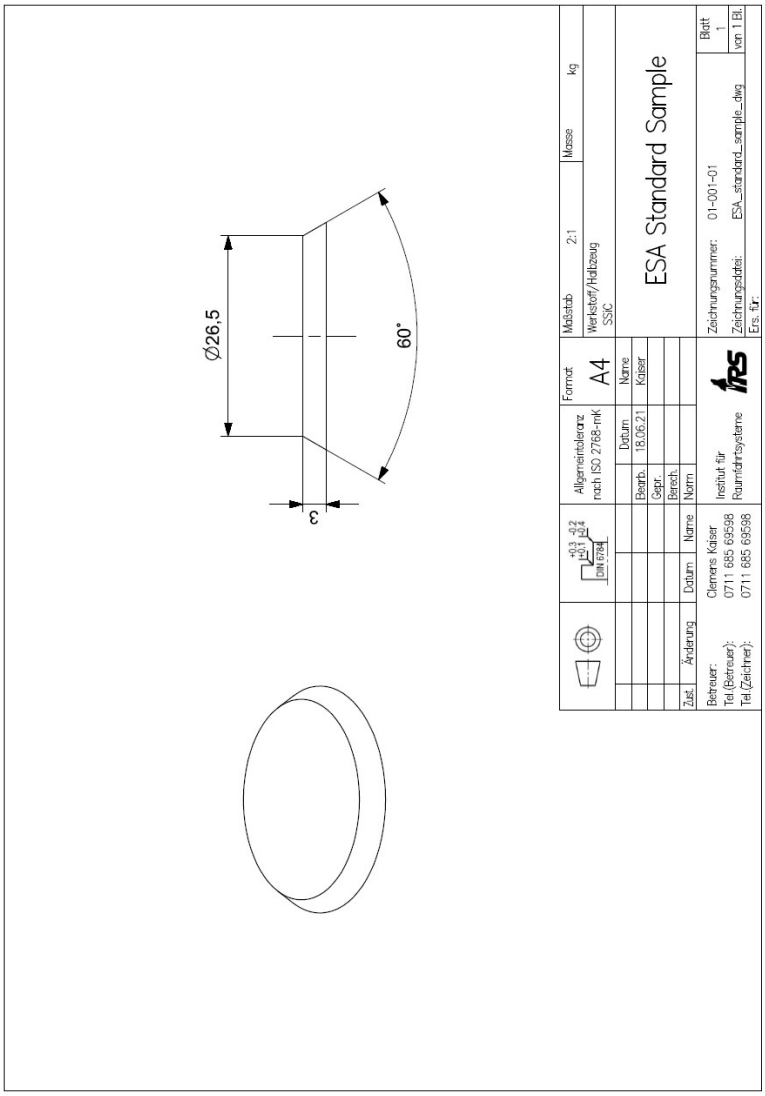

Figure A.2.: Drawing of the ESA standard SiC samples

A.7. Measurement Variability and Instrumental Considerations about WLIM

The roughness measurements obtained from WLIM are specific to the instrument used at DLR Stuttgart. Analyses conducted at the IMTCCC Institute using a different WLIM model on the same polished samples resulted in higher values of S_a, S_q, and S_z compared to those measured at DLR Stuttgart. This discrepancy highlights the sensitivity of WLIM results to the system configuration and measurement settings.

Table A.12.: Comparison of surface roughness parameters (S_a, S_q, R_z) for SiC samples IRS-01 to IRS-06 measured by IMTCCC and DLR Stuttgart

Sample	**IMTCCC Measurements**			**DLR Stuttgart Measurements**		
	S_a [nm]	S_q [nm]	R_z [µm]	S_a [nm]	S_q [nm]	R_z [µm]
IRS-01	40.7	151.1	10.0	16.87	25.26	320.58
IRS-02	41.8	141.2	5.9	15.63	22.97	357.52
IRS-03	46.2	144.5	6.2	16.05	24.58	334.20
IRS-04	70.1	313.5	10.2	16.17	23.15	327.20
IRS-05	44.0	171.9	7.1	15.29	23.19	432.63
IRS-06	44.5	179.2	8.1	16.19	23.96	358.27

The higher roughness values recorded by IMTCCC can be attributed to the limitations of the PSI mode used at DLR Stuttgart, which was not fully capable of capturing the depth of pores inherent to the porous structure of the SiC samples. To address this, additional measurements were attempted using WLIM in HDVSI mode at 100x magnification, targeting individual pores. However, reliable quantitative data could not be produced with HDVSI due to its restriction to very small areas (64 nm × 48 nm) compared to the PSI mode's larger measurement area (640 µm × 480 µm). Consequently, HDVSI mode was unsuitable for comprehensive surface analysis, and quantitative roughness assessments remained based on PSI mode measurements.

Furthermore, AFM analyses conducted on all samples before and after plasma exposure yielded S_a, S_q, and R_z values significantly lower (on the order of 3 to 8 nm) compared to WLIM measurements (approximately 20 nm in PSI mode). This discrepancy is likely due to AFM's limited precision in measuring surface profiles larger than 1 nm. While AFM excels at resolving atomic-scale features, it is less effective for characterizing larger-scale roughness and pore depths necessary for these SiC samples. For a detailed comparison between WLIM and AFM measurement techniques, refer to Appendix A.2.

A.8. Normogram for SEM/EDX Analysis

The normogram (Figure A.3) used for analyzing the SEM/EDX data provides a graphical representation that relates key parameters affecting the penetration depth of electrons during SEM/EDX scans. It allows the estimation of the interaction volume and effective penetration depth (R) of primary electrons in a material, which is essential for interpreting the detected elemental composition accurately.

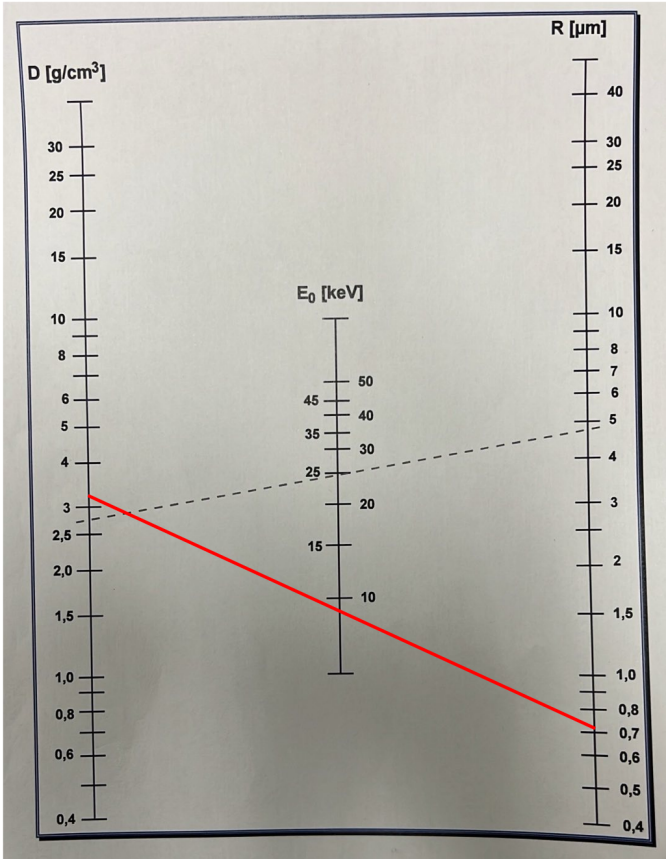

Figure A.3.: Application of the normogram to SiC (density = 3.17 g/cm^3) for determining penetration depths at E_0 = 7–8 keV and E_0 = 15 keV.

The normogram consists of three primary axes:

- **Density of the material (D)**: Represented on the left axis in units of g/cm^3, this parameter is specific to the sample material, such as silicon carbide (SiC), which has a density of approximately 3.17 g/cm^3 in this work [64].
- **Penetration depth (R)**: Represented on the right axis in micrometers (μm), this value indicates the depth to which primary electrons can effectively penetrate the material.
- **Electron beam energy (E_0)**: Represented on the central vertical axis in keV, this parameter specifies the accelerating voltage of the electron beam in SEM/EDX analysis.

The normogram utilizes curves linking D, R, and E_0, allowing the user to trace a value from one axis to another. For a given density, the normogram facilitates estimating R as a function of E_0.

The SEM/EDX scans conducted for this work faced significant challenges, particularly related to noise in the data. The scans at E_0 = 7–8 keV were notably noisy, making it difficult to obtain clean and reliable elemental maps. This noise may have stemmed from several factors, including surface roughness, charging effects, or limitations in the sensitivity of the detector at lower beam energies. Moreover, the noisy nature of the scans complicated the normalization process used to estimate the percentages of SiO_x and SiC. While the normogram provided a theoretical estimate of penetration depth, these noisy results underscore the necessity of further analyses at higher signal-to-noise ratios and at additional E_0 values to validate the trends observed.

A.9. Algorithms and Tools Used for Data Processing

A.9.1. Python Scripts for Surface Roughness Data Analysis

A custom Python script was developed to process the `.asc` files generated from White Light Interferometry Microscopy (WLIM) measurements conducted at DLR Stuttgart. The script was designed to streamline the data analysis workflow and ensure precise calculation and visualization of surface roughness parameters.

Data Import and Preprocessing The script reads and preprocesses raw `.asc` files, ensuring compatibility with analysis tools. Invalid or missing data points are handled appropriately to maintain data integrity.

Calculation of Roughness Parameters The arithmetic mean roughness (S_a), root mean square roughness (S_q), and maximum height of the surface (S_z) are calculated. Descriptive statistics such as mean and standard deviation are provided for these parameters to summarize the data effectively.

3D Surface Visualization Using the Plotly library, the script generates interactive 3D visualizations of the surface topography, enabling a detailed examination of surface morphology before and after plasma exposure.

Modular and Extensible Design The script employs a modular approach, allowing users to easily adapt or extend its functionality for future analyses or integration with other datasets.

The Python environment setup, including required package installations (`numpy`, `pandas`, `plotly`, etc.), and detailed comments explaining each function, are included within the script. This ensures reproducibility and facilitates use by other researchers.

The complete script is provided as an attachment to this document.

A.9.2. Python Scripts for Plasma Wind Tunnel Data Analysis

A Python script was developed to process, analyze, and visualize the experimental data obtained from the PWK3 tests. The script automates various tasks, including parsing data files, filtering time ranges, computing corrected temperatures based on emissivity and transmissivity, plotting temperature variations, and conducting statistical analyses. This ensures efficiency, consistency, and accuracy in data handling and presentation.

Data Parsing and Preparation The script reads and parses custom `.dat` files from PWK3 experiments, converting the data into a structured format (Pandas DataFrame) for easy manipulation.

Temperature Correction The measured temperature (T_m) is corrected to account for emissivity (ε) and window transmissivity (τ) using the formula:

$$T_w = \frac{1}{\frac{1}{T_m} + \frac{\lambda k}{hc} \ln(\tau \cdot \varepsilon)}$$

This correction improves the accuracy of the measured data.

Visualization The script generates plots to visualize measured and corrected temperatures over time, as well as temperature variations after reaching specific thresholds.

Statistical Analysis Statistical metrics (mean, standard deviation, standard error, confidence intervals) are computed for key parameters such as temperature, pressure, and heat flux.

Steady-State Detection The script analyzes temperature trends to identify steady-state conditions before a decrease in temperature, crucial for interpreting plasma behavior.

This script is instrumental in ensuring the reproducibility and reliability of data processing for PWK3 experiments. The complete Python script is provided as an external attached file to this thesis for further reference and use.

A.9.2.1. Image Processing and Visualization Tools

Several software tools were utilized to process experimental images, generate visualizations, and ensure the clarity and quality of data representation. GIMP was employed extensively for image modifications, including contrast adjustments, noise reduction, and cropping, to enhance visual data clarity. Inkscape served as the primary tool for creating vector-based schematics and diagrams, enabling precise representation of the experimental setup and findings. Additionally, IrfanView64 was used for handling high-resolution microscopy images, ensuring image fidelity and compatibility with different software formats. Collectively, these tools played a vital role in visual data presentation and integration within this manuscript.

A.9.2.2. Computational Methods and Manuscript Preparation

Python was a cornerstone for computational tasks, including data analysis, scripting, and visualization. Libraries such as NumPy, Pandas, and Matplotlib were employed to perform statistical evaluations and generate plots. OpenAI o1-mini-2024-09-12 api, an advanced language model, facilitated script optimization and computational efficiency, streamlining data workflows. For manuscript preparation, Perplexity AI's advanced language model contributed to enhancing grammar, style, and clarity. Challenges such as image processing limitations and software compatibility were mitigated by standardizing file formats and optimizing resolution settings. All Python scripts developed for this work are provided as supplementary material, with detailed annotations to promote reproducibility. Despite these technological contributions, the author remains solely responsible for the manuscript's content, accuracy, and scientific integrity.